Revision 1

Petrology and geochemistry of lunar granite 12032,366-19 and implications for lunar granite petrogenesis

Stephen M. Seddio[1,*], Bradley L. Jolliff[1], Randy L. Korotev[1], and Ryan A. Zeigler[2]

[1]Department of Earth and Planetary Sciences and the McDonnell Center for Space Sciences, Washington University, St. Louis, MO 63130, U.S.A. [2]Astromaterials and Exploration Science Directorate, NASA – Johnson Space Center, mail code KT, 2101 NASA Pkwy, Houston, TX 77058, U.S.A.

ABSTRACT

Apollo 12 sample 12032,366-19 is a 21.3-mg granite fragment that is distinct from any other lunar granite or felsite. It is composed of barian K-feldspar, quartz, sodic plagioclase, hedenbergite, fayalite, and ilmenite, with trace amounts of zirconolite, baddeleyite, apatite, and merrillite. The texture of 12032,366-19 is largely a micrographic intergrowth predominantly of K-feldspar and quartz and, to a lesser extent, plagioclase and quartz. Hedenbergite, fayalite, and ilmenite are present in minor but significant quantities—6.0, 3.1, and 1.7 wt%, respectively—and are scattered throughout the feldspar-quartz intergrowths. Trace amounts of Zr-bearing phases are found including zirconolite (0.6 wt%) and baddeleyite (0.04 wt%). Incompatible trace-element concentrations are high in 12032,366-19, particularly the high-field-strength elements, e.g., Zr, Sm, and Th (1500, 25, and 61 µg/g, respectively). The chondrite-normalized,

---

[*] E-mail: sseddio@levee.wustl.edu

rare-earth-element concentrations form a "V-pattern" that is characteristic of other lunar granitic material. Modeling 12032,366-19 as a derivative from a KREEP-like parent melt, the composition and mineral assemblage can be obtained by extended fractional crystallization combined with separation of the low-density minerals plus trapped melt components prior to final solidification. However, this model cannot quantitatively account for the relatively sodic composition of the plagioclase (An_{34-50}) and requires that the starting melt has Na_2O of 1.2 – 1.4 wt%, which is higher than most KREEP compositions. Formation of this assemblage by silicate-liquid immiscibility is neither required nor indicated by petrogenetic modeling.

Keywords: granite, Moon, zirconolite, apatite, felsite, Apollo 12

INTRODUCTION

There are about twenty known lunar granites (Appendix 1) including "large" individual samples (e.g., Apollo 12 sample 12013, 82 g) and clasts within breccias (e.g., 14321,1027, 1.8 g). Most lunar granites are fine-grained; sample 15405,12 is the coarsest with >1-mm mineral grains (Ryder 1976). Lunar granites characteristically contain intergrowths of K-feldspar and silica. Plagioclase is also common and may be intergrown with silica as well. Lunar granites are diverse in the presence, abundance, and compositions of pyroxene and olivine (typically fayalite), and contain nominally anhydrous minerals with the exception of apatite. Most lunar granites have been severely affected by meteorite impacts in that they have been partially melted or brecciated, have experienced shock metamorphism, or contain clasts of other lithologies as well as Fe-Ni metal from meteorite impactors. We describe here a small granite fragment, designated 12032,366-19, separated from Apollo 12 regolith sample 12032. This granite rock fragment is petrographically, mineralogically, and compositionally distinct from any previously characterized lunar granite and is largely unaffected by processes associated with meteorite impacts, i.e., it is monomict and unbrecciated.

SAMPLES AND EXPERIMENTAL PROCEDURE

Sample 12032 is one of several regolith bulk soil samples collected on the Apollo 12 mission. Subsample 366 consists of forty-one 2–4 mm grain-size lithic fragments allocated for the studies of Barra et al. (2006) and Korotev et al. (2011) along with 317 lithic fragments from other Apollo 12 regolith samples. The subject of this paper is the 19th fragment in the subset, designated 12032,366-19 (Fig. 1). We examined all 358 fragments under a binocular microscope and analyzed each one individually for concentrations of 26 chemical elements by INAA (instrumental neutron activation analysis; Korotev et al. 2011). Eight fragments were found to be granitic in composition, with 12032,366-19 being the largest at 21.3 mg. INAA results for 12032,366-19 are reported in Table 1. Results for 12001,912-02 (9.2 mg) and 12032,366-07 (15.7 mg) are reported in Barra et al. (2006). Compositional results for the other five fragments (2.7–7.5 mg) are reported in Appendix 1. (INAA data for all 366 fragments are presented in the electronic annex of Korotev et al. 2011.)

After INAA, which is effectively nondestructive, we mounted and polished the sample in a petrographic thick section for EPMA (electron-probe microanalysis). The texture and mineral assemblage were characterized by high-resolution BSE (back-scattered electron) imaging and X-ray map analysis using the 5-wavelength-spectrometer

JEOL 8200 electron microprobe at Washington University, which includes a high-intensity LIFH/PETH H-type spectrometer and an EDS (energy-dispersive spectrometer) with an SDD (silicon-drift detector). Images and maps were generated at an accelerating voltage of 15 kV and a probe current of 25 nA (50 nA for X-ray maps), except as indicated below. We used a combination of WDS (wavelength-dispersive spectrometers) and the SDD EDS to generate X-ray maps.

Quantitative mineral compositions were determined by WDS EPMA using the Probe for EPMA software developed by Probe Software, Inc. In addition, we used the Probe for EPMA software for data correction including peak interference corrections (e.g., Th mβ on U mα; and Fe Lα_1 on F Kα). Nominal analytical conditions for typical mineral phases (feldspar, silica, pyroxene, fayalite, ilmenite, and glass) were 15 kV accelerating voltage and 25 nA probe current, with beam diameters ranging from 1 to 10 µm. Analytical standards included synthetic and natural silicate, oxide, and REE glass standards of Drake and Weill (1972) and Carpenter et al. (2002) for primary calibration, and these were checked against secondary standards.

Typically, elements were measured using the Kα lines and counted on peak for 40 seconds (Si, Ti, Al, Cr, Fe, Mn, Mg, Na), except for elements analyzed using the high-intensity spectrometer (Ca, K, and P were counted for 20 seconds, and Ba, using the Lα line, was counted for 120 seconds). In addition to these elements, analyses of Zr-rich minerals included an expanded element list as follows: V (Kα; 20 seconds); Zr (Lα; 60 seconds); La, Ce, Nd, and Yb (Lα; 120 seconds each); Hf, Ta, and Pb (Mα; 180 seconds each); Y and Nb (Lα; 220 seconds each); and U and Th (Mα; 240 seconds each). This protocol led to detection limits for most minor and trace elements in the 0.01 to 0.04 wt% range (100 to 400 μg/g).

When analyzing phosphates, elements measured using the Kα lines were counted on peak for 20 seconds (Ca), 25 seconds (Na), 30 seconds (Mn, Fe), 35 seconds (Al), 40 seconds (Mg, Si, and P), 45 seconds (Cl), and 130 seconds (F); elements measured using the Lα lines were counted on peak for 30 seconds (La, Ce, Gd, Nd, and Yb; all but Ce were analyzed using the H-type spectrometer) and 45 seconds (Y). We used the Probe for EPMA software to correct for the interference of Fe $L\alpha_1$ and Ce Mζ on F Kα and to apply a non-linear (polynomial) background correction for F (and Si). The F X-ray count-rates, which were analyzed on a layered-dispersive element (LDE1) crystal, were found to vary with positive linear time dependence (Fig. 2; Stormer et al. 1993). Such variations were accounted for by the time-dependent intensity correction of the Probe for EPMA software, which we used to project the F X-ray count-rates back to time zero using a linear extrapolation to determine the intensity (e.g., McCubbin et al. 2010). In our analyses of the REEs, we applied the following the interference corrections using the Probe for EPMA software: Nd Ll on La $L\alpha_1$; La $L\gamma_3$, Ce $L\gamma_1$, and Nd $L\beta_2$ on Gd $L\alpha_1$; and Ce $L\beta_1$ on Nd $L\alpha_1$.

We used a modal recombination technique that we designate CMR (constrained modal recombination; Tables 1 and 2) to estimate the bulk concentration of elements for which concentration data were not obtained by INAA. The model was constrained to fit the oxides for which both microprobe and INAA concentrations were obtained (FeO, CaO, BaO, Na_2O, K_2O, and ZrO_2). Phase abundances (Table 2) were determined using image analysis of a BSE mosaic and X-ray maps to essentially count all pixels in each phase, which were then divided by the total number of pixels (background subtracted) to obtain the area fraction which we assume is indicative of the volume fraction. The volume fraction of each phase was multiplied by the density scaled to the composition of each respective phase (Deer et al. 1976). Finally, we divided these individual values by their sum to yield weight fractions. The bulk concentrations of each oxide were then calculated by summing the oxide concentration of each phase (an average of the phase compositions determined by electron microprobe) multiplied by the weight fraction of the phase (see example for SiO_2 below).

$$[\mathrm{SiO_2}]_{\mathrm{Bulk}} = \sum_{\mathrm{phase\ n=1,2,3\ldots}} \left([\mathrm{SiO_2}]_{\mathrm{n}} \mathrm{X}(\mathrm{weight\ fraction\ of\ phase\ n})\right)$$

The bulk composition obtained from INAA represents the entire 21.3 mg sample, but the concentrations generated from the constrained modal recombination technique represent only the specific plane of the section exposed by the polished mount and the BSE image and X-ray maps of that section. To assure that our bulk major-element composition was representative of the whole sample, we adjusted phase proportions from those obtained from image analysis to best-fit the INAA data. For example, our polished section of 12032,366-19 contains 6.2% plagioclase and 7.3% hedenbergite (area percentages converted to weight percentages) leading to a bulk CaO concentration of 2.2 wt% for 12032,366-19 (based on the average compositions of plagioclase and hedenbergite). INAA, however, yields a bulk CaO of 2.9 ± 0.2 wt%. In CMR, we increase the plagioclase abundance to 19 wt%, and decrease the hedenbergite abundance to 6.0 wt% (to fit both the INAA derived bulk CaO of 2.9 ± 0.2 wt% and FeO of 4.99 ± 0.05 wt%). The CMR bulk CaO therefore is 3.04 wt%. This example is simplified since

CMR takes the CaO contribution of all present phases into account, not just plagioclase and hedenbergite.

The CMR error was calculated using the error from both EPMA and image analysis. We applied counting statistics to the total number of pixels attributed to each phase in the image and X-ray maps (Fig. 3,4). The final "% Error" values are the result of propagating error through averaging the phase compositions, multiplying the average compositions by the wt% of that phase, and summing those values for each oxide or element. The trace-element compositions listed in the "EPMA" composition are from zirconolite, baddeleyite, REE-rich apatite, RE-merrillite, and apatite. These phases account for very small portions of the image, and their abundances were constrained to fit the INAA data as closely as possible. Following the same procedures for error propagation as with the major elements, the errors in the model associated with the trace elements would be between 260 and 640%. The trace-element errors are high because the trace elements are concentrated in trace minerals (e.g., zirconolite) which are represented by a relatively small number of pixels in the image and X-ray maps resulting in high error from counting statistics.

One irregular zirconolite grain (see descriptions in next section) yielded initial compositional analyses with anomalously high SiO_2. We assume that the zirconolite grain thickness might be such that the analyzed composition resulted from overlap of the electron interaction volume with another mineral. To further investigate this composition, we obtained three BSE images of the area at 5, 15, and 25 kV accelerating voltages (Fig. 5). We then modeled electron trajectories with Monte Carlo simulations using the Casino program version 2.42 (Hovington et al. 1997). Simulations of 5000 electron trajectories each were run at 5, 15, and 25 kV on models consisting of K-feldspar overlying zirconolite and zirconolite overlying quartz. The thickness of the top layer was varied. We constrained the thickness of the overlying phases by noting whether or not the backscattered electrons interacted only with the top phase at the different accelerating voltages. A detailed description of our process of determining the zirconolite composition is in Appendix 2.

Following the method of Montel et al. (1996), we calculated the crystallization age of 12032,366-19 from our analyses of zirconolite. In doing so, we assumed that all Pb analyzed is radiogenic which appears valid since nonradiogenic Pb should not exist in zirconolite beyond trace concentrations because Pb does not fit in the crystal structure. Given that assumption,

$$\mathrm{Pb} = \frac{\mathrm{Th}}{232}\left(\mathrm{e}^{\lambda^{232}\mathrm{t}} - 1\right)208 + 0.9928\frac{\mathrm{U}}{238.04}\left(\mathrm{e}^{\lambda^{238}\mathrm{t}} - 1\right)206 + 0.0072\frac{\mathrm{U}}{238.04}\left(\mathrm{e}^{\lambda^{235}\mathrm{t}} - 1\right)207$$

where Pb, Th, and U are in ppm and λ^{232} (4.9475×10^{-11} yr^{-1}; Jaffey et al. 1971), λ^{235} (9.8485×10^{-10} yr^{-1}; LeRoux and Glendenin 1963), and λ^{238} (1.55125×10^{-10} yr^{-1}; LeRoux and Glendenin 1963) are the decay constants for Th^{232}, U^{235}, and U^{238}, respectively. Solving for *t* yields the age of the analyzed grain along with the fraction of lead generated from each parent element. We report the average crystallization age calculagted for each zirconolite analysis and report the error as the 95% confidence interval.

We identified the silica phase as the polymorph quartz by Raman spectroscopic analysis using a Hololab 5000-532 laser Raman spectrometer (Kaiser Optical Systems, Inc.). The 532 nm line of a frequency-doubled Nd:YAG solid-state laser was used as the excitation source. Analyses were done using a 20× long-working distance objective (NA=0.4), which condenses the laser beam into a spot of 6 μm diameter on the sample, with an average power of 11 mW. This objective also collects the back-scattered Raman photons from the sample. These photons were sent through a multimode optical fiber to a Raman spectrograph. A volume holographic grating spectrometer disperses the collected Raman photons into a Raman Stokes shift range of 100 to 4300 cm^{-1} relative to the 532-nm laser line, with a spectral resolution of 4–5 cm^{-1}. See Freeman et al. (2008) for more analytical details.

RESULTS

Petrography

Lunar sample 12032,366-19 is an unshocked, unbrecciated, fine-grained granite fragment. It is composed predominantly of granophyric intergrowths of barian K-feldspar ($An_{0.7-16}$,Ab_{21-50},Or_{33-78},$Cn_{0.4-3.9}$) and quartz (Figs. 3,4) that, according to modal analysis, account for ~62 wt% of the sample, and to a lesser extent, a graphic intergrowths of plagioclase (An_{34-50},Ab_{49-65},$Or_{0.8-6.6}$,$Cn_{0.0-0.3}$) and quartz (Table 2, Figs. 3,4) that account for ~27 wt% of the sample. K-feldspar and silica intergrowths extend throughout the entire sample, whereas intergrowths of plagioclase and silica occur on the scale of ~1 mm. The mafic phases are present in significant amounts (6.0 wt% hedenbergite and 3.1 wt% fayalite) compared to most other lunar granites (e.g., 12013 “Light;” 12033,507; 14161,7269; 14303,204; 14321,1027; 15405,12; and 73255,27,3; see Appendix 1 for references) in which it is common for either pyroxene or olivine (or both) to be absent. There are >20 hedenbergite grains and >30 fayalite grains exposed in our polished section of 12032,366-19.

Potassium feldspar. Compositions of K-feldspar (Fig. 6; Table 3) are similar, from spot to spot and as reflected in the potassium X-ray image, with two exceptions. (1) In several instances, large subhedral grains (as large as 440 × 100 μm) of K-feldspar lack quartz intergrowths (Figs. 3,4) and are zoned. The cores of these grains have a higher Na/K (e.g., An_{15},Ab_{50},Or_{33},$Cn_{1.9}$) than their rims, which have Na/K similar to the rest of the K-feldspar in the sample (e.g., $An_{1.6}$,Ab_{28},Or_{67},$Cn_{3.0}$;Fig. 4). (2) The K-feldspar ("Kfs*" of Table 3) that is part of a subrounded inclusion inside one of the three "large" (see below) pyroxene grains has among the lowest Na/K in the fragment (An_1,Ab_{21},Or_{78},$Cn_{0.5}$). Moreover, in the K-feldspar in the inclusion, the abundance of the Cn (celsian, Ba-feldspar) component is only 0.5%, whereas the other analyzed K-feldspar compositions have Cn values of 1.6 to 3.9% (0.91 to 1.90 wt% BaO). The "Kfs*" analyses also have the highest FeO content (0.44 to 0.49 wt%) of the analyzed K-feldspar grains but not by a large amount (the other analyses range from <0.05 to 0.34 wt%).

Plagioclase. Plagioclase is not zoned and is unusually sodic for a lunar rock ($An_{33.5-50.2}$, Fig. 6). In fact, the albite contents of the plagioclase are the highest of which we are aware in any lunar sample. This high albite content is not totally unprecedented though: Warren et al. (1987) reported zoned plagioclase with rims of $An_{35.5}$ in felsite 12033,507. The FeO content of the plagioclase ranges from 0.14 to 0.33 wt% with an average concentration of 0.21 wt %. These values are consistent with FeO concentrations reported for plagioclase in other lunar granites (e.g. Warren et al. 1987; Jolliff 1991). From our thick section, we are unable to determine whether the plagioclase is crystalline or maskelynite.

Quartz. The SiO_2 phase is identified as quartz on the basis of Raman spectroscopy (Fig. 8). Its texture is fractured in a hackled pattern (e.g., Jolliff et al. 1999), suggesting that it may have inverted from cristobalite. Quartz analyses with the electron microprobe give minor-oxide concentrations (Table 3), including Al_2O_3 (0.21 wt%), FeO (0.21 wt%), TiO_2 (0.05 wt%), and K_2O (0.02 wt%).

Hedenbergite. All analyzed pyroxene grains in 12032,366-19 are hedenbergite ($En_{4.6\text{-}6.2}$, $Fs_{51\text{-}52}$, $Wo_{43\text{-}44}$). In the probe mount, there are three relatively large grains: an elongate grain (670 × 56 μm; Figs. 3,4,7a) that terminates at the edge of the sample, a 196 × 134 μm grain with a sub-rounded inclusion (diameter = 58 μm; Figs. 3,4), and a 425 × 112 μm grain (Figs. 3,4). The shape of the inclusion-bearing hedenbergite grain is similar to a hopper crystal (Fig. 3). There are >20 other, smaller grains of hedenbergite in the section. The pyroxene grains are subhedral with irregular boundaries and in some cases are serrated. Six spot analyses of hedenbergite yielded minor concentrations of TiO_2 (0.69–1.28 wt%), Al_2O_3 (0.53–0.84 wt%), MnO (0.33–0.38 wt%), and Na_2O (0.07–0.14 wt%) which are common concentrations for pyroxenes in other lunar granites (Quick et al. 1977; Warren et al. 1987; Jolliff 1991). Careful examination of the 12032,366-19 Mg X-ray map indicates that the larger pyroxene grains are slightly richer in Mg (up to 2 wt% MgO) at the cores.

Fayalite. In 12032,366-19, the fayalite ($Fa_{97.3}$) grains are small (average grain size: 130 × 50 μm), and subhedral to anhedral with typically equant morphologies. The fayalite contains ~1 wt% MgO and small amounts of MnO (0.79–0.86 wt%), CaO (0.11–0.24 wt%), TiO_2 (<0.05–0.19 wt%), and P_2O_5 (0.06–0.07 wt%). These concentrations are typical of olivine compositions in other lunar granites (Quick et al. 1977; Warren et al. 1987).

Ilmenite. Ilmenite grains tend to be elongate (aspect ratio average: 13.5, range: 5.9 to 27; Fig. 7b,7c) but not to the extent of some of the zirconolite grains (see below). Ilmenite is commonly found along the boundaries of pyroxene and olivine and is typically subhedral to anhedral. Ilmenite and baddeleyite are the only minerals in the sample that exhibit a preference for occurring adjacent to another mineral. Ilmenite grains contain only 0.12 wt% MgO, lower than the MgO range observed in the ilmenite of 12013 felsic material (1.76–2.01 wt%, Quick et al. 1981). The Nb_2O_5 concentration is 0.97 wt%, whereas V_2O_5 is below the detection limit (<0.017 wt%). Both of these concentrations are similar to those of ilmenite in the granitic phase of 12013 (Quick et al. 1981).

Baddeleyite. In 12032,366-19, baddeleyite is always found in association with ilmenite, and its analyses reveal concentrations of HfO_2 of 2.8 wt% and measureable FeO (1.1 wt%), TiO_2 (0.8 wt%), and Nb_2O_5 (0.5 wt%). The largest baddeleyite grain is euhedral, 24.7 x 16.8 μm, and is highlighted in Figure 7a.

Zirconolite. Zirconolite occurs in two forms in 12032,366-19. The first consists of fine-grained, elongate “strings” (finely elongate green phase in Fig. 4b; diagonal, bright phase in Fig. 7b; and gray arrow in Fig. 7c) scattered throughout the section. These elongate grains are typically ~65 μm long and ~3 μm wide. There is only one occurrence of the second form in the studied slice of 12032,366-19. It is coarser (0.1 mm long, 0.04 mm wide) than any occurrence of the elongate form and has an irregular shape (green phase at top of Fig. 4b, false-colored X-ray image).

Zirconolite is a fairly common accessory mineral in evolved lunar rocks that has the general formula $(Ca,REE)Zr(Ti,Nb,Ta)_2O_7$. In 12032,366-19, its composition (Table 4) is similar to compositions reported by Wark et al. (1973) and Rasmussen et al. (2008) in some lunar mare basalts and breccias (Table 4); however, the composition obtained by Haines et al. (1971) for zirconolite in the 12013 granitic breccia has 12.8 wt% less ZrO_2 than that in 12032,366-19. Several of our zirconolite analyses on elongate grains imply significant concentrations of SiO_2; however, we conclude that these results are an artifact of electron beam volume overlap because the zirconolite grains are so thin. Our best analysis indicates that the zirconolite contains <0.008 wt% SiO_2.

We measured concentrations of the four REEs present in the highest concentrations (La, Ce, Nd, and Yb) and Y in our zirconolite analyses (Fig. 9), but many of the analyses resulted in low totals. The REE^{3+} concentrations of the zirconolite analyses with the lowest SiO_2 concentrations were interpolated to form a smooth, chondrite-normalized pattern with the measured REE concentrations (Fig. 9). We also assume that the Y concentration, normalized to chondrites, plots at a point halfway between normalized Ho and Er concentrations (Korotev 1996). The full REE component was then used to calculate the structural formula of the 12032,366-19 zirconolite (Table 4b). The normalized REE pattern is HREE-rich (Fig. 9) unlike the pattern of REE in the mare basalt occurrence reported by Rasmussen et al. (2008). Oxide sums, including the REE, for the four analyses with lowest silica range from 97.4% to 98.7% (Table 4a).

Zirconolite analyses were normalized on the basis of 7 oxygen atoms using the structural formula, $(\mathbf{M_I})^{2+}(\mathbf{M_{II}})^{4+}(\mathbf{M_{III}})_2^{4+}\mathbf{O_7}$, following the methods of Wark et al. (1973) as described in the experimental procedure section. The results are listed in Table

4b. Four zirconolite analyses included PbO data (Table 4a). Using Th, U, and Pb concentrations, we calculated a crystallization age of 3.9 ± 0.3 Ga (error is a 95% confidence interval).

Phosphates. Phosphates are rare in 12032,366-19, as they are in most granitic lunar samples (Warren et al. 1983c), and account for <0.3 vol% of 12032,366-19, on the basis of image analysis of a P X-ray map of the sample. Quantitative analyses reveal that three phosphate phases are present in 12032,366-19—apatite, REE-rich apatite, and RE-merrillite—all of which are anhedral to subhedral. Of the apatite grains we have measured, the compositions fall into a high-REE group (we refer to these compositions as "REE-rich apatite") and a low-REE group (we refer to these compositions as "apatite"); they do not form a continuum of REE concentrations. Because the phosphate grain sizes are small, commonly <5 µm, we disregarded analyses that indicate overlap of the electron beam interaction volume with an adjacent phase (e.g., ~1 wt% Al_2O_3 from feldspar or ~5 wt% SiO_2 from quartz). We measured concentrations of five REEs (La, Ce, Nd, Gd, and Yb) and Y in our phosphate analyses (Fig. 9). La, Ce, Nd, and Y were above detection limits in analyses of all three phosphates; Gd and Yb are above detection limits in merrillite with 15–22% and 23–32% error, respectively, and are above detection limits in about half of the REE-rich apatite analyses with 24–52% and 25–47% error, respectively. The (low REE) apatite analyses have Gd and Yb below detection limits. On a chondrite-normalized plot (Fig. 9), the analyzed LREE form a negative slope that is similar for the three phosphates. In merrillite, the analyzed HREEs have an approximately flat slope. We used the slopes of the merrillite REEs to interpolate the unanalyzed REE^{3+} concentrations. Though Gd and Yb were commonly below detection limits in the apatites, Y (and Gd and Yb when detectable) indicates that the apatite and REE-rich apatite have chondrite-normalized REE patterns that mimic the pattern of merrillite. We interpolated the concentrations of REE^{3+} in apatite that were either not analyzed or that were found to be below our detection limits using the chondrite-normalized REE pattern of merrillite scaled to the concentrations detected for the LREE and Y.

The largest grain of apatite in 12032,366-19 is 25 × 15 μm and is adjacent to an elongate zirconolite grain and quartz. In apatite, the (F, Cl, OH) site is occupied by 0.30–0.56 F and 0.17–0.23 Cl apfu (atoms per formula unit), and sums range from 0.47 to 0.78 leaving open the possibility for a missing component, possibly OH (McCubbin et al. 2010). The apatite analyses contain 1.91–2.09 wt% SiO_2 (0.16 to 0.18 apfu) which is more than enough to provide a charge balance for the 1.25–1.36 wt% $(REE,Y)_2O_3$ (0.04-0.05 apfu). We suspect that the excess SiO_2 was contributed to the analyses by secondary fluorescence of Si in adjacent quartz.

The REE-rich apatite ("RE-Ap" in Table 3, Fig. 2) contains an average of 7.2±0.4 wt% REE_2O_3 (error is 1σ). The largest occurrence of REE-rich apatite is elongate, 44 × 6 μm (Fig. 7d), but it has been fractured into segments typically with dimensions of ~5 μm or less. It contains an average of 3.2±0.2 wt% SiO_2 (error is 1σ), which corresponds to 0.29 apfu per 25 negative charges and provides charge-balance for the REEs and Y (0.31 apfu). F and Cl are also present at 0.96 ± 0.11 and 1.32 ± 0.06 wt% (0.28 and 0.21 apfu), respectively (errors are one σ) which, based on apatite stoichiometry, only occupies 42-54% of the (F, Cl, OH) site, leaving open the possibility that this grain contains significant OH.

RE-merrillite is the third phosphate present in 12032,366-19. Concentrations of F and Cl are below detection limits (<0.02 and <0.01 wt%, respectively). Only one grain was large enough (15 × 5 μm) to provide a good analysis, and it contains 5.24 wt% FeO, 0.59 wt% MgO, and 15.1 wt% $(REE+Y)_2O_3$. On the basis of our electron microprobe analyses, the REE-rich apatite has a similar chondrite-normalized REE pattern (Fig. 9) to that of the RE-merrillite but is about an order of magnitude lower in concentration.

Glass Inclusions. We observed inclusions of glass and two crystalline inclusions in pyroxene in 12032,366-19. The inclusions are rounded and located at or near the center of the pyroxene grains. All of the inclusions are glass except for the largest (diameter of 58 μm), which has crystallized to an assemblage of K-feldspar, plagioclase, and quartz, and another, which has crystallized into K-feldspar and quartz. One of the largest glass inclusions has a composition with significantly higher SiO_2 than the bulk sample (e.g., 78.3 vs. 70.1 wt% SiO_2, Table 3). The bulk composition of the largest crystalline inclusion has 70.6 wt% SiO_2; this was calculated using a modal recombination technique that assumed the inclusion-hedenbergite boundary was originally smooth, like all other inclusion-hedenbergite boundaries in the section, until the inclusion crystallized additional hedenbergite onto the boundary. The hedenbergite within the assumed boundary is included in the modal recombination.

Bulk composition

The bulk composition of 12032,366-19 as estimated from CMR and determined by INAA are listed in Table 1. The phase abundances derived from both the image analysis and the modal recombination are listed in Table 2. Notable major oxide concentrations obtained from INAA include: 4.99 wt% FeO (Fig. 10), 2.10 wt% Na_2O, and 4.8 wt% K_2O (Table 1). Only four reported lunar granitic compositions have lower bulk FeO (12023,147-10; 14321,1027; 73215,43,3; 73255,27,2; Appendix 1). Samples 14321,1027 (149 mg); 73215,43,3 (20 mg); and 73255,27,3 (2 mg) are granitic clasts and have the lowest bulk FeO (2.3, 3.0, and 3.1 wt%, respectively; references are in Appendix 1). Sample 12023,147-10 (2.67 mg) is an igneous fragment with no evidence of brecciation. It contains 3.1 wt% FeO. Clast 14303,204 (70 mg) has a bulk FeO concentration of 5.6 wt% (Warren et al. 1983c), which is the most similar to that of 12032,366-19. Sample 15434,10 (27 mg), which has an igneous texture, has the highest bulk FeO (19 wt%) of any sample identified as lunar granite (identified as such from thin section 15434,10,136; Ryder and Martinez 1991)—likely a sampling issue from the coarseness of the texture compared to the size of the 39 mg chip analyzed by INAA (Ryder and Martinez 1991). The remaining eighteen samples listed in Appendix 1 have bulk compositions that range from 6.0 to 14 wt% FeO and have been identified as granitic lunar samples. High bulk FeO is likely a result of other lithologies being mixed with granitic lithologies during the formation of granitic breccias (e.g., 12013—6 to 14 wt% FeO—is a breccia consisting of a mixture of granitic and basaltic lithologies, Quick et al. 1981; samples 14001,28.2, 14001,28.3, and 14001,28.4—9.1 to 12.2 wt% FeO—consist of clasts of granitic breccia in a ferropyroxenitic glass, Morris et al. 1990). The bulk Na_2O (2.10 wt%) of 12032,366-19 is the highest of any lunar sample of which we are aware. The second most sodic lunar granitic composition is that of breccia 14001,28.4 (1.90 wt%, Morris et al. 1990), and others have bulk Na_2O as low as 0.19 wt% (breccia 73215,43,3).

Compared to high-K KREEP (Warren 1989), Ba, Rb, Cs, Yb, Lu, Ta, W, Th, and U concentrations are high in 12032,366-19 (Fig. 11), whereas the LREE are lower by a factor of ~0.6. Iridium and Au are below INAA detection limits (<1.3 ppb and <5 ppb, respectively), consistent with an unbrecciated rock unaffected by meteoritic contamination. REE abundances and relative concentrations are unlike typical Apollo 12 mare and nonmare materials, including KREEP, but are similar to other granites and felsites, exhibiting a characteristically V-shaped chondrite-normalized REE pattern (e.g., Blanchard and Budahn 1979; Jolliff 1991; Fig. 12). In 12032,366-19, the LREE-rich RE-merrillite and REE-rich apatite and the HREE-rich zirconolite (Fig. 9) are the most likely main contributors to the V-shaped chondrite-normalized REE pattern.

DISCUSSION

Granites are one of the rarest lithologies in the Apollo collection, implying that rocks of granitic composition make up only a small fraction of the lunar crust. However, granitic samples are relatively more common among the nonmare components at Apollo 12 (five have been characterized thus far) compared to the other Apollo sites presumably because the site is located in the Procellarum KREEP Terrane (Jolliff et al. 2000), which has the highest abundances of K, Th, and U on the lunar surface (Lawrence et al. 1998). Given the high concentrations of those elements in granite, it logically follows that the source of most of the lunar granitic material would be in this terrane as well. The Apollo 14 and Apollo 15 sites also lie within this terrane, and both have yielded several granitic samples (Ryder 1976; Warren et al. 1983c; Jolliff 1991; Ryder and Martinez 1991) whereas we are aware of no granite clasts in the Apollo 16 collection. Moreover, silicic surface compositions associated with some of the "red spots" such as the Gruithuisen domes, Mairan domes, and Hansteen Alpha (Hawke et al. 2003; Wilson and Head 2003; Glotch et al. 2010), most of which are now known to be silica-rich (Glotch et al. 2010), occur within this terrane.

12032,366-19 compared to other lunar granites

Granite 12032,366-19 is of lunar origin. It is not a terrestrial contaminant or a piece of Earth blasted to the Moon (Chapman 2002). It contains no petrographic indication of hydrous alteration of any minerals (e.g., serpentinization of fayalite, sericitization of plagioclase). Micas and amphiboles are absent in 12032,366-19 (and other lunar samples) but are common in terrestrial granites.

Sample 12032,366-19 is unique among lunar samples. It contains no impact-generated glass or brecciated material, unlike many other lunar granites (Rutherford et al. 1976; Warren et al. 1983c; Morris et al. 1990; Jolliff 1991). The graphic intergrowth of K-feldspar and silica, commonly described as a granophyre, dominates most of the lunar granitic samples (e.g., 12013); however, significant amounts of plagioclase-silica intergrowths are far less common among reported samples. It is also common for lunar granites to contain shock-melted glass, but 12032,366-19 contains none. It is noteworthy that only a quarter or so of known lunar granites have pyroxene in abundances large enough to analyze, and the Mg′ (mol% Mg/[Mg+Fe]) of the pyroxene in 12032,366-19, essentially endmember hedenbergite, is significantly lower than those of other lunar granites (Fig. 13).

Perhaps because all samples are exceedingly small by terrestrial sampling and analysis standards, a wide distribution in bulk compositions characterizes rocks (and assemblages) that have been classified as lunar granites or felsites. Appendix 1 includes several granitic bulk compositions for comparison with 12032,366-19. The 12032,366-19 REE concentrations are most similar (of those to which it has been compared thus far) to those of 12001,912-02; 12013,10,28; 12023,147-10; and 12033,517, all from Apollo 12. 12032,366-19 contains the second highest concentration of BaO (0.68 wt%) of which we are aware in a lunar sample (the highest is in sample 12032,366-07, another lithic fragment of granitic composition). The most striking difference between 12032,366-19 and other lunar granites is that its Na_2O/K_2O is higher by a factor of 2–5—a characteristic reflected by both the abundance and sodic nature of its plagioclase. To our knowledge, the texture and mineral assemblage of this sample is unique among studied lunar samples.

Lunar granites (pristine or otherwise) have U-Pb crystallization ages between 3.88 and 4.32 Ga (from zircon analyses; Meyer et al. 1996). Our calculation of a crystallization age of 3.87 ± 0.28 Ga for sample 12032,366-19 is consistent with this range.

Pristinity

Although 12032,366-19 was collected on the immediate surface of the Moon, it is an unbrecciated sample with an igneous texture and contains no evidence of any admixed meteoritic or regolith material. The bulk rock concentration of Ir is low, <1.3 ppb, corresponding to <0.2% meteoritic material (H chondrite equivalent). Moreover, metallic iron and troilite are absent. Metallic Fe, depending on Ni concentrations, would also indicate a meteoritic source (Papike et al. 1991).

Shock-melted glass is a common occurrence in many lunar granitic samples (e.g., 14303,204 is a felsite clast of which half is glass; Warren et al. 1983c). It is also common for veins of impact glass to cut through portions of granitic samples (e.g., 12033,507;

Warren et al. 1987). The only glass in 12032,366-19 occurs as inclusions in hedenbergite and does not appear to be of shock-melted origin (though the sample is a thick section which precludes an assessment by transmitted light microscopy). These glass inclusions are more likely to be melt that became trapped within an early forming crystal. The granitic composition of the inclusion glass indicates that the hedenbergite was in equilibrium with the granite melt. The texture of 12032,366-19 indicates that the rock only experienced one episode of crystallization and has not experienced any re-melting since.

ZrO_2 – SiO_2 phase boundary

In sample 12032,366-19, baddeleyite (monoclinic) is in physical contact with quartz (Fig. 7a). The ZrO_2–SiO_2 phase diagram generated by Kaiser et al. 2008 indicates that ZrO_2 (tetragonal) and SiO_2 (cristobalite) are only stable together between 1673°C and 1687°C. At lower temperatures, the phases should react to form zircon. Baddeleyite and silica may have crystallized metastably. Alternatively, given that in 12032,366-19 baddeleyite always occurs in contact with ilmenite, it may have crystallized by the diffusion of Zr out of ilmenite. Terrestrially, this process has been used to explain zircon rims around ilmenite grains (e.g., Morisset and Scoates 2008). It may also be responsible for the intimate intergrowth of zircon and ilmenite in the Apollo 12 high-Th impact melt beccias (Liu et al. 2012). Although the diffusion of Zr out of ilmenite explains the co-occurrence of baddeleyite and ilmenite in 12032,366-19, it does not explain why baddeleyite, instead of zircon, crystallized in the presence of abundant SiO_2.

Petrogenesis

The following three methods of producing granitic compositions in the low-fO_2, low-pressure conditions near the lunar surface have been suggested: (1) high SiO_2 achieved by fractional crystallization of an evolved parent such as KREEP basalt or basaltic andesite glass (e.g., Longhi 1990); (2) high SiO_2 achieved by SLI (silicate liquid immiscibility; e.g., Hess et al. 1975; Rutherford et al. 1976; Neal and Taylor 1989; Jolliff 1991); and (3) partial melting of an enriched crustal protolith (e.g., KREEP basalt) by basaltic underplating (e.g., Lawrence et al. 2005; Hagerty et al. 2006). SLI, which does not occur without being preceded by extensive fractional crystallization, tends to form very high SiO_2 (68–80 wt%), low CaO (1–6.5 wt%), and low FeO (3–7.5 wt%) compositions (Table 5; though SLI can produce compositions with ~61 wt% SiO_2 at high pressure (3 kbar), Holmberg and Rutherford 1994)—similar to the bulk composition of 12032,366-19 (Table 1). Process (3), coupled with upward enrichment of high-silica melt is a common process on Earth, leading to the formation of bimodal volcanics, i.e., basalt and rhyolite. We see this situation perhaps reflected in the lunar granitic breccia 12013. In the same vein, on the Moon, we do not see intermediate compositions (with SiO_2 between 52 and 70 wt%) when there should be more of the intermediate silica materials than high silica if (1) were the main process. We explore the methods of producing lunar granitic material, considering their ability to produce lithologies like 12032,366-19.

12032,366-19 contains K-feldspar, quartz, alkali-rich plagioclase, Fe-pyroxene, and Fe-olivine—a representative mineral assemblage consistent with late-stage fractional crystallization. These phases have relatively low crystallization temperatures compared to Mg-pyroxenes and Mg-olivine and indicate crystallization from a liquid that had already exhausted most of its Mg and was therefore in the extreme late stages of fractionation. The incompatible trace elements in 12032,366-19 are high compared to KREEP (Fig. 11). The concentrations of these elements in the liquid become higher as crystallization continues, and it logically follows that 12032,366-19 crystallized from a liquid that was at a late stage of fractional crystallization in order to explain such high concentrations of incompatible elements. This indication of the late-stage nature of the parent melt is consistent with the near absence of phosphates. Phosphorus is an incompatible element, and phosphates tend to crystallize late in the fractional crystallization sequence (Hess and Rutherford 1974, Hess et al. 1975, Warren et al. 1983c, Jolliff 1991, and Jolliff et al. 1999). Since phosphate in 12032,366-19 is present at only a trace level, the parent melt may have crystallized phosphates as part of a residual assemblage that was presumably segregated and left behind during gravity separation of the granitic mass, as hypothesized by Jolliff (1991). Separation of minerals that concentrated the middle REE (merrillite and apatite) explains the V-shaped REE pattern as a result of early phosphate crystallization, which would impart a middle REE depletion relative to the LREE and HREE on remaining residual melt. Alternatively, the parent melt may have had low P content compared to KREEP basalt.

Petrogenetic modeling

The texture of 12032,366-19 shows no direct (relict) evidence of liquid immiscibility—except, perhaps, the glass inclusions with ~78 wt% SiO_2 within hedenbergite (see below)—such as that seen in sample 14161,373 (a mafic assemblage containing rounded segregations of K-feldspar and SiO_2; Jolliff 1991, Jolliff et al. 1999). We tested whether the bulk composition could be achieved simply by fractional crystallization of a melt with a KREEP-like composition. We selected KREEP basalt (KB) 15434,18,199-A (composition compiled by Papike et al. 1998) and basaltic andesite glass (BAG) of Zeigler et al. (2006) as compositions to represent potential parent melts because both compositions (Table 5) represent alkali-rich melts that could plausibly have fractionally crystallized to produce felsic final assemblages. Compared to the KB composition, the BAG composition has higher Fe/Mg (2.8 vs. 1.4) and lower Al_2O_3 (12.9 vs. 15.2 wt%), but the SiO_2 contents are similar (BAG: 52.5 wt%; KB: 52.8 wt%). The compositions were modeled using MAGFOX (Longhi 1991) by extended fractional crystallization reaching 89.4 wt% crystallized (for KB) and 85.4 wt% crystallized (for BAG). The paths followed by the residual liquids for KB and BAG and the phases crystallizing at each stage of melt evolution are described in detail in Appendix 3 and depicted in Appendix Figure 1 of Appendix 3. The compositions, temperatures, and viscosities of the KB and BAG residual liquids at ~25 wt% crystallization intervals are given in Table 6. In order to compare the residual melt compositions and crystallizing phases generated by our fractional crystallization modeling with the results of experimental fractional crystallization of KREEP basalt 15386 (Holmberg and Rutherford 1994), we modeled the fractional crystallization of KREEP basalt 15386 (results in Appendix 3).

Both the KB and BAG crystallization models have several shortcomings. Neither KB nor BAG produce, upon fractional crystallization, residual melt compositions as rich in SiO_2 (57.5 wt% and 55.1 wt%, respectively; Fig. 14 and Appendix Figure 1 of Appendix 3) as observed in the granite (70.1 wt%)%), at least not at a stage when there is enough liquid left for plausible separation of melt from crystals. Low oxygen fugacity relevant to the lunar system prevents crystallization of magnetite, which in terrestrial liquid compositions occurs early and halts the FeO-enrichment trend, and causes the SiO_2 concentration of residual melt to increase to produce rhyolitic liquid compositions (e.g., Hess et al., 1975). Under lunar fO_2 and low water content, FeO-rich residual melts would typically reach the field of silicate-liquid immiscibility prior to onset of Fe-Ti oxide crystallization. Both models drive TiO_2 to very low levels by the 80–85% solidification stage (this may be an artifact of the model), yet in 12032,366-19, ilmenite is present and the bulk TiO_2 is 1.07 wt%. FeO concentrations in the model residual melts at this point are 12.3 wt% (KB) and 15.3 wt% (BAG), which is roughly three times that of 12032,366-19 (4.98 wt%). K_2O in 12032,366-19 (4.58 wt%) is similar to that predicted by the models (5.0 wt%, KB and 3.9 wt%, BAG). KB and BAG produce P_2O_5 of 2.9 wt% (KB) and 3.4 wt% (BAG) while that of 12032,366-19 is only 0.052 wt%. Also, the anorthite contents of KB ($An_{62.6}$) and BAG ($An_{62.5}$) are higher than that of 12032,366-19 ($An_{34.9}$). Most importantly, K-feldspar does not saturate in either the KB or BAG models. The crystallizing mineral assemblages at the 80-85% solidification stage of the KB and BAG models would be tonalitic based on QAPF classification (Appendix Figure 1 of Appendix 3); however, if the normative K-feldspar from the residual liquid is included in the classification, the mineral assemblage for both models is that of quartz monzonite with bulk SiO_2 of ~50 wt%.

Silicate liquid immiscibility

As noted above, a key failure of extended fractional crystallization is that it does not generate SiO_2 concentrations in residual melts as high as observed in the granite (~70 wt%) while there is still a significant proportion of residual melt. Moreover the process of extended fractional crystallization should produce intermediate evolved compositions in greater volumes than granite, yet such compositions are not observed on the Moon. In fact, evolved lunar rock compositions generally have bimodal distributions with respect to silica content (Hess et al. 1975; Rutherford et al. 1976). Also, the absence of intermediate lunar lithologies, something akin to terrestrial granodiorite (or dacite), which would be produced as a melt progressed from crystallizing mafic rocks to felsic rocks implies that another process may have occurred (Rutherford et al. 1976).

Silicate liquid immiscibility has long been suggested as a process responsible for the production of lunar granites while at the same time accounting for the absence of intermediate lithologies (e.g., Hess et al. 1975; Rutherford et al. 1976; Neal and Taylor 1989; Jolliff 1991). SLI is a process that can occur as a melt undergoes fractional crystallization. As crystallization proceeds and melt becomes progressively richer in Si, Fe, and incompatible elements, the melt can ultimately reach a composition that unmixes when the melt enters the field of SLI (Fig. 14). This process has been observed in the laboratory (Hess et al. 1975, Rutherford et al. 1976) and in nature (e.g., Skaergaard, Jakobsen et al. 2005; Bushveld, Lee 1979). One of the liquids is Fe-rich and incorporates the REE- and P-rich fraction of KREEP, which, if it separates physically from the felsic fraction, crystallizes as monzogabbro or monzodiorite. The complementary liquid is rich in Si and K, and if it separates physically from the Fe-rich liquid, would crystallize to a felsic or granitic assemblage (Rutherford et al. 1976; Taylor et al. 1980; Jolliff 1991; Table 5).

SLI could feasibly be combined with the fractional crystallization model to explain the bulk composition of 12032,366-19 in the following way: a parent melt of composition similar to BAG or KB undergoes extensive fractional crystallization until it reaches a point where SLI occurs (Fig. 14). As the melt unmixes into two liquids, the denser, Fe-rich liquid remains with the crystallizing (gabbroic) assemblage, and the lower-density felsic liquid rises and separates from the gabbroic fraction. Finally, the granitic liquid continues to crystallize producing the bulk composition of 12032,366-19. However, in our models, as the KB composition crystallizes, it does not pass into the field of SLI, and BAG only grazes the boundary of the field before trending away from it (Fig. 14). This leads us to search for other possibilities to explain the petrogenesis of 12032,366-19 and to consider the possibility that we do not have the right starting composition. We acknowledge that the boundaries of field of immiscibility drawn by Roedder (1951; Fig. 14) are probably only an estimation of where the field actually is. The modeling of KREEP basalt 15386 suggests that the residual liquid passes close to the field of immiscibility without entering it similar to the KB model (Fig. 14); whereas the experimental work of Holmberg and Rutherford (1994) did result in SLI after ~70% crystallization implying that though KB does not enter the SLI field of Roedder (1951), experimental fractional crystallization of the KB composition may result in immiscible liquids.

Although SLI has been observed to occur on a small (micro) scale in lunar rocks, including mare basalts (Roedder and Weiblen 1970; Roedder and Weiblen 1971; Roedder and Weiblen 1972) and monzogabbro (Jolliff 1991), it is not clear that SLI could or did occur on a scale large enough to produce some of the large silicic volcanic constructs on the Moon such as the Gruithuisen domes, the Mairan domes, and Hansteen Alpha (Glotch et al. 2010). Partial melting produced by basaltic “underplating” has been suggested as an alternative process that could produce significant amounts of granitic material (Lawrence et al. 2005; Hagerty et al. 2006). This process involves the injection of basaltic magma into the lunar crust and partial melting of the overlying crustal material, which then intrudes to a shallow level, forming granite, or extrudes onto the surface as a large volume of rhyolitic material without producing intermediate lithologies. The efficacy of this process depends on the composition of the crust at the point of intrusion of basaltic melt and on the rheology and transport of the silica-rich material upward from the zone where it is formed. If the crust was anorthositic, it is unlikely that basaltic underplating would lead to a significant amount of melting because of the high melting point of anorthosite. If, however, basaltic melt intruded into a crust of KREEP-basalt or similar composition, which has a melting point around 1000º C (Holmberg and Rutherford 1994), and if the crust in this region was already hot, then partial melting would have been much more likely and more volumetrically significant. A lithology like 12032,366-19 could be produced from ~10-15% partial melting of a KREEP basalt.

The glass inclusions with ~78 wt% SiO_2 within hedenbergite could be explained as a product of local SLI. A liquid with the composition of the glass inclusion combined with a relatively small amount of hedenbergite and a liquid with the composition of hedenbergite combined with the glass inclusion would be complementary liquids consistent with the miscibility gap of Roedder (1951). However, The glass inclusion composition could also be the result of the crystallization of hedenbergite from an inclusion with the bulk composition of 12032,366-19 onto the inner walls of the host hedenbergite grain. A third explanation appeals to the vagaries of late stage fractional crystallization.

Gravity separation of phases

If we take the mineral compositions that are in equilibrium with the KREEP basalt and BAG residual melts at the latest stages of fractional crystallization as modeled above and adjust the proportions by increasing the low-density phases relative to the high-density phases, as might occur during gravity-induced separation or flow differentiation, we can achieve the compositions of the pristine granites without appealing to SLI (Fig. 15; Columns 10 and 11, Table 7). For this gravity separation model, we add the K-feldspar from calculating the normative mineralogy of the residual liquid at the final stages of the KB and BAG models to the mineral assemblages predicted by the KB and BAG models. To obtain the pristine granite compositions, the concentrations of K-feldspar and quartz modeled above must be increased by factors of 1.3 to 1.5 and 4.0 to 4.2, respectively. Accompanying the increased K-feldspar and quartz is a depletion of mafic silicates and phosphates owing to density differentiation or separation. An exception for 12032,366-19 is its high Na_2O, which requires a more sodic plagioclase and an additional 0.3–0.5 wt% Na_2O content in either the KB or BAG starting melt composition in order for the crystallizing plagioclase to have ~$An_{33.5}$ to match that contained in the sample.

The obvious problem for this model is how to separate phases after a high degree of crystallization and at relatively high silica contents when the viscosity of the system is very high. The viscosities of the residual liquids of the KB and BAG models, calculated using the KWare Magma program (Ken Wohletz, Version 2.49.0126) and the methods of Shaw (1972) and Bottinga and Weill (1972), become as high as ~67000 and ~3500 Pa·s, respectively, at the end stages of the KB and BAG models. Separation of phases is also a problem in the case of the two liquids produced by SLI because the Si-rich phase similarly has a very high viscosity. Separation of the mafic and felsic phases in the lunar magmatic environment was not assisted by tectonic forces and processes involving significant concentrations of magmatic water as it is in terrestrial environments. The high-viscosity, silica-rich phase does not need to flow, it simply needs to rise through the much lower-viscosity mafic residual melt. Perhaps crustal movements related to large impacts that occurred during the time of upper-crustal magmatism played a role in the segregation of these phases, for example, movement along faults or uplifts associated with basin ring formation, or movement related to isostatic adjustments following an impact and associated flow segregation.

Equilibrium crystallization and SLI

Given that the fractional crystallization of KB and BAG produces residual liquid compositional trajectories that do not intersect or barely intersect the field of SLI (Fig. 14), we investigated what effect equilibrium crystallization would have on KB. Crystallization modeling done using the MAGPOX program (Longhi 1991) indicates that a liquid with the initial composition of KB is driven into the field of SLI (Roedder 1951) after 56 wt% of crystallization in equilibrium with the crystallizing solids. Granitic compositions could be produced from the crystallization of a liquid of KB composition if the first 50% of crystallization occurred in equilibrium with the solids. If the immiscible liquids were physically separated, then the silicic liquid would solidify to produce a rock with ~70 wt% bulk SiO_2 (terrestrial examples include the silicic immiscible liquid compositions in Table 5).

IMPLICATIONS

Remote sensing data, Earth-based (near-IR reflectance spectra) and orbital (images from Clementine and LRO; spectra from Lunar Prospector gamma-ray spectrometer and LRO Diviner radiometer), have provided evidence for regions of silicic volcanism on the Moon. Sample 12032,366-19 (an igneous rock rich with K-feldspar, quartz, and plagioclase, along with near Fe end-member mafic minerals) is a candidate to be among the lunar samples most similar to the rocks that compose some of the lunar "red spots." Glotch et al. (2010) identified several of the red spots as regions of high-SiO_2 content from the Christiansen Feature in the LRO Diviner data. Perhaps the 12032,366-19 mineralogy is relevant to interpreting some of the features seen at the silicic volcanic complex that lies at the center of the Compton-Belkovich Th-anomaly (Jolliff et al. 2011), which has been modeled to have a Th concentration of 40-55 ppm (Lawrence et al. 2003). This concentration is similar to that for the bulk sample of 12032,366-19 (60.6 ppm) as well as other lunar granites (Appendix 1).

ACKNOWLEDGEMENTS

We thank Paul Carpenter for his assistance with trace element analysis on the electron microprobe and insight into Zr-Ti phases. We thank Alian Wang and Weigang Kong for Raman spectroscopic measurements. We are grateful to G. Jeffrey Taylor and Malcolm J. Rutherford for their insightful reviews of this paper. This work was funded by NASA grant NNG04GG10G (RLK).

References Cited

Anders E. and Grevesse N. (1989) Abundances of the elements: meteoritic and solar. Geochimica et Cosmochimica Acta, 53, 197-214.

Barra, F., Swindle, T.D., Korotev, R.L., Jolliff, B.L., Zeigler, R.A., and Olson, E. (2006) ^{40}Ar-^{39}Ar dating on Apollo 12 regolith: Implications on the age of Copernicus and the source of non-mare materials. Geochimica et Cosmochimica Acta, 70, 6016–6031.

Blanchard, D.P., J.W. Jacobs, and J.C. Brannon (1977) Chemistry of ANT-suite and felsite clasts from the consortium breccia 73215 and of gabbroic anorthosite 79215. Procedings of the 8th Lunar and Planetary Science Conference, 2507-2524.

Blanchard, D.P. and J.R. Budahn (1979) Remnants from the ancient lunar crust: clasts from consortium breccia 73255. Procedings of the 10th Lunar and Planetary Science Conference, 803-816.

Bottinga, Y.A. and Weill, D.F. (1972) The viscosity of magmatic silicate liquids: a model for calculation. American Journal of Science, 272, 438-473.

Brown, G.M., Emeleus, C.H., Holland, J.G., and Phillips, R. (1970) Mineralogical, Chemical and petrological features of Apollo 11 rocks and their relationship to igneous processes. Proceedings of the Apollo 11 Lunar Science Conference, 195–219.

Carpenter, P., Counce, D., Kluk, E., and Nabelek, C. (2002) Characterization of Corning EPMA Standard Glasses 95IRV, 95IRW, and 95IRX. Journal of Research of the National Institute of Standards and Technology, 107, 703-718.

Chapman, C.R. (2002) Earth’s lunar attic. Nature, 419, 791-794.

Deer, W.A., Howie, R.A., and Zussman, J. (1976) An Introduction to the Rock Forming Minerals. Longman Group Limited, London.

Dence, M.R., Douglas, J.A.V., Plant, A.G., and Traill, R.J. (1970) Petrology, mineralogy and deformation of Apollo 11 samples. Proceedings of the Apollo 11 Lunar Science Conference, 315–340.

Downs, R.T. (2006) The RRUFF Project: an integrated study of the chemistry, crystallography, Raman and infrared spectroscopy of minerals. Program and Abstracts of the 19th General Meeting of the International Mineralogical Association in Kobe, Japan. O03-13.

Drake, M.J., and Weill, D.F. (1972) New rare earth element standards for electron microprobe analysis, Chemical Geology, 10, 179-181.

Freeman, J.J., Wang,A., Kuebler, K.E, Haskin, L.A. (2008) Characterization of natural feldspar by Raman spectroscopy for future planetary exploration. Canadian Mineralogist, 46, 1477–1500.

Glotch, T.D., Lucey, P.G., Bandfield, J.L., Greenhagen, B.T., Thomas, I.R., Elphic, R.C., Bowles, N., Wyatt, M.B., Allen, C.C., Hanna, K.D., Paige, D.A. (2010) Highly silicic compositions on the Moon. Science, 329, 1510.

Haines, E.L., Albee, A.L., Chodos, A.A., and Wasserburg, G.J. (1971) Uranium-bearing minerals of lunar rock 12013. Earth and Planetary Science Letters, 12, 145-154.

Hagerty, J.J., Lawrence, D.J., Hawke, B.R., Vaniman, D.T., Elphic, R.C., and Feldman, W.C. (2006) Refined thorium abundances for lunar red spots: Implications for evolved, nonmare volcanism on the Moon. Journal of Geophysical Research, 111, E06002.

Hawke, B.R., Lawrence, D.J., Blewett, D.T., Lucey, P.G., Smith, G.A., Spudis, P.D., and Taylor, G.J. (2003), Hansteen Alpha: A volcanic construct in the lunar highlands, Journal of Geophysical Research, 108, 5069.

Hess, P.C. and Rutherford, M.J. (1974) Element fractionation between immiscible melts. Abstracts of the Lunar and Planetary Science Conference, 5, 328-330.

Hess, P.C., Rutherford, M.J., Guillemette, R.N., Ryerson, F.J., and Tuchfeld, H.A. (1975) Residual products of fractional crystallization of lunar magmas - an experimental study. Proceedings of the 6th Lunar Science Conference, 895-909.

Holmberg, B. and Rutherford, M.J. (1994) An experimental study of KREEP basalt evolution. Abstracts of the 25th Lunar and Planetary Science Conference, 557.

Hovington, P., Drouin, D., and Gauvin, R. (1997) CASINO: A new Monte Carlo code in C language for electron beam interaction—Part I: Description of the program. Scanning,19, 1-14.

Hubbard, N.J., P.W. Gast, and H. Wiesmann (1970) Rare earth alkaline and alkali metal and 87/86 Sr data for sub-samples of lunar sample 12013. Earth and Planetary Science Letters, 9, 181-184.

Jaffey, A.H., Flynn, K.F., Glendenin, L.E., Bentley, W.C., and Essling, A.M. (1971) Precision measurement of half-lives and specific activities of ^{235}U and ^{238}U. Physical Review C: Nuclear Physics, 4, 1889-1906.

Jakobsen, J.K., Veksler, I.V., Tegner, C., and Brooks, C.K. (2005) Immiscible iron- and silica-rich melts in basalt petrogenesis documented in the Skaergaard intrusion. Geology, 33, 885-888.

Jarosewich, E., Nelen, J.A., and Norberg, J.A. (1980) Reference samples for electron microprobe analysis. Geostandards Newsletter, 4, 43–47.

Jolliff, B.L. (1991) Fragments of quartz monzodiorite and felsite in Apollo 14 soil particles. Proceedings of the 21st Lunar and Planetary Science Conference, 101–118.

Jolliff, B.L., Floss, C., McCallum, I.S., and Schwartz, J.M. (1999) Geochemistry, petrology, and cooling history of 14161, 7373: A plutonic lunar sample with textural evidence of granitic-fraction separation by silicate-liquid immiscibility. American Mineralogist, 84, 821-837.

Jolliff, B.L., Gillis, J.J., Haskin, L.A., Korotev, R.L., and Wieczorek, M.A. (2000) Major lunar crustal terranes: Surface expressions and crust-mantle origins. Journal of Geophysical Research: Planets, 105, 4197-4216.

Jolliff, B.L., Korotev, R.L., and Haskin, L.A. (1991) Geochemistry of 2-4-mm particles from Apollo 14 soil (14161) and implications regarding igneous components and soil-forming processes. Proceedings of the 21st Lunar and Planetary Science Conference, 193–219.

Jolliff, B.L., Wiseman, S.A., Lawrence, S.J., Tran, T.N., Robinson, M.S., Sato, H., Hawke, B.R., Scholten, F., Oberst, J., Hiesinger, H., van der Bogert, C.H., Greenhagen, B.T., Glotch, T.D., and Paige, D.A. (2011) Non-mare silicic volcanism on the lunar farside at Compton-Belkovich. Nature Geoscience, 4, 566-571.

Kaiser, A., Lobert, M., and Telle, R. (2008) Thermal stability of zircon ($ZrSiO_4$). Journal of the European Ceramic Society, 28, 2199-2211.

Keil, K. and Prinz, M. (1971) Mineralogy and composition of Apollo 11 lunar samples. Proceedings of the Second Lunar Science Conference, 319-341.

Keil, K., Bunch, T.E., and Prinz, M. (1970) Mineralogy and composition of Apollo 11 lunar samples. Proceedings of the Apollo 11 Lunar Science Conference, 561–598.

Korotev, R.L. (1996) A self-consistent compilation of elemental concentration data for 93 geochemical reference samples. Geostandards Newsletter, 20, 217–245.

Korotev, R.L., Jolliff, B.L., Zeigler, R.A., Seddio, S.M., and Haskin, L.A. (2011) Apollo 12 revisited. Geochimica et Cosmochimica Acta, 75, 1540-1573.

Krasov, N.F. and Clocchiatti, R. (1979). Immiscibility in silicate melts and its possible petrogenetic importance, as shown by study of melt inclusions. Transactions (Doklady) of the USSR Academy of Sciences, 248, 92-95.

Lawrence, D.J., Hawke, B.R., Hagerty, J.J., Elphic, R.C., Feldman, W.C., Prettyman, T.H., and Vaniman, D.T. (2005) Evidence for a high-Th, evolved lithology on the Moon at Hansteen Alpha. Geophysical Research Letters, 32, L07201.

Lawrence, D.J., Feldman, W.C., Barraclough, B.L., Binder, A.B., Elphic, R.C., Maurice, S., and Thomsen, D.R. (1998) Global elemental maps of the moon: The Lunar Prospector Gamma-Ray Spectrometer. Science, 281, 1484.

Laul, J.C. (1986) Chemistry of the Apollo 12 highland component. Proceedings of the 16th Lunar and Planetary Science Conference, D251–D261.

Lee, C.A. (1979) Spheroidal pyroxenite aggregates in the Bushveld Complex — a special case of silicate liquid immiscibility. Earth and Planetary Science Letters, 44, 295-310.

LeRoux, L.J. and Glendenin, L.E. (1963) Half-life of ^{232}Th. Proceedings of the National Meeting on Nuclear Energy, Pretoria, South Africa, 83-94.

Liu, D., Jolliff, B.L., Zeigler, R.A., Korotev, R.L., Wan, Y., Xie, H., Zhang, Y., Dong, C., and Wang, W. (2012) Comparative zircon U-Pb geochronology of impact melt breccias from Apollo 12 and lunar meteorite SaU 169, and the age of the Imbrium impact. Earth and Planetary Science Letters, 319-320, 277-286.

Longhi, J. (1990) Silicate liquid immiscibility in isothermal crystallization experiments. Proceedings of the 20th Lunar and Planetary Science Conference, 13-24.

Longhi, J. (1991) Comparative liquidus equilibria of hypersthene-normative basalts at low pressure. American Mineralogist, 76, 785-800.

Marvin, U.B., Wood, J. A., Taylor, G. J., Reid Jr., J. B., Powell, B. N., Dickey Jr., J. S., and Bower, J. F. (1971) Relative proportions and probable sources of rock fragments in the Apollo 12 soil samples. Proceedings of the Second Lunar Science Conference, 679-699.

McCubbin, F.M., Steele, A., Nekvasil, H., Schnieders, A., Rose, T., Fries, M., Carpenter, P.K., and Jolliff, B.L. (2010) Detection of structurally bound hydroxyl in fluorapatite from Apollo Mare basalt 15058,128 using TOF-SIMS. American Mineralogist, 95, 1141-1150.

Meyer, C., Williams, I.S., and Compston, W. (1996) Uranium-lead ages for lunar zircons: Evidence for a prolonged period of granophyre formation from 4.32 to 3.88 Ga. Meteoritics and Planetary Science, 21, 370-387.

Montel, J.-M., Foret, S., Veschambre, M., Nicollet, C., and Provost, A. (1996) Chemical Geology., 131, 37-53.

Morgan, J.W. and Ehman, W.D. (1970) Lunar rock 12013; O, Si, Al and Fe abundances. Earth and Planetary Science Letters, 9, 164.

Morisset, C.-E., and Scoates, J.S. (2008) Origin of zircon rims around ilmenite in mafic plutonic rocks of proterozoic anorthosite suites. Canadian Mineralogist, 46, 289-304.

Morris, R.W., Taylor, G.J., Newsom, H.E., and Keil, K. (1990) Highly evolved and ultramafic lithologies from Apollo 14 soils. Proceedings of the 20th Lunar and Planetary Science Conference, 61–75.

Neal, C.R., and Taylor, L.A. (1989), The nature of barium partitioning between immiscible melts: A comparison of experimental and natural systems with reference to lunar granite petrogenesis. Proceedings of the 19th Lunar and Planetary Science Conference, 19th, 209.

Papike, J.J., Ryder, G., and Shearer, C.K. (1998) Lunar samples. Planetary Materials, Reviews in Mineralogy, 36, 5-1.

Papike, J.J., Taylor, L., and Simon, S. (1991) Lunar minerals. The Lunar Sourcebook, Cambridge University Press, 121-181.

Philpotts, A.R. (1981). Liquid immiscibility in silicate melt inclusions in plagioclase phenocrysts. Bulletin de Mine¤ralogie, 104, 317-324.

Philpotts, A.R. (1982). Compositions of immiscible liquids in volcanic rocks. Contributions to Mineralogy and Petrology, 80, 201-218.

Quick, J.E., Albee, A.L., Ma, M.-S., Murali, A.V., and Schmitt, R.A. (1977) Chemical compositions and possible immiscibility of two silicate melts in 12013. Procedings of the 8th Lunar and Planetary Science Conference, 2153-2189.

Quick, J.E., James, O.B., and Albee, A.L. (1981) Petrology and petrogenesis of lunar breccia 12013. Proceedings of the 12th Lunar and Planetary Science Conference, 117-172

Rasmussen, B., Fletcher, I.R., and Muhling, J.R. (2008) Pb/Pb geochronology, petrography and chemistry of Zr-rich accessory minerals (zirconolite, tranquillityite and baddeleyite) in mare basalt 10047. Geochimica et Cosmochimica Acta, 72, 5799-5818.

Roedder, E. (1951) Low temperature liquid immiscibility in the system K_2O-FeO-Al_2O_3-SiO_2. American Mineralogist, 36, 282-286. Proceedings of the 3rd Lunar Science Conference, 251-279.

Roedder, E. and Weiblen, P.W. (1970) Lunar pertrology of silicate melt inclusions, Apollo 11 rocks. Proceedings of the Apollo 11 Lunar Science Conference, 801-837.

Roedder, E. and Weiblen, P.W. (1971) Petrology of silicate melt inclusions, Apollo 11 and Apollo 12 and terrestrial equivalents. Proceedings of the Second Lunar Science Conference, 801-837.

Roedder, E. and Weiblen, P.W. (1972) Petrographic features and petrologic significance of melt inclusions in Apollo 14 and 15 rocks. Proceedings of the Third Lunar Science Conference, 801-837.

Rutherford, M.J., Hess, P.C., Ryerson, F.J., Campbell, H.W., and Dick, P.A. (1976) The chemistry, origin and petrogenetic implications of lunar granite and monzonite. Proceedings of the 7th Lunar Science Conference, 1723-1740.

Ryabov, V.V. (1989). Liquation in Natural Glasses: the Example of Traps. Novosibirsk: Nauka.

Ryder, G. (1976) Lunar sample 15405: remnant of a KREEP basalt-granite differentiated pluton. Earth and Planetary Science Letters, 29, 255-268.

Ryder, G. and Martinez, R.R. (1991) Evolved hypabyssal rocks from Station 7, Apennine Front, Apollo 15. Proceedings of the 21st Lunar and Planetary Science Conference, 137-150.

Schnetzler, C.C., J.A. Philpotts, and M.L. Bottino (1970) Li, K, Rb, Sr, Ba and rare-earth concentrations, and Rb-Sr age of lunar rock 12013. Earth and Planetary Science Letters, 9, 185-192.

Seddio, S.M., Korotev, R.L., Jolliff, B.L., and Zeigler, R.A. (2009) Petrographic diversity in Apollo 12 regolith rock particles**.** Lunar and Planetary Science Conference XL. Lunar and Planetary Institute, Houston. #2415 (abstract).

Shaw, H.R. (1972) Viscosities of magmatic silicate liquids: an empirical method of prediction. American Journal of Science, 272, 870-893.

Snyder, G.A., Taylor, L.T., Liu, Y-.G., and Schmitt, R.A. (1992) Petrogenesis of the western highlands of the moon - Evidence from a diverse group of whitlockite-rich rocks from the Fra Mauro formation. Proceedings of Lunar and Planetary Science, 22, 399-416.

Stormer, J.C., Pierson, M.L., and Tacker, R.C., (1993) Variation of F-X-ray and Cl-X-ray intensity due to anisotropic diffusion in apatite during electron-microprobe analysis. American Mineralogist, 78, 641-648.

Taylor, G.J., Warner, R.D., Keil, K., Ma, M.-S., and Schmitt, R.A. (1980) Silicate liquid immiscibility, evolved lunar rocks and the formation of KREEP. Proceedings of the Conference of the Lunar Highlands Crust, 339-352.

Wakita, H. and Schmitt, R.A. (1970) Elemental abundances in seven fragments from lunar rock 12013. Earth and Planetary Science Letters, 9, 169-176.

Wark, D.A, Reid, A.F., Lovering, J.F., and El Goresy, A. (1973) Zirconolite (versus zirkelite) in lunar rocks. Abstracts of the Lunar and Planetary Science Conference, 4, 764 (abstract).

Warren, P.H. (1989) KREEP: major-element diversity, trace-element uniformity (almost). Workshop on Moon in Transition: Apollo 14, KREEP, and Evolved Lunar Rocks, 149-153 (abstract).

Warren, P.H., Jerde, E.A., and Kallemeyn, G.W. (1987) Pristine Moon rocks: a “large” felsite and a metal-rich ferroan anorthosite. Proceedings of the 17th Lunar and Planetary Science Conference, E303–E313.

Warren, P.H., Taylor, G.J., Keil, K., Kallemeyn, G.W., Rosener, P.S., and Wasson, J.T. (1983a) Sixth foray for pristine nonmare rocks and an assessment of the diversity of lunar anorthosites. Proceedings of the 13th Lunar and Planetary Science Conference, A615-A630.

Warren, P.H., Taylor, G.J., Keil, K., Kallemeyn, G.W., Shirley, D.N., and Wasson, J.T. (1983b) Seventh Foray - Whitlockite-rich lithologies, a diopside-bearing troctolitic anorthosite, ferroan anorthosites, and KREEP. Proceedings of the 14th Lunar and Planetary Science Conference, B151–B164.

Warren, P.H., Taylor, G.J., Keil, K., Shirley, D.N., and Wasson, J.T. (1983c) Petrology and chemistry of two 'large' granite clasts from the moon. Earth and Planetary Science Letters, 64, 175–185.

Wilson, L., and Head, J.W. (2003), Lunar Gruithuisen and Mairan domes: Rheology and mode of emplacement. Journal of Geophysical Research, 108, 5012.

Zeigler, R.A., Korotev, R.L., Jolliff, B.L., Haskin, L.A., and Floss, C. (2006) The geochemistry and provenance of Apollo 16 mafic glasses. Geochimica et Cosmochimica Acta, 70, 6050-6067.

Figure Captions

Figure 1. Photograph of sample 12032,366-19 top (a) and bottom (b) with a 1-mm grid in the background. K-feldspar, plagioclase, and silica appear white. Hedenbergite, fayalite, and ilmenite are the dark phases.

Figure 2. Positive linear time dependence of F X-ray count-rates (counts per second). Solid lines are best fit lines. Curved, dashed lines represent the 95% confidence envelope. Parts “a” and “b” are analyses of the REE-rich apatite. Part “c” is an analysis of apatite. Part “d” is an analysis of the Durango fluorapatite (Jarosewich et al. 1980) standard. Parts “a”, “b”, and “c” were analyzed with a 2 µm beam diameter and a 25 nA probe current. Part “d” was analyzed with a 20 µm beam diameter and a 25 nA probe current.

Figure 3. Back-scattered electron (BSE) image mosaic of 12032,366-19. In order of brightness from darkest to brightest, minerals are quartz, sodic plagioclase, K-feldspar, hedenbergite, fayalite and ilmenite, and zirconolite and baddeleyite. Note that the inclusion-bearing hedenbergite grain in the lower right appears to be a hopper crystal. See Fig. 4 for phase identifications based on X-ray analysis.

Figure 4. **a.** An RGB image of 12032,366-19 with K in the red channel, Na in the green channel, and Fe in the blue channel. With this color scheme, K-feldspar is orange, more sodic K-feldspar is light orange, plagioclase is green, olivine is bright blue, pyroxene is darker blue, and quartz is represented as black. **b.** An RGBGray image of 12032,366-19 with Ca in the red channel, Zr in the green channel, Ti in the blue channel, and Si in the gray channel. With this color scheme, pyroxene is pink, plagioclase is dull pink, ilmenite is blue, zirconolite and ZrO_2 are green.

Figure 5. Three BSE images of the largest zirconolite grain taken at varying accelerating voltages of 5, 15, and 25 kV. Arrow "x" points to a region that is covered by a thin layer of K-feldspar. Arrow "y" points to a region where the zirconolite is thin. The thin layers become transparent in the images taken at higher accelerating voltages since the backscattered electrons penetrate deeper into the sample at higher accelerating voltages.

Figure 6. Feldspar ternary diagram showing the K-feldspar and plagioclase compositions found in 12032,366-19. The composition has been normalized to An, Ab, and Or. The celsian (Cn) component is represented by the symbol shade. Vectors indicate the feldspar composition changes as crystallization progressed.

Figure 7. BSE images of textures in 12032,366-19. We enhanced the contrast in all 4 BSE images to the same extent so that the same phases in each image have the same brightness. Hd = hedenbergite, Kfs = K-feldspar, Fa = Fayalite, Ilm = ilmenite, Qz = quartz, and Pl = plagioclase. **a**. The large medium-gray phase transects the image is hedenbergite. The white arrow points to an ilmenite of a typical grain size in this sample. The black arrow points to the largest occurrence of baddeleyite in 12032,366-19. The baddeleyite is bordered mostly by a coarse ilmenite grain and silica to a lesser extent. **b.** An elongate example of zirconolite lies diagonally in the center of the image and is nearly paralleled by another occurrence in the bottom left. **c.** The white arrow points to the irregularly-shaped occurrence of zirconolite discussed in text. The gray arrow points to another occurrence of zirconolite. **d.** The white arrow points to the largest phosphate occurrence; it is REE-rich apatite (Table 3).

Figure 8. Raman spectra of quartz in 12032,366-19. The “Standard” spectrum is from the RRUFF™ Project (Downs 2006) database.

Figure 9. REE plots of zirconolite (shaded gray) and merrillite (shaded gray with diagonal lines) in 12032,366-19. The gray regions are the ranges of concentrations for the four zirconolite analyses with the lowest SiO_2 and the two merrillite analyses; the black solid lines represent the average concentrations. Yttrium is plotted with the REEs (Korotev 1996). The analyzed elements are indicated on the horizontal axis. *Gd was analyzed on merrillite but not zirconolite. The other REE concentrations were estimated (see text). Europium is assumed to be present in low concentration assuming the zirconolite and merrillite crystallized after plagioclase. Chondrite values are those of Anders and Grevesse (1989) for CI chondrites multiplied by a factor of 1.36 to maintain consistent values with older literature, in which data were normalized to ordinary chondrites (Korotev 1996).

Figure 10. Compositional diagram for Apollo 12 rock fragments (after Fig. 3 of Korotev et al. 2011). Sample 12032,366-19 is shown by the star, plotting at just over 60 ppm Th. The color of each symbol corresponds to the Ba (red channel), Zr (green channel), and Cr (blue channel) concentrations. The granites and a few other points that are riched in Ba relative to Zr are readily distinguished from those that have normal KREEP-like Ba/Zr (light green).

Figure 11. Bulk elemental concentrations of 12032,366-19 compared to High-K KREEP (Warren 1989).

Figure 12. Compared to typical Apollo 12 regolith (Korotev et al. 2011), 12032,366-19 has a "V"-shaped REE pattern common to lunar granitic materials (12013, Quick et al. 1977; 12033,517,Warren et al. 1987; 14161,7269, Jolliff et al. 1991; 14303,206, Warren et al. 1983b; 14321,1028, Warren et al. 1983a; 15434,10, Ryder and Martinez 1991; and 73255,27, Blanchard and Budahn 1979). 14303,206 (Warren et al. 1983b) has a REE pattern similar to the typical Apollo 12 soil. Chondrite values are those of Anders and Grevesse (1989) for CI chondrites multiplied by a factor of 1.36 to maintain consistent values with older literature, in which data were normalized to ordinary chondrites (Korotev 1996). The analyzed elements are indicated on the horizontal axis; the other REE concentrations were estimated (see text). Samples with "*" include Dy; samples with "**" include Dy and Ho. Ce was estimated for 14161,7269.

Figure 13. Mg# of pyroxenes in lunar granites (12032,366-19; 12033,507; 14303,204; 15405,12; and 15434,10) and two quartz-monzogabbros (14161,7069 and 14161,7373) plotted against the An content of the plagioclase in the same samples. The coexisting pyroxene and plagioclase from fractional crystallization modeling is also plotted. The earlier crystallization is in the upper-right and crystallization proceeds down to the lower-left. The KB starting composition produced 3 pyroxenes; the BAG starting composition produced 2 pyroxenes. The gray rectangle represents the region occupied by 14303,204; 15405,12; and 15434,10, which each considerably overlap each other. 12033,507 and 14303,204 (Warren et al. 1987). 14161,7069 and 14161,7373 (Jolliff 1991). 15405,12 (Ryder 1976). 15434,10 (Ryder and Martinez 1991).

Figure 14. Ternary diagram illustrating the compositional paths that the KB and BAG residual melt compositions follow during fractional crystallization. Note that the BAG path barely intersects the field of SLI, while the KB path does not intersect it. The granitic compositions (natural and experimental) of Table 7 are also plotted. All units are in wt%. The field of SLI is an estimation based on the experimental work of Roedder (1951).

Figure 15. Illustration depicting a gravity separation model that could have produced a mineralogy like that of 12032,366-19 without requiring SLI.

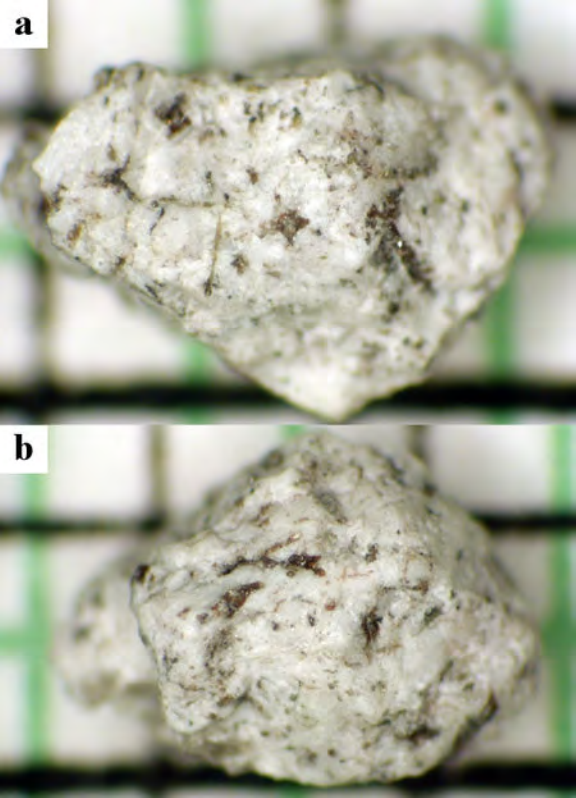
a
b

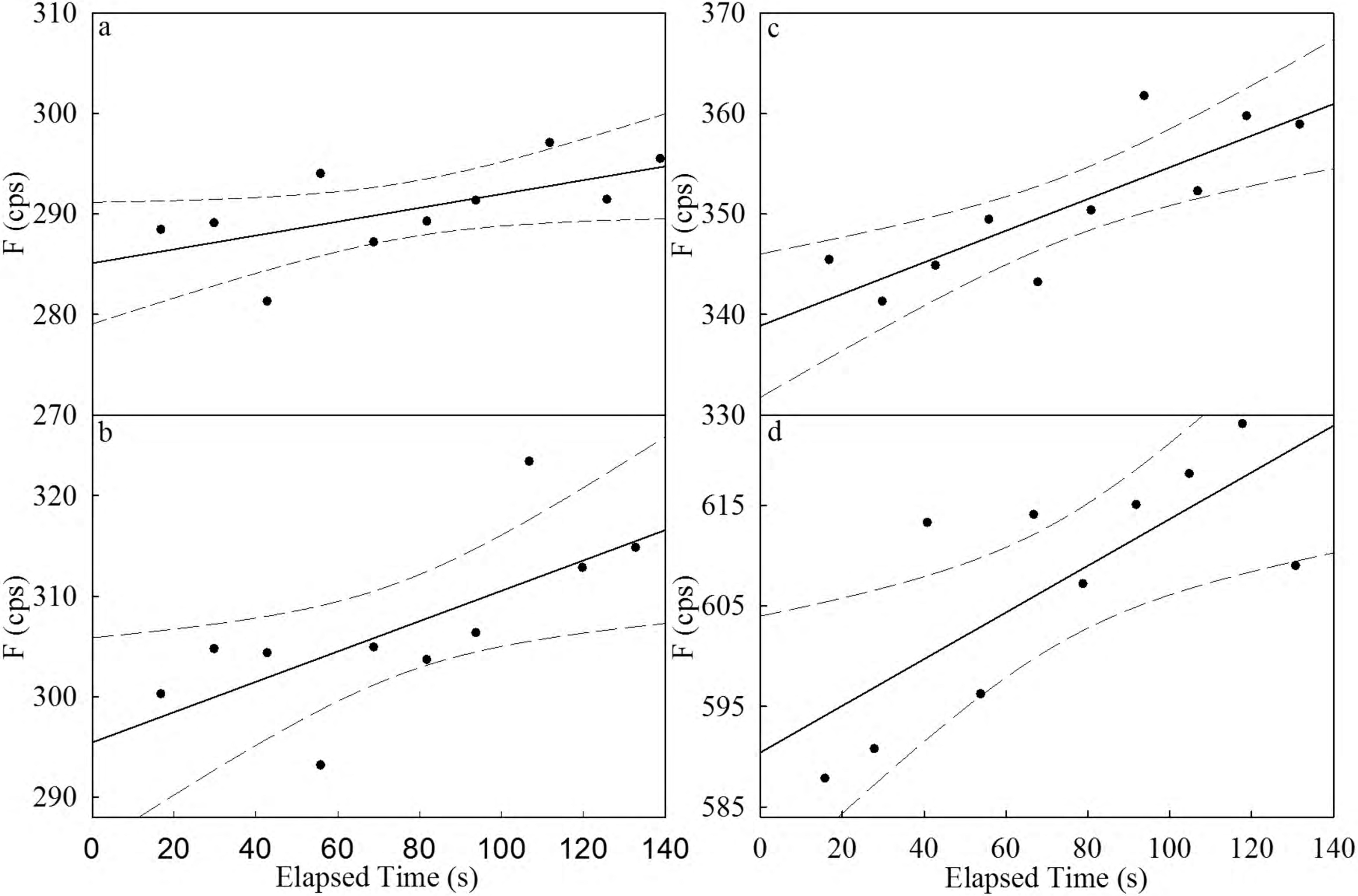
a
b
c
d
F (cps)
F (cps)
F (cps)
F (cps)
310
300
290
280
270
320
310
300
290
370
360
350
340
330
615
605
595
585
0
20
40
60
80
100
120
140
Elapsed Time (s)
Elapsed Time (s)

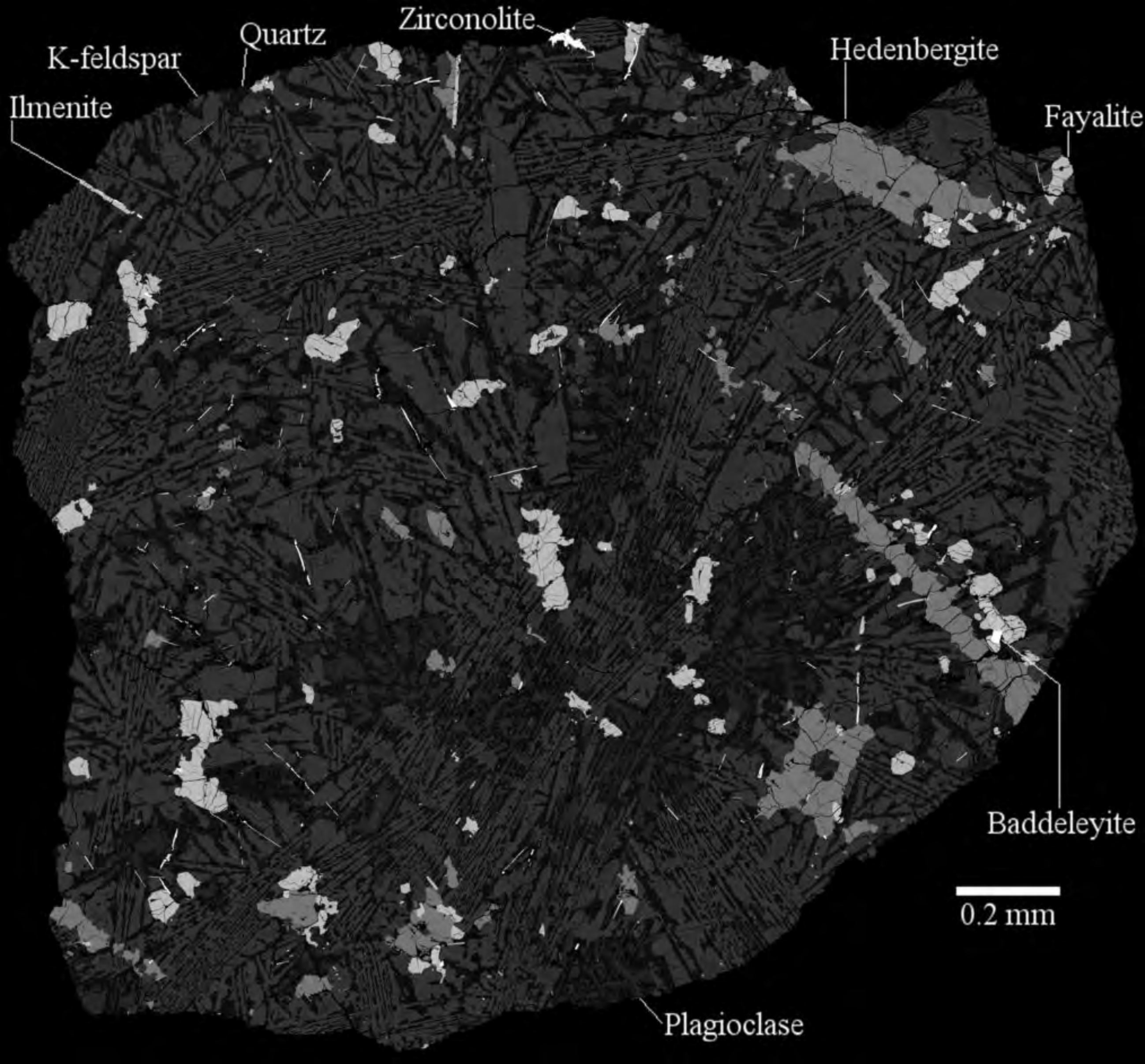
Zirconolite
Quartz
K-feldspar
Ilmenite
Hedenbergite
Fayalite
Baddeleyite
0.2 mm
Plagioclase

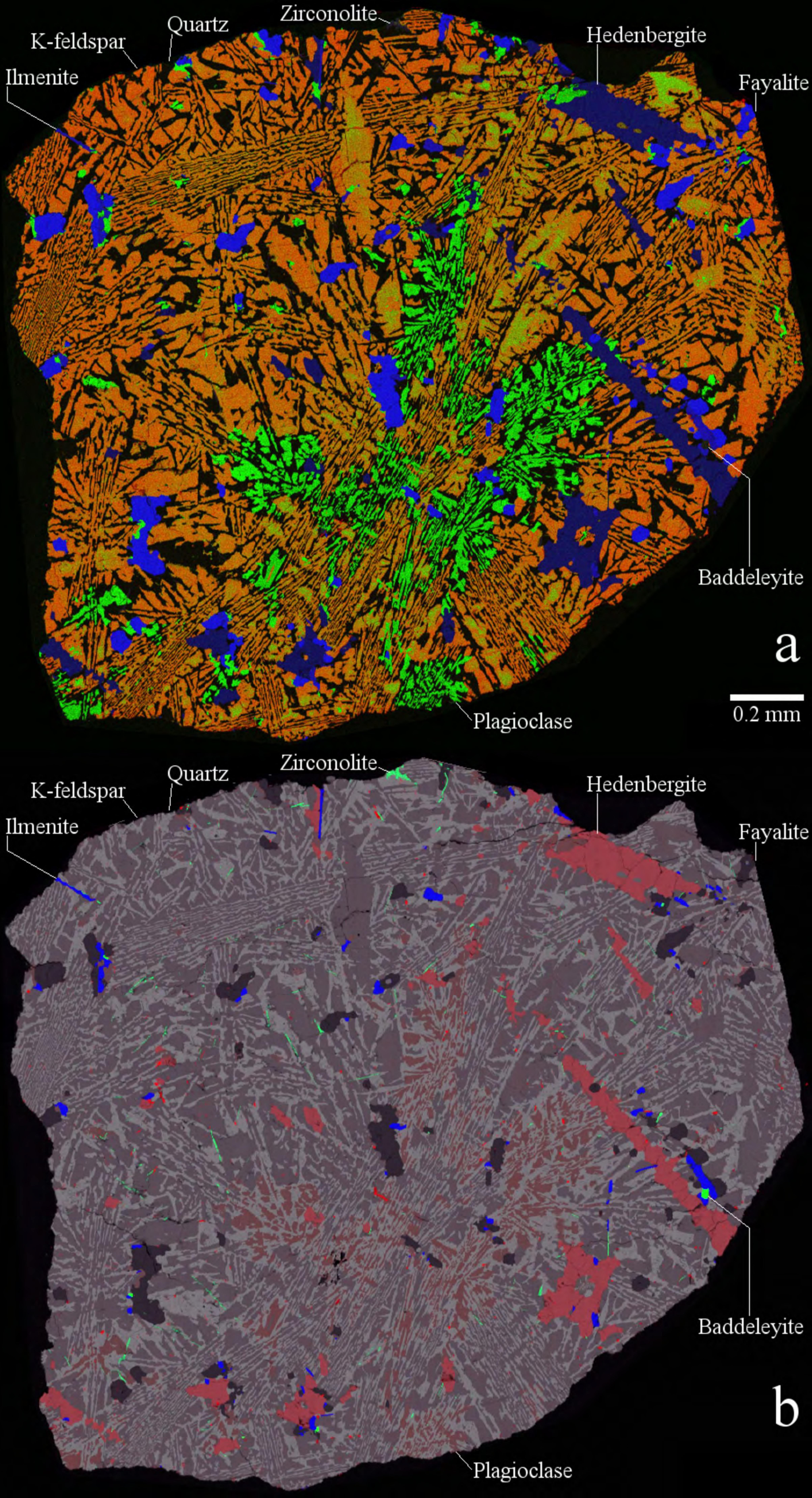
Zirconolite
Quartz
K-feldspar
Ilmenite
Hedenbergite
Fayalite
Baddeleyite
a
0.2 mm
Plagioclase
Zirconolite
Quartz
K-feldspar
Ilmenite
Hedenbergite
Fayalite
Baddeleyite
b
Plagioclase

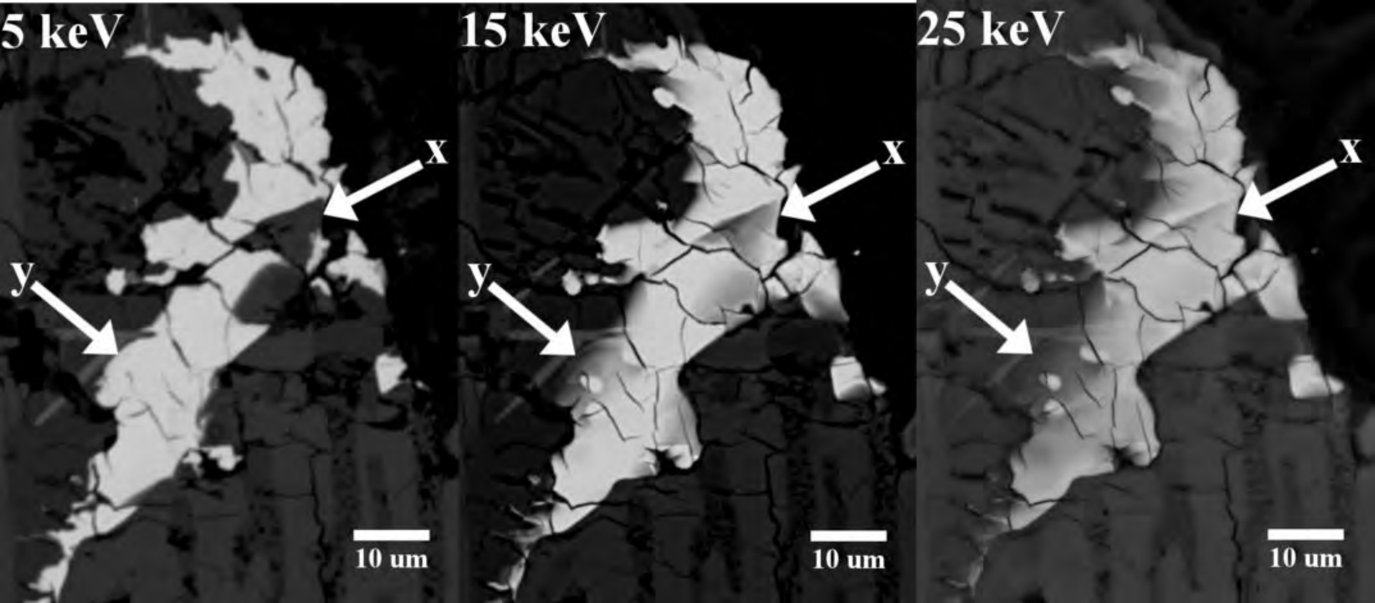
5 keV
15 keV
25 keV
x
x
x
y
y
y
10 um
10 um
10 um

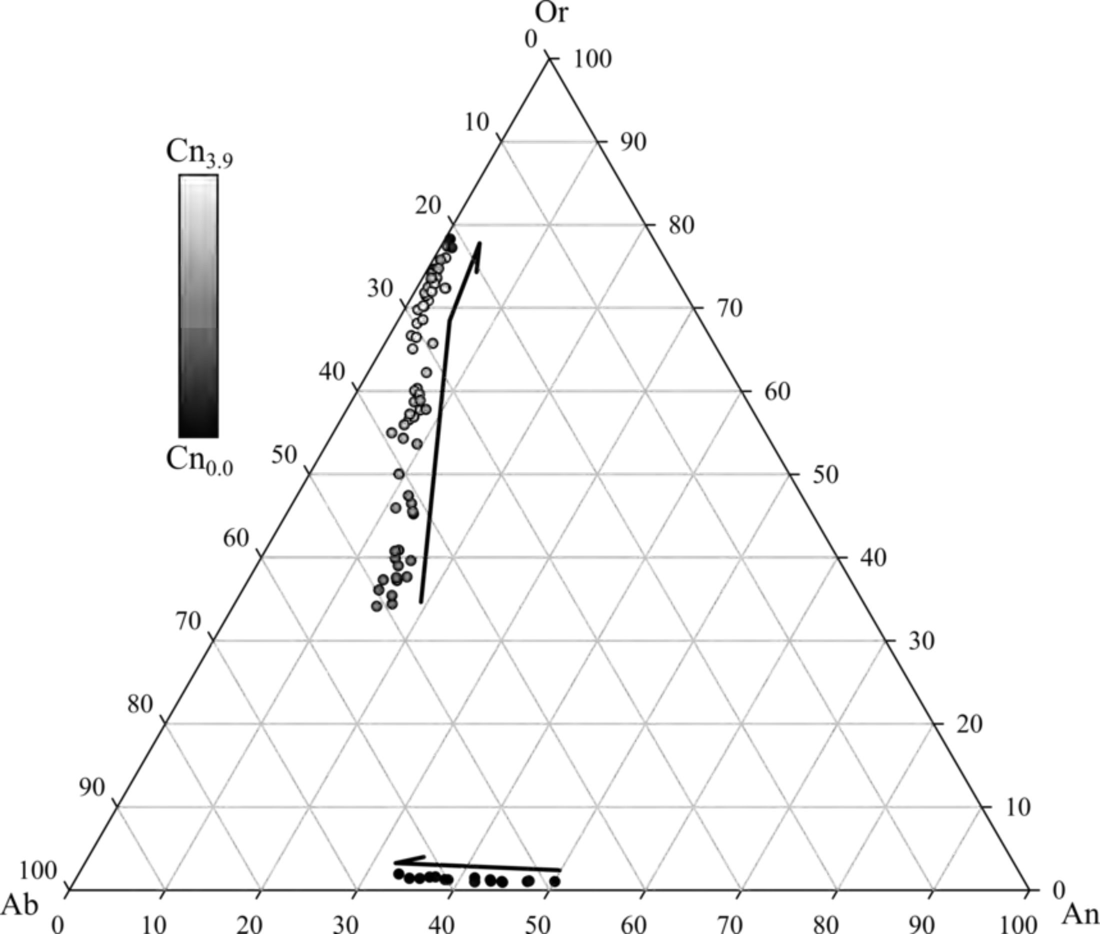
Or
Ab
An
Cn3.9
Cn0.0
0
10
20
30
40
50
60
70
80
90
100

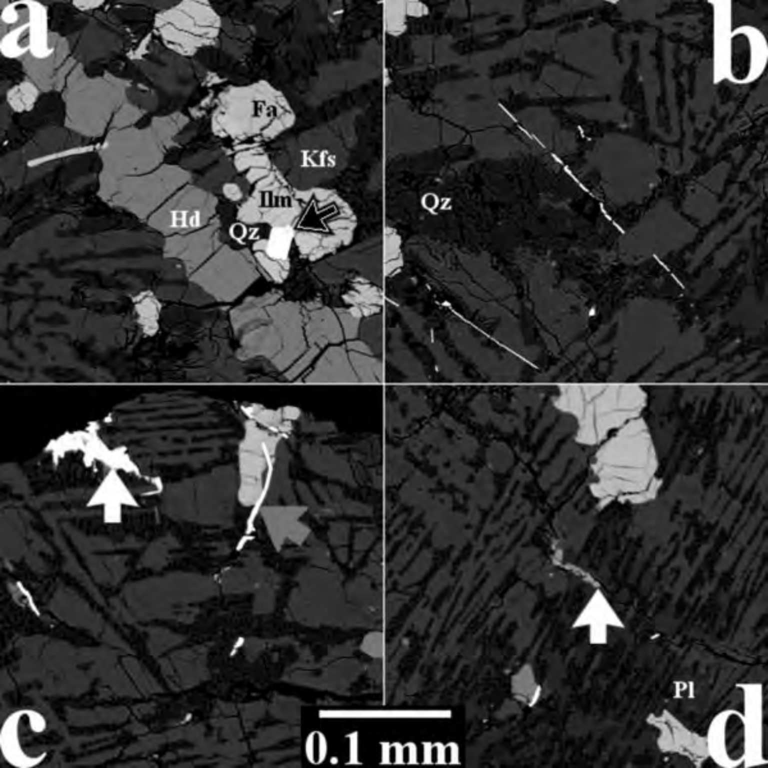
a
Fa
Kfs
Ilm
Hd
Qz
b
Qz
c
0.1 mm
Pl
d

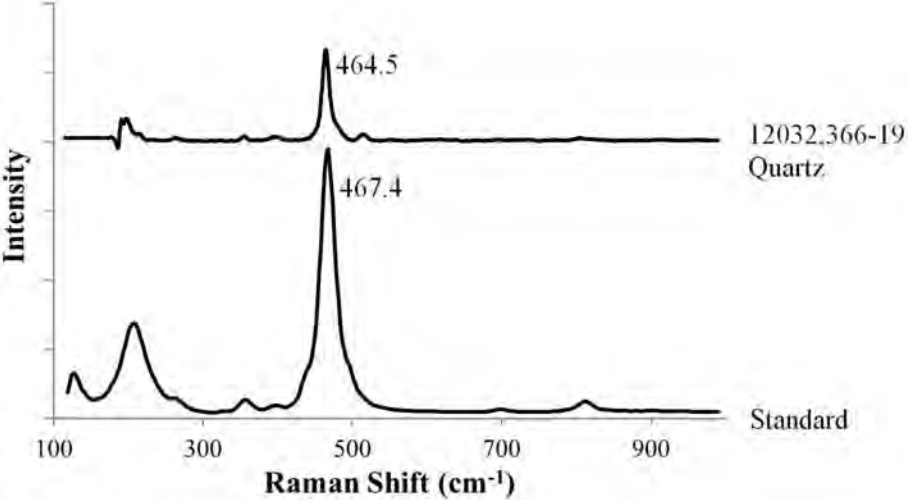
464.5
467.4
12032,366-19
Quartz
Standard
Intensity
100
300
500
700
900
Raman Shift (cm-1)

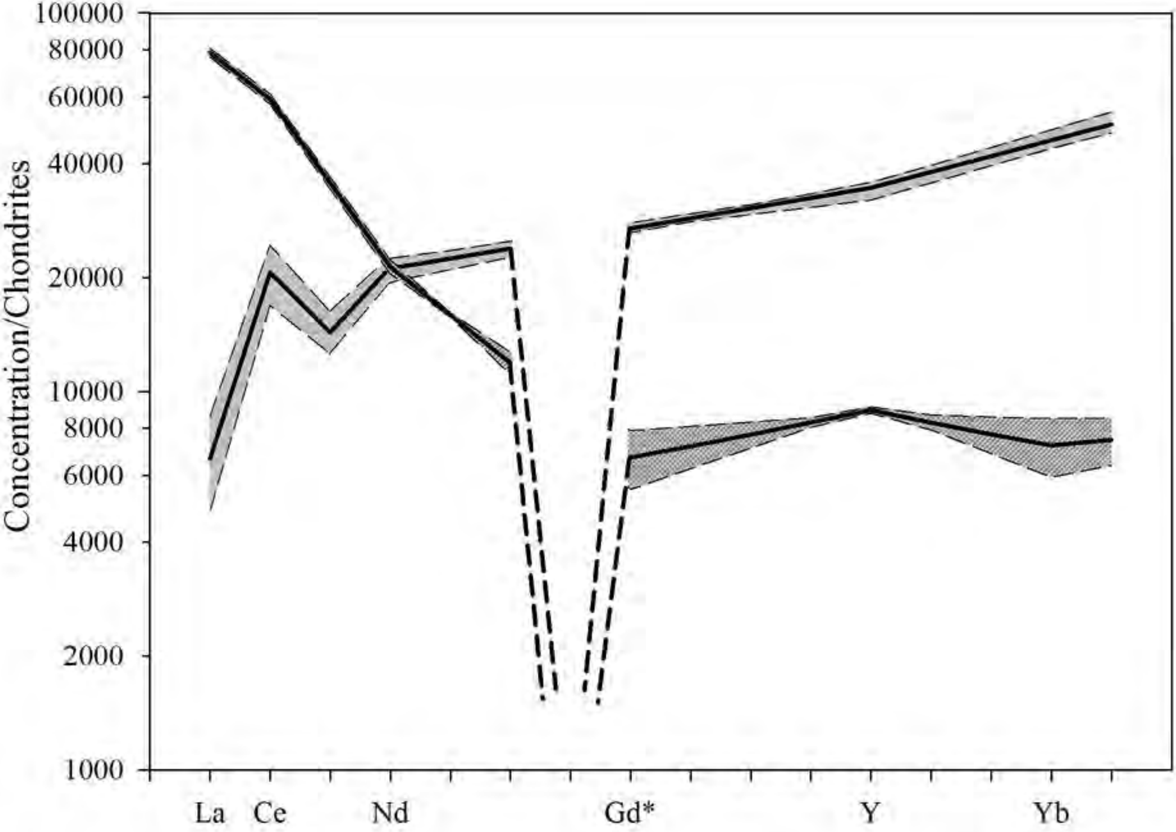
Concentration/Chondrites
100000
80000
60000
40000
20000
10000
8000
6000
4000
2000
1000
La
Ce
Nd
Gd*
Y
Yb

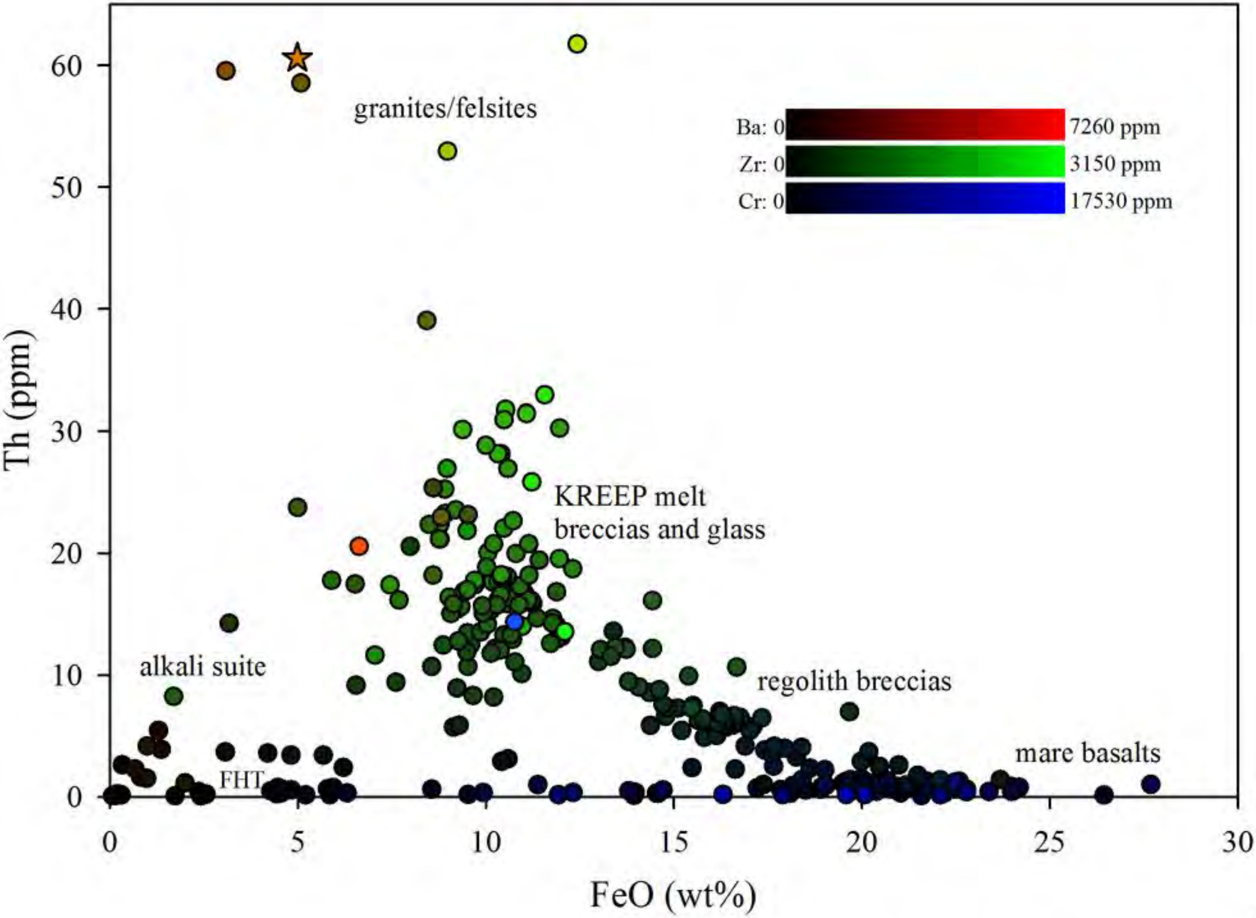
granites/felsites
KREEP melt breccias and glass
alkali suite
regolith breccias
mare basalts
FHT
Ba: 0
7260 ppm
Zr: 0
3150 ppm
Cr: 0
17530 ppm
Th (ppm)
FeO (wt%)
0
10
20
30
40
50
60
0
5
10
15
20
25
30

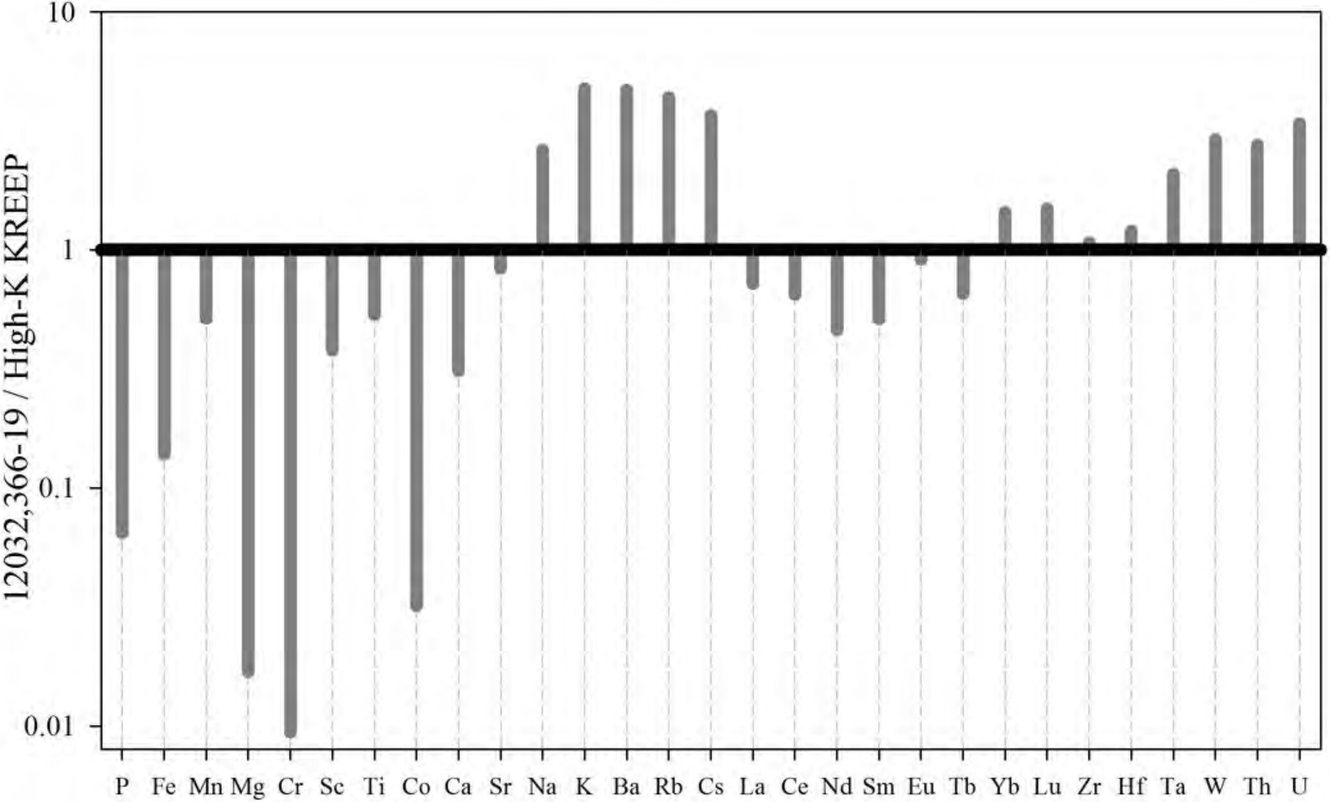
12032,366-19 / High-K KREEP
10
1
0.1
0.01
P
Fe
Mn
Mg
Cr
Sc
Ti
Co
Ca
Sr
Na
K
Ba
Rb
Cs
La
Ce
Nd
Sm
Eu
Tb
Yb
Lu
Zr
Hf
Ta
W
Th
U

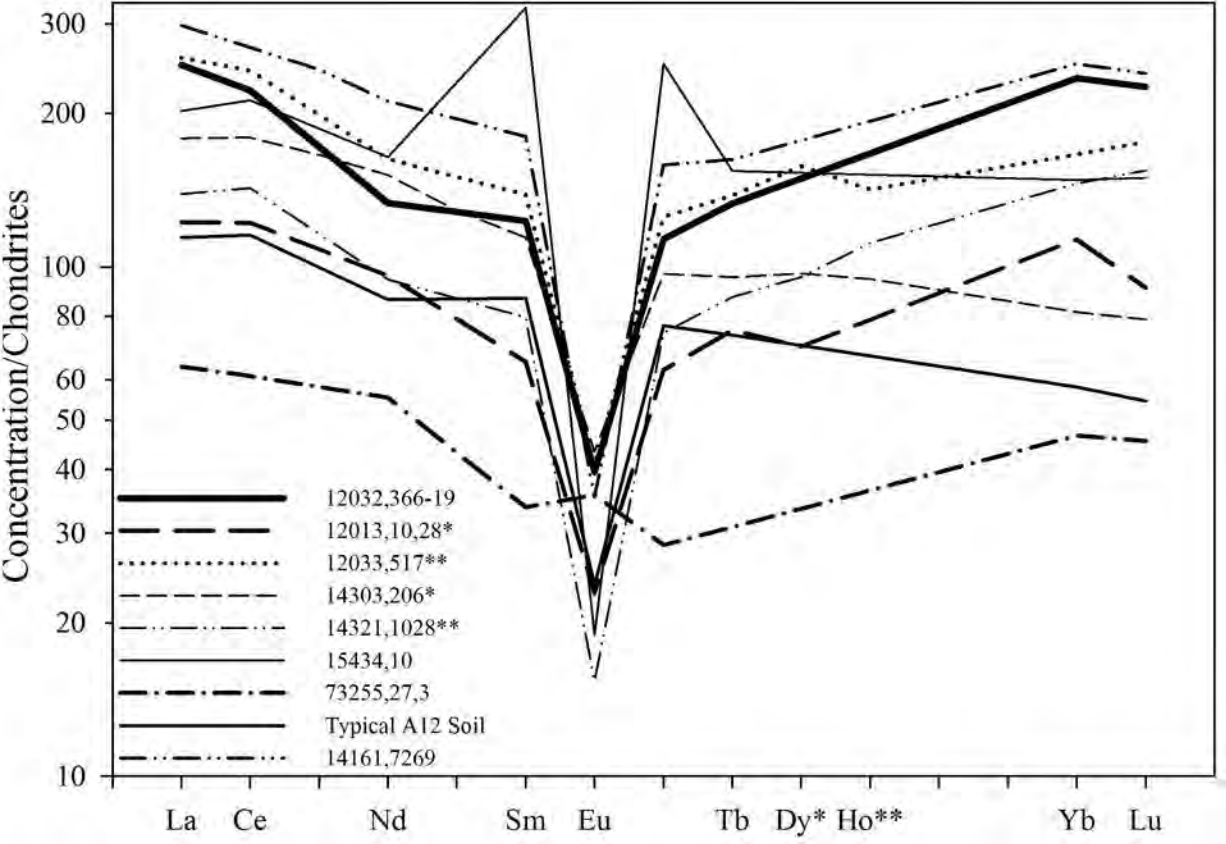
Concentration/Chondrites
300
200
100
80
60
50
40
30
20
10
La
Ce
Nd
Sm
Eu
Tb
Dy*
Ho**
Yb
Lu
12032,366-19
12013,10,28*
12033,517**
14303,206*
14321,1028**
15434,10
73255,27,3
Typical A12 Soil
14161,7269

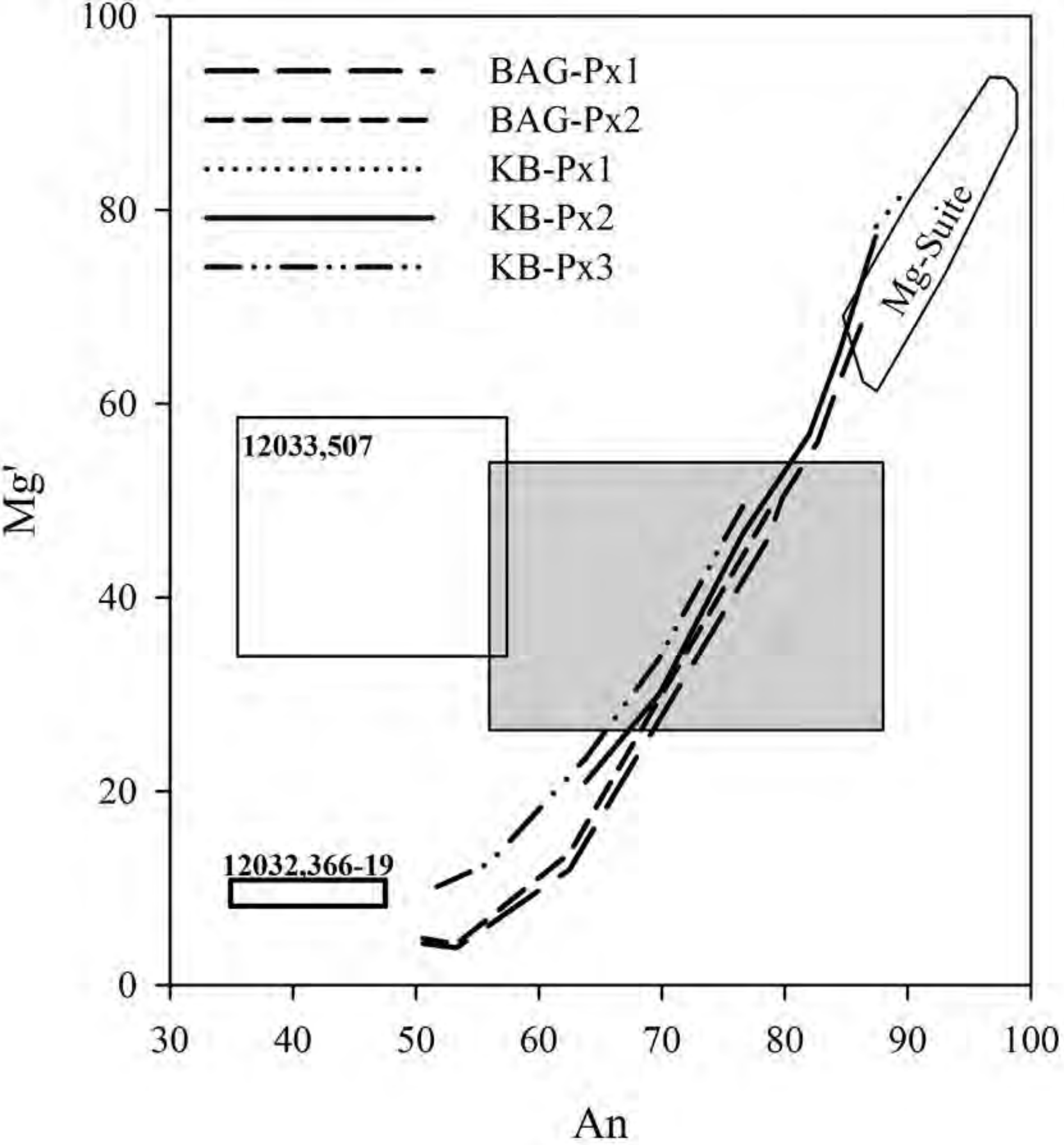
100
80
60
40
20
0
Mg'
30
40
50
60
70
80
90
100
An
BAG-Px1
BAG-Px2
KB-Px1
KB-Px2
KB-Px3
Mg-Suite
12033,507
12032,366-19

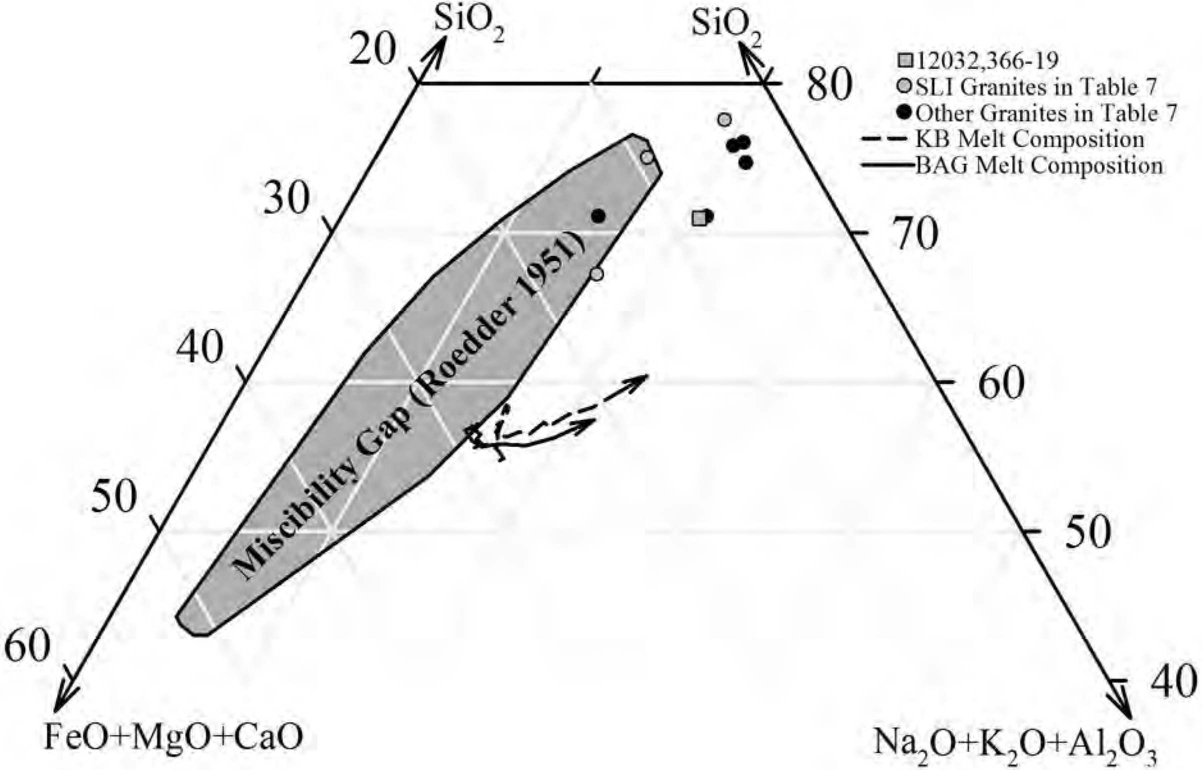
SiO₂
SiO₂
20
30
40
50
60
80
70
60
50
40
FeO+MgO+CaO
Na₂O+K₂O+Al₂O₃
Miscibility Gap (Roedder 1951)
12032,366-19
SLI Granites in Table 7
Other Granites in Table 7
KB Melt Composition
BAG Melt Composition

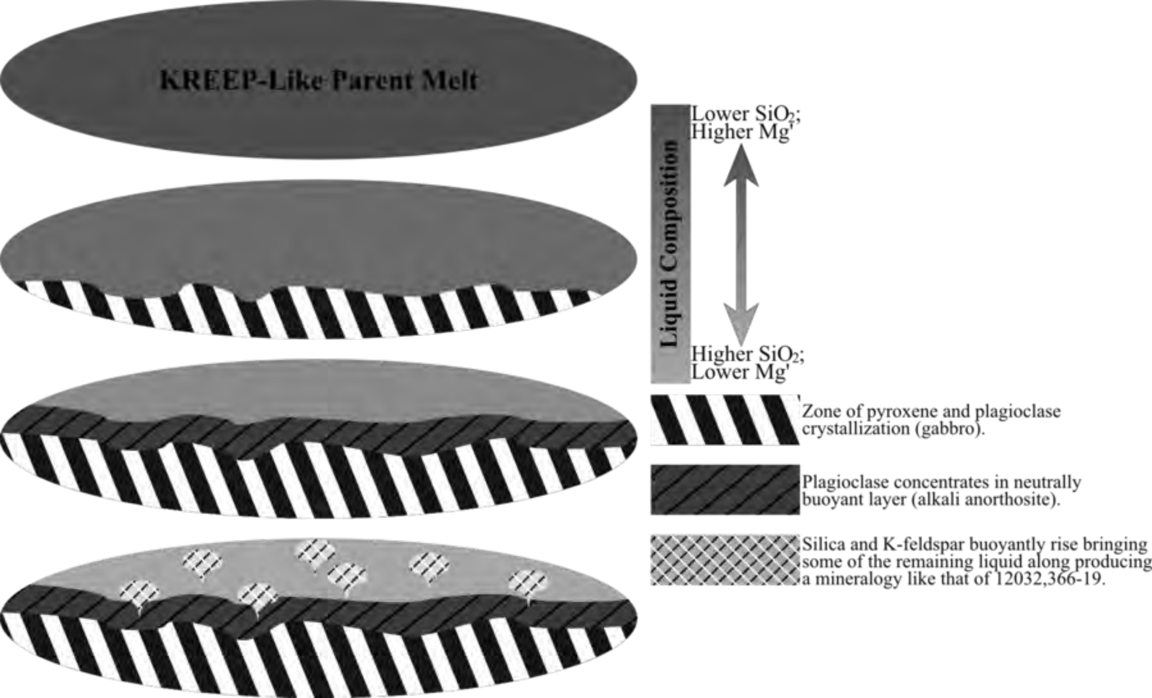
KREEP-Like Parent Melt
Liquid Composition
Lower SiO_2;
Higher Mg'
Higher SiO_2;
Lower Mg'
Zone of pyroxene and plagioclase crystallization (gabbro).
Plagioclase concentrates in neutrally buoyant layer (alkali anorthosite).
Silica and K-feldspar buoyantly rise bringing some of the remaining liquid along producing a mineralogy like that of 12032,366-19.

Table 1. The bulk composition of 12032,366-19.

	CMR	% Error	INAA	1σ		CMR	INAA	1σ
SiO$_2$	70.1	0.15	-	-	**Sm**	-	24.6	0.3
TiO$_2$	1.07	1.8	-	-	**Eu**	-	3.01	0.03
Al$_2$O$_3$	13.5	0.23	-	-	**Tb**	-	6.56	0.07
FeO	4.98	0.54	4.99	0.05	**Yb**	-	51.8	0.5
MnO	0.07	5.7	-	-	**Lu**	-	7.44	0.08
MgO	0.14	0.81	-	-	**Sc**	-	8.7	0.09
CaO	3.04	0.41	2.91	0.18	**Co**	-	0.77	0.02
BaO	0.68	1.1	0.68	0.01	**Ni**	-	<25	-
Na$_2$O	2.47	0.52	2.10	0.02	**Zn**	-	16	3
K$_2$O	4.58	0.21	4.80	0.24	**Rb**	-	96	2
P$_2$O$_5$	0.052	4.5	-	-	**Sr**	-	167	12
SUM	100.7	-	-	-	**Cs**	-	3.67	0.04
Cr	<200	-	11.3	0.6	**Ta**	-	10.4	0.1
Zr	1500	-	1500	20	**W**	-	9	1
Hf	37.8	-	45.5	0.5	**Ir**	-	<1.3	-
Nb	304	-	-	-	**Au**	-	<5	-
La	11.3	-	79.4	0.8	**Y**	457	-	-
Ce	106	-	182	2	**Th**	126	60.6	0.6
Nd	83.2	-	82	2	**U**	52.7	20.7	0.2

Oxide values are in wt%; element values are in ppm except Ir and Au which are in ppb. The INAA data are from Korotev et al. (2011); uncertainties (1σ) are 1 standard deviation estimates of analytical uncertainty based mainly on counting statistics. The "CMR" composition and "% Error" were derived by modal recombination using the average phase compositions from the microprobe (Table 2) to "best fit" the bulk rock INAA data (see text).

Table 2. Modal mineralogy of 12032,366-19.

		Abundance	
Phase	Composition	Image	CMR
K-feldspar	$An_{1.2-6.1}Ab_{25-33}Or_{58-74}Cn_{0.4-3.9}$	49	43.5
Quartz	$(Si,Al,Fe,Ti)O_2$	31	26
Plagioclase	$An_{35-48}Ab_{52-64}Or_{0.9-1.3}Cn_{0.0-0.1}$	6.2	19
Pyroxene	$En_{4.6-6.2}Fs_{51-52}Wo_{43-44}$	7.3	6.0
Olivine	$Fo_{2.7}Fa_{97}$	4.5	3.1
Ilmenite	$Il_{99.6}Gk_{0.4}$	1.8	1.7
Zirconolite	$(Fe,Y,Ca,REE)(Zr,Hf,U,Th)(Ti,Nb,Al,Si,Ta)_2O_7$	0.13	0.30
REE-rich apatite	$(Ca,REE,Y,Fe)_5([P,Si]O_4)_3(F,Cl)$	Trace	0.2
Apatite	$(Ca,Fe)_5(PO_4)_3(F,Cl)$	Trace	0.1
RE-merrillite	$(Ca,REE)_{16}(REE,Y)_2(Fe,Mg)_2([P,Si]O_4)_{14}$	Trace	0.08
ZrO_2	$Zr_{98.4}Hf_{1.6}$	0. 07	0.058
Sum		100	100

“Image” is the modal mineralogy of the 12032,366-19 polished section directly determined by image analysis. “CMR” was derived from a modal recombination using the average mineral compositions from the microprobe to “best fit” the bulk rock compositions from INAA (see text). All values are converted to weight percent. Zirconolite and phosphate formulae are idealized. Compositions are in Tables 3, 4a, and 4b. Cn = Celsian (Ba-feldspar end-member), Gk = Geikielite (Mg endmember of ilmenite solid-solution).

Table 3. Minerals in 12032,366-19.

	Kfs	Kfs*	Qz	Pl	Hd	Fa	Ilm	Apatite	RE-Ap	Merr	Glass Incl.	CMR
N	66	3	11	16	6	5	1	3	13	1	1	-
SiO_2	64.2	67.2	101.5	58.6	47.6	29.4	<0.03	2.01	3.17	0.90	78.3	70.0
TiO_2	0.063	0.04	<0.05	<0.04	0.92	0.13	51.1	n.a.	n.a.	n.a.	0.13	1.04
Al_2O_3	20.3	18.8	0.21	26.3	0.69	<0.02	<0.02	<0.02	0.05	<0.02	12.4	13.5
Cr_2O_3	<0.04	<0.04	<0.04	<0.04	<0.04	<0.04	<0.04	n.a.	n.a.	n.a.	<0.03	<0.02
FeO	0.12	0.46	0.21	0.21	29.3	68.6	47.4	0.90	1.79	5.24	1.10	4.99
MnO	<0.04	<0.04	<0.04	<0.04	0.34	0.83	0.43	<0.03	0.09	0.07	<0.04	0.12
MgO	<0.02	<0.02	<0.02	<0.02	1.65	1.06	0.12	<0.02	<0.02	0.59	<0.01	0.13
CaO	1.34	0.23	<0.10	8.56	19.2	0.17	<0.02	54.6	46.6	36.9	0.48	2.9
BaO	1.43	0.26	<0.06	<0.04	<0.05	<0.04	<0.05	n.a.	n.a.	n.a.	0.079	0.68
Na_2O	3.71	2.43	<0.04	6.57	0.10	<0.05	<0.05	0.10	0.17	0.07	0.86	2.10
K_2O	9.82	12.6	0.02	0.19	<0.01	<0.01	<0.01	n.a.	n.a.	n.a.	2.95	4.8
P_2O_5	<0.01	<0.01	<0.02	<0.01	<0.01	<0.01	<0.01	38.4	33.9	40.4	<0.01	0.039
Y_2O_3	n.a.	n.a.	n.a.	n.a.	n.a.	n.a.	n.a.	0.18	1.30	2.45	n.a.	n.a.
REE_2O_3	n.a.	n.a.	n.a.	n.a.	n.a.	n.a.	n.a.	1.13	7.21	12.6	n.a.	n.a.
F	n.a.	n.a.	n.a.	n.a.	n.a.	n.a.	n.a.	1.47	0.96	<0.02	n.a.	n.a.
Cl	n.a.	n.a.	n.a.	n.a.	n.a.	n.a.	n.a.	1.34	1.32	<0.01	n.a.	n.a.
-O=F	-	-	-	-	-	-	-	0.62	0.40	-	-	-
-O=Cl	-	-	-	-	-	-	-	0.34	0.30	-	-	-
Sum	101.0	102.0	102.4	100.6	99.8	100.1	100.2	99.3	95.9	99.2	96.4	100.0

Ilmenite also contains ~1 wt% Nb_2O_5, but V_2O_5 was below the detection limit; for oxide abundances in zirconolite, see Table 4a.

All values are reported in weight percent (wt%). *N* is the number of analyses averaged. “Kfs*” is a single analysis of a K-feldspar in an inclusion within a hedenbergite grain. “RE-Ap” refers to apatite analyses with high REE concentration. “Merr” refers to RE-merrillite. The “CMR” composition was derived by modal recombination using the average phase compositions from the microprobe (Table 2) to “best fit” the bulk rock INAA data (see text and Table 1). “n.a.” means “not analyzed.” REE_2O_3 was estimated from La, Ce, Nd, Gd, Y, and Yb included in the analyses (details in Experimental Procedures).

Table 4a. Zirconolite analyses containing the lowest concentrations of SiO_2 and those in which PbO was included.

Spot	Sum	ZrO_2	TiO_2	Y_2O_3	FeO	Nb_2O_5	CaO	ThO_2	UO_2	PbO	HfO_2	Ta_2O_5	Al_2O_3	SiO_2	MnO
1930	97.48	28.73	24.28	9.85	9.32	7.42	4.30	2.46	1.10	-	0.58	0.32	0.13	<0.01	0.09
1931	97.52	28.72	24.25	9.92	9.37	7.29	4.26	2.34	1.06	-	0.57	0.31	0.23	0.21	0.10
1936	98.74	30.21	24.05	9.73	8.84	7.81	4.70	1.45	0.50	-	0.81	0.29	0.11	0.31	0.11
1938	97.36	29.57	24.11	8.96	8.59	7.27	4.62	2.33	0.72	-	0.67	0.32	0.17	0.41	0.08
1943	94.55	21.43	17.43	6.67	6.65	5.07	3.18	1.39	0.37	0.60	0.63	0.24	0.13	21.08	0.06
1944	99.00	22.05	18.61	6.85	7.12	5.19	3.30	1.38	0.38	0.63	0.64	0.27	0.11	22.21	0.09
1945	91.95	23.81	19.15	7.18	7.27	5.65	3.61	1.71	0.43	0.74	0.62	0.22	0.12	11.05	0.07
1946	103.94	24.15	20.23	7.62	7.47	5.94	3.75	1.29	0.40	0.54	0.66	0.18	0.14	19.81	0.06
12013	89.7	17.2	22.1	9.1	11.6	8.3	3.0	4.1	3.4	-	-	-	-	2.1	-
Mare	100.28	30.61	28.51	9.05	9.70	3.91	3.18	0.11	0.05	-	0.60	0.24	0.41	0.08	0.00

Spot	La_2O_3	Ce_2O_3	Pr_2O_3*	Nd_2O_3	Sm_2O_3*	Gd_2O_3*	Tb_2O_3*	Dy_2O_3*	Ho_2O_3*	Er_2O_3*	Tm_2O_3*	Yb_2O_3	Lu_2O_3*
1930	0.23	1.59	0.19	1.38	0.52	0.81	0.16	1.16	0.28	0.98	0.17	1.22	0.21
1931	0.17	1.61	0.18	1.44	0.54	0.83	0.16	1.17	0.29	0.97	0.16	1.17	0.19
1936	0.30	2.26	0.23	1.58	0.58	0.86	0.17	1.18	0.28	0.93	0.15	1.11	0.18
1938	0.24	2.28	0.21	1.60	0.57	0.83	0.16	1.11	0.26	0.88	0.15	1.09	0.18
1943	0.20	1.74	0.33	2.19	1.19	0.85	0.15	1.06	0.25	0.75	0.12	0.83	0.14
1944	0.24	1.83	0.35	2.30	1.24	0.88	0.16	1.10	0.26	0.79	0.13	0.88	0.15
1945	0.26	1.82	0.35	2.30	1.26	0.90	0.16	1.13	0.27	0.81	0.13	0.90	0.15
1946	0.32	2.42	0.45	2.88	1.49	1.04	0.18	1.23	0.28	0.82	0.13	0.85	0.13
12013	0.2	1.7	-	-	-	-	-	-	-	-	-	-	-
Mare	0.19	1.64	0.47	3.48	1.67	2.62	-	2.34	-	0.99	-	0.43	-

REE oxides with * are estimated concentrations based on the measured REE values (see text). All values are in wt%. “Mare” is an average of 12 analyses from 7 zirconolite grains in 10047,11, 10047,227 and 10047,230 (Rasmussen et al. 2008). “12013” is an average of two zirconolite analyses from granitic lunar breccia 12013 (Haines et al. 1971). The * does not apply to “Mare” or “12013.” “-” means “not reported.”

Table 4b. Zirconolite formula calculation.

A	Ca	0.3220	0.3179	0.3455	0.3441
	Fe	0.5449	0.5456	0.5065	0.4999
	Mn	0.0055	0.0059	0.0066	0.0048
	Sum	0.8724	0.8694	0.8587	0.8487
B	Y	0.3665	0.3676	0.3549	0.3316
	La	0.0059	0.0045	0.0077	0.0061
	Ce	0.0406	0.0411	0.0568	0.0580
	Pr*	0.0048	0.0045	0.0057	0.0054
	Nd	0.0345	0.0358	0.0388	0.0397
	Sm*	0.0126	0.0130	0.0137	0.0137
	Gd*	0.0187	0.0191	0.0195	0.0190
	Tb*	0.0037	0.0037	0.0038	0.0036
	Dy*	0.0260	0.0263	0.0261	0.0249
	Ho*	0.0063	0.0064	0.0062	0.0059
	Er*	0.0214	0.0211	0.0201	0.0192
	Tm*	0.0036	0.0035	0.0033	0.0032
	Yb	0.0261	0.0249	0.0231	0.0232
	Lu*	0.0043	0.0041	0.0037	0.0038
	Sum	0.5753	0.5757	0.5834	0.5573
C	Zr	0.9794	0.9753	1.0100	1.0029
	Hf	0.0116	0.0113	0.0158	0.0132
	U	0.0171	0.0164	0.0076	0.0111
	Th	0.0391	0.0370	0.0226	0.0369
	Sum	1.0473	1.0400	1.0560	1.0641
D	Ti	1.2761	1.2701	1.2399	1.2610
	Si	0.0000	0.0148	0.0214	0.0287
	Nb	0.2346	0.2295	0.2419	0.2285
	Ta	0.0062	0.0059	0.0054	0.0060
	Al	0.0104	0.0190	0.0088	0.0139
	Sum	1.5272	1.5393	1.5175	1.5380
M_{I}	A	0.8724	0.8694	0.8587	0.8487
	B	0.1276	0.1306	0.1413	0.1513
	Sum	1.0000	1.0000	1.0000	1.0000
M_{II}	C	0.5523	0.5549	0.5579	0.5939
	B	0.4477	0.4451	0.4421	0.4061
	Sum	1.0000	1.0000	1.0000	1.0000
M_{III}	D	1.5272	1.5393	1.5175	1.5380
	Zr	0.4272	0.4204	0.4521	0.4090
Sum	1.9544	1.9597	1.9696	1.9470	
M_{I}+M_{II}+M_{III}		**3.9544**	**3.9597**	**3.9696**	**3.9470**

Methodology follows that of Wark et al. (1973) for four selected analyses. Ideally, M_{I}, M_{II}, and M_{III} should sum to 4. Elements with a * are estimated concentrations based on the measured REE values (see text).

Table 5. KB and BAG, and silicic immiscible liquid compositions.

	KB[1]	**BAG**[2]	**SLI**[3]	**SLI**[4]	**SLI**[4]	**SLI**[5]	**SLI**[6]
SiO_2	52.8	52.5	73.3	71.8	79.7	68.42	72.18
TiO_2	2.14	3.58	0.8	0.7	0.6	1.55	0.60
Al_2O_3	15.2	12.9	12.1	10.2	10.6	8.1	13.38
Cr_2O_3	0.29	0.13	-	-	-	-	-
FeO	10.1	13.3	3.2	4.0	3.5	7.26	4.10
MnO	0.15	0.18	0.0	0.0	0.0	0.06	0.26
MgO	7.4	4.82	0.0	1.1	0.6	1.92	1.06
CaO	9.4	9.1	1.8	6.5	1.2	2.84	2.90
Na_2O	0.89	0.97	3.1	2.2	2.2	2.33	0.75
K_2O	0.65	0.68	3.3	3.5	1.6	2.84	1.40
P_2O_5	0.62	0.51	0.07	0.0	0.0	0.0	0.37
SUM	99.6	98.7	97.7	100.0	100.0	95.3	97.0

Units are wt%. [1]Compiled by Papike et al. 1998. [2]Zeigler et al. 2006. [3]Philpotts 1982. [4]Philpotts 1981. [5]Krasov and Clocchiatti 1979. [6]Ryabov 1989.

Table 6. Compositions and characteristics of residual liquids in KB and BAG fractional crystallization models.

Wt% Liquid	**KB**					**BAG**				
	100	**75.3**	**51.3**	**26.1**	**10.6**	**100**	**74.69**	**50.19**	**25.67**	**14.58**
SiO_2	53.0	54.3	54.5	53.0	57.6	53.2	53.4	52.2	53.5	55.1
TiO_2	2.2	2.7	4.0	3.2	0.4	3.6	4.7	4.4	2.1	0.5
Al_2O_3	15.3	13.9	12.9	12.5	14.6	13.1	12.1	11.7	12.1	13.4
Cr_2O_3	0.3	0.1	0.1	0.1	0.2	0.1	0.1	0.1	0.1	0.1
FeO	10.1	11.3	12.9	14.7	12.6	13.5	14.5	15.9	17.2	15.3
MgO	7.4	5.8	3.5	1.8	0.4	4.9	3.4	2.5	1.2	0.3
MnO	0.2	0.2	0.2	0.3	0.4	0.2	0.2	0.3	0.3	0.4
CaO	9.4	9.0	8.6	8.5	4.2	9.2	9.0	9.5	7.7	5.6
K_2O	0.7	0.8	1.2	2.2	5.0	0.7	0.9	1.3	2.3	3.9
Na_2O	0. 9	1.0	1.1	1.4	1.9	1.0	1.1	1.2	1.6	1.9
P_2O_5	0.6	0.8	1.2	2.3	2.5	0.5	0.7	1.0	1.9	3.4
T(°C)	1147	1122	1078	1047	915	1092	1077	1062	1036	1017
η_S	125	260	618	702	66700	285	412	365	864	2650
η_{B-W}	106	196	471	787	20100	279	420	511	1120	3530

Oxides and temperatures are calculated by the MAGFOX program (Longhi 1991). η_S and η_{B-W} are the dynamic viscosities calculated using the KWare Magma program (Ken Wohletz, Version 2.49.0126) by the methods of Shaw (1972) and Bottinga and Weill (1972), respectively.

Table 7. Bulk compositions of 12032,366-19, selected lunar granites, selected high SiO_2 immiscible liquids, and granitic compositions generated from gravity separation model.

	1	**2**	**3**	**4**	**5**	**6**	**7**	**8**	**9**	**10**	**11**
SiO_2	70.0	73.0	70.8	74.2	68.1	75.5	76.4	74.2	65.8	70.2	70.2
TiO_2	1.04	0.60	0.60	0.33	0.90	0.26	0.7	0.7	2.3	1.17	1.16
Al_2O_3	13.5	11.9	12.7	12.5	10.2	12.3	12.2	11.1	10.6	13.3	13.4
FeO	4.93	0.90	6.30	2.32	6.99	3.10	1.8	6.9	8.5	4.62	4.97
MnO	0.13	0.12	0.10	0.02	-	0.04	-	-	-	-	-
MgO	0.14	0.70	0.40	0.07	1.53	0.20	0.5	0.1	1.5	0.34	0.25
CaO	3.0	1.40	1.00	1.25	4.89	0.50	1.1	2.1	5.7	3.88	3.51
BaO	0.77	0.65	-	0.24	-	0.61	-	-	-	-	-
Na_2O	2.49	1.40	1.10	0.52	0.79	0.53	0.5	0.4	1.6	1.67	1.91
K_2O	4.5	6.80	7.40	8.60	3.39	7.55	6.1	4.2	4.3	4.76	4.58
P_2O_5	0.039	-	0.70	-	-	-	0.01	0.2	0.3	-	-
ZrO_2	0.203	0.15	-	0.09	-	-	-	-	-	-	-
Hf	41.9	24	-	13.9	-	16	-	-	-	-	-
Cr	56	1010	0	17	-	70	-	-	-	0	0
Y	494	-	-	-	-	-	-	-	-	-	-
Th	132	41	-	65	-	9.5	-	-	-	-	-
U	45	12.3	-	23.4	-	-	-	-	-	-	-
SUM	100.8	97.6	101.1	100.1	96.7	100.6	99.3	99.9	100.6	100.0	100.0

Oxide units are wt%. Element units are ppm. 1. 12032,366-19: This study – microprobe and modal recombination. 2. 12013,10 light: Hubbard et al. 1970, Schnetzler et al. 1970, Wakita and Schmitt 1970, and Quick et al. 1977. 3. 12070,102-5: Potash rhyolite, Marvin et al. 1971. 4. 14321,1027: Pristine granite clast, Warren et al. 1983c. 5. 15405,12: Granite fragments, Ryder 1976. 6. 73255,27,3: Felsite clast, Blanchard and Budahn 1979. 7. Average compositions of six immiscible granitic inclusions in sample 14310,5, Roedder and Weiblen 1972. 8. Experimentally-produced high SiO_2 liquid from the fractionation of sample 12038,105, Hess et al. 1975. 9. Experimentally-produced high SiO_2 liquid from the fractionation of a composition similar to 15405 KREEP basalt, Rutherford et al. 1976. 10 and 11 are modeled compositions of low-density minerals in equilibrium with the melts of KB and BAG, respectively, in the last stages of fractional crystallization.

Petrology and geochemistry of lunar granite 12032,366-19 and implications for lunar granite petrogenesis.

Stephen M. Seddio[1,*], Bradley L. Jolliff[1], Randy L. Korotev[1], and Ryan A. Zeigler[2]

[1]Department of Earth and Planetary Sciences and the McDonnell Center for Space Sciences, Washington University, St. Louis, MO 63130, U.S.A. [2]Johnson Space Center, Houston, TX 77058, U.S.A.

ABSTRACT

Apollo 12 sample 12032,366-19 is a 21.3-mg granite fragment that is distinct from any other lunar granite or felsite. It is composed of barian K-feldspar, quartz, sodic plagioclase, hedenbergite, fayalite, and ilmenite, with trace amounts of zirconolite, baddeleyite, apatite, and merrillite. The texture of 12032,366-19 is largely a micrographic intergrowth predominantly of K-feldspar and quartz and, to a lesser extent, plagioclase and quartz. Hedenbergite, fayalite, and ilmenite are present in minor but significant quantities—6.0, 3.1, and 1.7 wt% respectively—and are scattered throughout the feldspar-quartz intergrowths. Trace amounts of Zr-bearing phases are found including zirconolite (0.6 wt%) and baddeleyite (0.04 wt%). Incompatible trace-element concentrations are high in 12032,366-19, particularly the high-field-strength elements, e.g., Zr, Sm, and Th (1500, 25, and 61 μg/g, respectively). The chondrite-normalized, rare-earth-element concentrations form a "V-pattern" that is characteristic of other lunar granitic material. Modeling 12032,366-19 as a derivative from a KREEP-like parent melt,

---

[*] E-mail: sseddio@levee.wustl.edu

the composition and mineral assemblage can be obtained by extended fractional crystallization combined with separation of the low-density minerals plus trapped melt components prior to final solidification. However, this model cannot quantitatively account for the relatively sodic composition of the plagioclase (An_{34-50}) and requires that the starting melt has Na_2O of 1.2 – 1.4 wt%, which is higher than most KREEP compositions. Formation of this assemblage by silicate-liquid immiscibility is neither required nor indicated by petrogenetic modeling.

INTRODUCTION

There are about twenty known lunar granites (Appendix 1) including "large" individual samples (e.g., Apollo 12 sample 12013, 82 g) and clasts within breccias (e.g., 14321,1027, 1.8 g). Most lunar granites are fine-grained; sample 15405,12 is the coarsest with >1-mm mineral grains (Ryder 1976). Lunar granites characteristically contain intergrowths of K-feldspar and silica. Plagioclase is also common and may be intergrown with silica as well. Lunar granites are diverse in the presence, abundance, and compositions of pyroxene and olivine (fayalite), and contain no water-bearing minerals. Most lunar granites have been severely affected by meteorite impacts in that they have been partially melted or brecciated, have experienced shock metamorphism, or contain clasts of other lithologies as well as Fe-Ni metal from impactors. We describe here a small granite fragment, designated 12032,366-19, that we separated from an Apollo 12 regolith sample. This granitic rock fragment is petrographically, mineralogically, and compositionally distinct from any previously characterized lunar granite and is largely unaffected by processes associated with meteorite impacts, i.e., it is monomict and unbrecciated. It is, however, unquestionably lunar.

SAMPLES AND EXPERIMENTAL PROCEDURE

Sample 12032 is the 2–4 mm grain-size fraction of one of several regolith samples collected on the Apollo 12 mission. Subsample 366 consists of 41 lithic fragments allocated for the studies of Barra et al. (2006) and Korotev et al. (2011) along with 317 lithic fragments from other Apollo 12 regolith samples. The subject of this paper is the 19th fragment in the subset, designated 12032,366-19 (Fig. 1). We examined all 358 fragments under a binocular microscope and analyzed each one individually for concentrations of 26 chemical elements by INAA (instrumental neutron activation analysis; Korotev et al. 2011). Eight fragments were found to be granitic in composition, with 12032,366-19 being the largest at 21.3 mg. INAA results for 12032,366-19 are reported in Table 1. Results for 12001,912-02 (9.2 mg) and 12032,366-07 (15.7 mg) are reported in Barra et al. (2006). Compositional results for the other five fragments (2.7–7.5 mg) are reported in Appendix 1. (INAA data for all 366 fragments are presented in the electronic annex of Korotev et al. 2011.)

After INAA, which is effectively nondestructive, we mounted and polished the sample in a petrographic thick section for EPMA (electron-probe microanalysis). The texture and mineral assemblage were characterized by high-resolution BSE (back-scattered electron) imaging and X-ray map analysis using the 5-wavelength-spectrometer JEOL 8200 electron microprobe at Washington University, which includes a high-intensity LIFH/PETH H-type spectrometer and an EDS (energy-dispersive spectrometer) with an SDD (silicon-drift detector). Images and maps were generated at an accelerating voltage of 15 kV and a beam current of 25 nA (50 nA for X-ray maps), except as indicated below. We used a combination of WDS (wavelength-dispersive spectrometers) and the SDD EDS to generate X-ray maps.

Quantitative mineral compositions were determined by WDS EPMA using the Probe for EPMA software developed by Probe Software, Inc. In addition, we used the Probe for EPMA software for data correction including peak interference corrections (e.g., Th mβ on U mα; and Fe $L\alpha_1$ on F Kα). Nominal analytical conditions for typical mineral phases (feldspar, silica, pyroxene, fayalite, ilmenite, and glass) were 15 kV accelerating voltage and 25 nA beam current, with beam diameters ranging from 1 to 10 µm. Analytical standards included synthetic and natural silicate, oxide, and REE glass standards of Drake and Weill (1972) and Carpenter et al. (2002) for primary calibration, and these were checked against secondary standards.

Typically, elements were measured using the Kα lines and counted on peak for 40 seconds (Si, Ti, Al, Cr, Fe, Mn, Mg, Na), except for elements analyzed using the high-intensity spectrometer (Ca, K, and P were counted for 20 seconds, and Ba, using the Lα line, was counted for 120 seconds). In addition to these elements, analyses of Zr-rich minerals included an expanded element list as follows: V (20 seconds); Zr (60 seconds); La, Ce, Nd, and Yb (120 seconds each); Hf, Ta, and Pb (180 seconds each); Y and Nb (220 seconds each); and U and Th (240 seconds each). This protocol led to detection limits for most minor and trace elements in the 0.01 to 0.04 wt% range (100 to 400 µg/g).

When analyzing phosphates, elements measured using the Kα lines were counted on peak for 20 seconds (Ca), 25 seconds (Na), 30 seconds (Mn, Fe), 35 seconds (Al), 40 seconds (Mg, Si, and P), 45 seconds (Cl), and 130 seconds (F); elements measured using the Lα lines were counted on peak for 30 seconds (La, Ce, Gd, Nd, and Yb) and 45 seconds (Y). We used the Probe for EPMA software to correct for the interference of Fe $L\alpha_1$ and Ce $M\zeta$ on F $K\alpha$ and to apply a non-linear (polynomial) background correction for F (and Si). The F X-ray count-rates, which were analyzed on a layered-dispersive element (LDE1) crystal, were found to vary with positive linear time dependence (Fig. 2; Stormer et al. 1993). Such variations were accounted for by the time-dependent intensity correction of the Probe for EPMA software, which we used to project the F X-ray count-rates back to time zero using a linear extrapolation to determine the intensity (e.g., McCubbin et al. 2010). In our analyses of the REEs, we applied the following the interference corrections using the Probe for EPMA software: Nd Ll on La $L\alpha_1$; La $L\gamma_3$, Ce $L\gamma_1$, and Nd $L\beta_2$ on Gd $L\alpha_1$; and Ce $L\beta_1$ on Nd $L\alpha_1$.

We used a modal recombination technique that we designate Model 1 (Tables 1 and 2) to estimate the bulk concentration of elements for which concentration data were not obtained by INAA. The model was constrained to fit the oxides for which both microprobe and INAA concentrations were obtained (FeO, CaO, BaO, Na_2O, K_2O, and ZrO_2). Phase abundances (Table 2) were determined using image analysis of a BSE mosaic and X-ray maps to essentially count all pixels in each phase, which were then divided by the total number of pixels (background subtracted) to obtain the volume fraction. The volume fraction of each phase was multiplied by the density of each respective phase (Deer et al. 1976). Finally, we divided these individual values by their sum to yield weight fractions. The bulk concentrations of each oxide were then calculated by summing the oxide concentration of each phase (an average of the phase compositions determined by electron microprobe) multiplied by the weight fraction of the phase (see example for SiO_2 below).

$$[\mathrm{SiO_2}]_{\mathrm{Bulk}} = \sum_{\text{phase } n=1,2,3\ldots} \left([\mathrm{SiO_2}]_n \mathrm{X}(\text{weight fraction of phase n})\right)$$

The bulk composition obtained from INAA represents the entire 21.3 mg sample, but the concentrations generated from the modal recombination technique represent only the specific plane of the section exposed by the polished mount and the BSE image and X-ray maps of that section. To assure that our bulk major-element composition was representative of the whole sample, we adjusted phase proportions from those obtained from image analysis to best-fit the INAA data. For example, our polished section of 12032,366-19 contains 6.2% plagioclase and 7.3% hedenbergite (area percentages converted to weight percentages) leading to a bulk CaO concentration of 2.2 wt% for 12032,366-19 (based on the average compositions of plagioclase and hedenbergite). INAA, however, yields a bulk CaO of 2.9 ± 0.2 wt%. In Model 1, we increase the plagioclase abundance to 19 wt%, and decrease the hedenbergite abundance to 6.0 wt% (to fit both the INAA derived bulk CaO of 2.9 ± 0.2 wt% and FeO of 4.99 ± 0.05 wt%). The Model 1 bulk CaO therefore is 3.04 wt%. This example is simplified since Model 1 takes the CaO contribution of all present phases into account, not just plagioclase and hedenbergite.

The Model 1 error was calculated using the error from both EPMA and image analysis. We applied counting statistics to the total number of pixels attributed to each phase in the image and X-ray maps (Fig. 3,4). The final "% Error" values are the result of propagating error through averaging the phase compositions, multiplying the average compositions by the wt% of that phase, and summing those values for each oxide or element. The trace-element compositions listed in the "EPMA" composition are from zirconolite, baddeleyite, REE-rich apatite, RE-merrillite, and apatite. These phases account for very small portions of the image, and their abundances were constrained to fit the INAA data as closely as possible. Following the same procedures for error propagation as with the major elements, the errors in the model associated with the trace elements would be between 260 and 640%.

One irregular zirconolite grain (see descriptions in next section) yielded initial compositional analyses containing anomalously high SiO_2. To further investigate this composition, assuming that the zirconolite grain thickness might be such that the analyzed composition resulted from overlap of the electron interaction volume with another mineral, we obtained three BSE images of the area at 5, 15, and 25 kV accelerating voltages (Fig. 5). We then modeled electron trajectories by Monte Carlo simulations using the Casino program version 2.42 (Hovington et al. 1997). Simulations of 5000 electron trajectories each were run at 5, 15, and 25 kV on models consisting of K-feldspar overlying zirconolite and zirconolite overlying quartz. The thickness of the top layer was varied. We constrained the thickness by noting whether or not the backscattered electrons interacted only with the top phase at the different accelerating voltages.

Following the method of Montel et al. (1996), we calculated the crystallization age of 12032,366-19 from our analyses of zirconolite. In doing so, we assumed that all Pb analyzed is radiogenic which is valid since Pb should not exist in thorite beyond trace concentrations. Given that assumption,

$$\mathrm{Pb} = \frac{\mathrm{Th}}{232}\left(e^{\lambda^{232}t}-1\right)208 + 0.9928\frac{\mathrm{U}}{238.04}\left(e^{\lambda^{238}t}-1\right)206 + 0.0072\frac{\mathrm{U}}{238.04}\left(e^{\lambda^{235}t}-1\right)207$$

where Pb, Th, and U are in ppm and $\lambda^{232}, \lambda^{235}$, and λ^{238} are the decay constants for Th^{232}, U^{235}, and U^{238}, respectively. Solving for *t* yields the age of the analyzed grain along with the fraction of lead generated from each parent element.

We identified the silica phase as the polymorph quartz by Raman spectroscopic analysis using a Hololab 5000-532 laser Raman spectrometer (Kaiser Optical Systems, Inc.). The 532 nm line of a frequency-doubled Nd:YAG solid-state laser was used as the excitation source. Analyses were done using a 20× long-working distance objective (NA=0.4), which condenses the laser beam into a spot of 6 µm diameter on the sample, with an average power of 11 mW. This objective also collects the back-scattered Raman photons from the sample. These photons were sent through a multimode optical fiber to a Raman spectrograph. A volume holographic grating spectrometer disperses the collected Raman photons into a Raman Stokes shift range of 100 to 4300 cm^{-1} relative to the 532-nm laser line, with a spectral resolution of 4–5 cm^{-1}. See Freeman et al. (2008) for more analytical details.

RESULTS

Petrography

Lunar sample 12032,366-19 is an unshocked, unbrecciated, fine-grained granitic rock fragment. It is composed predominantly of granophyric intergrowths of barian K-feldspar ($An_{0.7-16}$,Ab_{21-50},Or_{33-78},$Cn_{0.4-3.9}$) and quartz (Figs. 3,4) that, according to modal analysis, account for ~62 wt% of the sample, and to a lesser extent, a graphic intergrowths of plagioclase (An_{34-50},Ab_{49-65},$Or_{0.8-6.6}$,$Cn_{0.0-0.3}$) and quartz (Table 2, Figs. 3,4) that account for ~27 wt% of the sample. K-feldspar and silica intergrowths extend throughout the entire sample, whereas intergrowths of plagioclase and silica occur on the scale of ~1 mm. The mafic phases are present in significant amounts (6.0 wt% hedenbergite and 3.1 wt% fayalite) compared to most other lunar granites (e.g., 12013 Light; 12033,507; 14161,7269; 14303,204; 14321,1027; 15405,12; and 73255,27,3; see Appendix 1 for references) in which it is common for either pyroxene or olivine (or both) to be absent. There are >20 hedenbergite grains and >30 fayalite grains exposed in our polished section of 12032,366-19.

Potassium feldspar. Compositions of K-feldspar (Fig. 6; Table 3) are similar, from spot to spot and as reflected in the K X-ray image, with two exceptions. (1) In several instances, large subhedral grains (as large as 440 × 100 μm) of K-feldspar lack quartz intergrowths (Figs. 3,4) and are zoned. The cores of these grains have a higher Na/K than their rims, which have Na/K similar to the rest of the K-feldspar in the sample (Fig. 4). (2) The K-feldspar ("Kfs*" of Table 3) that is part of a subrounded inclusion inside one of the three "large" (see below) pyroxene grains has among the lowest Na/K in the fragment. Moreover, in K-feldspar in the inclusion, the abundance of the Cn (celsian, Ba-Feldspar) component is only 0.5%, whereas the other analyzed K-feldspar compositions have Cn values of 1.6 to 3.9% (0.91 to 1.90 wt% BaO). The "Kfs*" analyses also have the highest FeO content (0.44 to 0.49 wt%) of the analyzed K-feldspar grains but not by a large amount (the other analyses range from <0.05 to 0.34 wt%). It is unlikely that the high FeO of these analyses results from beam overlap with the surrounding hedenbergite grain because these analyses also have some of the highest K_2O (11.0 to 13.5 wt%) in the sample.

The granophyric intergrowths of quartz and K-feldspar occur in the following three textures in decreasing order of abundance: parallel (Fig. 7d), irregular (lower left, Fig. 7a), and graphic (Upper half, Fig. 7b; left of center, Fig. 7c). The parallel granophyre consists of homogeneously thin (average width: 6 μm), parallel grains of quartz intergrown with K-feldspar. The quartz grains in the irregular granophyre are commonly wider (average width: 8 μm) than those in the parallel. The quartz grains of the graphic texture are the widest (8-12 μm) of the three granophyric textures and intersect each other. The three textures continuously extend from K-feldspar into plagioclase (Figs. 3,4).

Plagioclase. Plagioclase is not zoned and is unusually sodic for a lunar rock ($An_{33.5-50.2}$, Fig. 6). In fact, the albite contents of the plagioclase are the highest of which we are aware in any lunar sample. This high albite content is not totally unprecedented though: Warren et al. (1987) reported zoned plagioclase with rims of $An_{35.5}$ in felsite 12033,507. The FeO content of the plagioclase ranges from 0.14 to 0.33 wt% with an average concentration of 0.21 wt %. These values are consistent with FeO concentrations reported for plagioclase in other lunar granites (e.g. Warren et al. 1987; Jolliff 1991).

Quartz. The SiO_2 phase is identified as quartz on the basis of Raman spectroscopy (Fig. 8). Its texture is fractured in a hackled pattern, suggesting that it may have inverted from cristobalite. Quartz analyses with the electron microprobe give minor-oxide concentrations (Table 3), including Al_2O_3 (0.21 wt%), FeO (0.21), TiO_2 (0.05), CaO (<0.06), BaO (<0.06), and K_2O (0.02 wt%).

Hedenbergite. All analyzed pyroxene grains in 12032,366-19 are hedenbergite ($En_{4.6-6.2}$, Fs_{51-52}, Wo_{43-44}). In the probe mount, there are three relatively large grains: an elongate grain (670 × 56 μm; Figs. 3,4,7a) that terminates at the edge of the sample, a 196 × 134 μm grain with a sub-rounded inclusion (diameter = 58 μm; Figs. 3,4), and a 425 × 112 μm grain (Figs. 3,4). There are >20 other, smaller grains of hedenbergite in the section. The pyroxene grains are subhedral with irregular boundaries and in some cases are serrated. Six spot analyses of hedenbergite yielded minor concentrations of TiO_2 (0.69-1.28 wt%), Al_2O_3 (0.53-0.84 wt%), MnO (0.33-0.38 wt%), and Na_2O (0.07-0.14 wt%) which are common concentrations for pyroxenes in other lunar granites (Quick et al. 1977; Warren et al. 1987; Jolliff 1991). Careful examination of the 12032,366-19 Mg X-ray map indicates that the larger pyroxene grains are slightly richer in Mg (up to 2 wt% MgO) at the cores.

Fayalite. In 12032,366-19, the fayalite ($Fa_{97.3}$) grains are small (average grain size: 130 × 50 μm), and subhedral to anhedral with generally equant morphologies. The fayalite contains ~1 wt% MgO and small amounts of MnO (0.79-0.86 wt%), CaO (0.11-0.24 wt%), TiO_2 (<0.05-0.19 wt%), and P_2O_5 (0.06-0.07 wt%). These concentrations are typical of olivine compositions in other lunar granites (Quick et al. 1977; Warren et al. 1987).

Ilmenite. Ilmenite grains tend to be elongate (aspect ratio average: 13.5, range: 5.9 to 27; Fig. 7b,7c) but not to the extent of some of the zirconolite grains (see below). Ilmenite is commonly found along the boundaries of pyroxene and olivine, though where it occurs as such, it tends to be subhedral to anhedral. Ilmenite and baddeleyite are the only minerals in the sample that exhibit a preference for occurring adjacent to another mineral. Ilmenite grains contain only 0.12 wt% MgO, lower than the MgO range observed in the ilmenite of 12013 felsic material (1.76-2.01 wt%, Quick et al. 1981). The

Nb_2O_5 concentration is 0.97 wt%, whereas V_2O_5 is below the detection limit (<0.017 wt%). Both of these concentrations are similar to those of ilmenite in the granitic phase of 12013 (Quick et al. 1981).

Baddeleyite. In 12032,366-19, the baddeleyite phase is always found in association with ilmenite, and its analyses reveal concentrations of HfO_2 of 2.8 wt% and measureable FeO (1.1 wt%), TiO_2 (0.8 wt%), and Nb_2O_5 (0.5 wt%). The largest ZrO_2 grain is euhedral, 24.7 x 16.8 µm, and is highlighted in Figure 7a.

Zirconolite. Zirconolite occurs in two forms in 12032,366-19. The first consists of fine-grained, elongate "strings" (finely elongate green phase in Fig. 4b; diagonal, bright phase in Fig. 7b; and gray arrow in Fig. 7c) scattered throughout the section. These elongate grains are typically ~65 µm long and ~3 µm wide. There is only one occurrence of the second form in the studied slice of 12032,366-19. It is coarser (0.1 mm long, 0.04 mm wide) than any occurrence of the elongate form and has an irregular shape (green at top of Fig. 4b, false-colored X-ray image).

Zirconolite is a fairly common accessory mineral in evolved lunar rocks that has the general formula $(Ca,REE)_1Zr_1(Ti,Nb,Ta)_2O_7$. In 12032,366-19, its composition (Table 4) is similar to compositions reported by Wark et al. (1973) and Rasmussen et al. (2008) in some lunar mare basalts and breccias (Table 4); however, the composition obtained by Haines et al. (1971) for zirconolite in the 12013 granitic breccia has 12.8 wt% less ZrO_2 than that in 12032,366-19. Several of our zirconolite analyses on elongate grains imply significant concentrations of SiO_2; however, we conclude that these results are an artifact of electron beam volume overlap because the zirconolite grains are so thin. Figure 9 shows that concentrations of other elements correlate inversely with the SiO_2

concentration, implying that SiO_2 from other minerals effectively 'dilutes' the other oxides as opposed to Si replacing cations in the zirconolite crystal. If Si were replacing one or a few cations, we would expect the concentrations of the substituted cations to decrease as Si increases while the concentrations of the cations Si does not replace should remain constant as Si increases. In the largest zirconolite grain in the probe mount, an irregularly-shaped occurrence (Fig. 4b,5), initial analyses yielded as much as 22.2 wt% SiO_2. We addressed this issue as described in the analytical section; here we further discuss the mineral chemical trends because it is important to establish the chemical composition of this occurrence of zirconolite. Suspecting the high SiO_2 might be an analytical issue, we imaged (BSE) the grain using different accelerating voltages and then modeled the thickness (using the Casino program version 2.42; Hovington et al. 1997) to be only 70-250 nm. Other portions of the irregular occurrence are overlain by K-feldspar (Fig. 5) modeled to be only 120-220 nm thick. All analyses on the thin or overlain portions of this zirconolite grain also contain a compositional component from the overlying and underlying phases. We conclude that the SiO_2, Al_2O_3, and Na_2O components of our zirconolite analyses were contributed by electron beam interaction with nearby (vertically distributed) phases, specifically quartz, plagioclase, and K-feldspar. Our best analysis indicates that the zirconolite contains <0.008 wt% SiO_2.

We measured concentrations of the four REEs present in the highest concentrations (La, Ce, Nd, and Yb) and Y in our zirconolite analyses (Fig. 10), but many of the analyses resulted in low totals. The REE^{3+} concentrations of the zirconolite analyses with the lowest SiO_2 concentrations were interpolated to form a smooth, chondrite-normalized pattern with the measured REE concentrations (Fig. 10). We also assume that the Y concentration, normalized to chondrites, plots at a point halfway between normalized Ho and Er concentrations (Korotev, 1996). The full REE component was then used to calculate the structural formula of the 12032,366-19 zirconolite (Table 4b). The normalized REE pattern is HREE-rich (Fig. 10) unlike the pattern of REE in the mare basalt occurrence reported by Rasmussen et al. (2008). Oxide sums, including the REE, for the four analyses with lowest silica range from 97.4% to 98.7% (Table 4a).

Zirconolite analyses were normalized on the basis of 7 oxygen atoms using the structural formula, $(\mathbf{M_{I}})^{2+}(\mathbf{M_{II}})^{4+}(\mathbf{M_{III}})_{2}^{4+}\mathbf{O_{7}}$, following the methods of Wark et al. (1973) as described in the experimental procedure section. The results are listed in Table 4b. Four zirconolite analyses included PbO data (Table 4a). Using Th, U, and Pb concentrations, we calculated a crystallization age of 3.87 ± 0.28 Ga.

Phosphates. Phosphates are rare in 12032,366-19 and account for <0.3 vol% of 12032,366-19, on the basis of image analysis of a P X-ray map of the sample. Quantitative analyses reveal that three phosphate phases are present in 12032,366-19—apatite, REE-rich apatite, and RE-merrillite—all of which are anhedral to subhedral and likely took on the shape of the small pockets of residual melt where they occur. Of the apatite grains we have measured, the compositions fall into a high-REE group (we refer to these compositions as “REE-rich apatite”) and a low-REE group (we refer to these compositions as “apatite”); they do not form a continuum of REE concentrations. Because the phosphate grain sizes are small, commonly <5 μm, we disregarded analyses that indicate overlap of the electron beam interaction volume with an adjacent phase (e.g., ~1 wt% Al_2O_3 from feldspar or ~5 wt% SiO_2 from quartz). We measured concentrations of five REEs (La, Ce, Nd, Gd, and Yb) and Y in our phosphate analyses (Fig. 10). La, Ce, Nd, and Y were above detection limits in analyses of all three phosphates; Gd and Yb are above detection limits in merrillite with 15-22% and 23-32% error, respectively, and are above detection limits in about half of the REE-rich apatite analyses with 24-52% and 25-47% error, respectively. The (low REE) apatite analyses have Gd and Yb below detection limits. On a chondrite-normalized plot (Fig. 10), the analyzed LREE form a negative slope that is the same for the three phosphates. In merrillite, the analyzed HREEs have a roughly flat slope. We used these slopes to interpolate the unanalyzed REE^{3+} concentrations. Though Gd and Yb were commonly below detection limits in the apatites, Y (and Gd and Yb when detectable) indicates that the apatite and REE-rich apatite have LREE and HREE chondrite-normalized patterns that mimic the pattern of merrillite. We interpolated the concentrations of REE^{3+} in apatite that were either not analyzed or that were found to be below our detection limits using the chondrite-normalized REE pattern of merrillite scaled to the concentrations detected for the LREE and Y.

The largest grain of apatite in 12032,366-19 is 25 × 15 μm and is adjacent to an elongate zirconolite grain and quartz. In apatite, the (F, Cl, OH) site is occupied by 0.30-0.56 F and 0.17-0.23 Cl apfu (atoms per formula unit), and sums range from 0.47 to 0.78 leaving open the possibility for a missing component, possibly OH (McCubbin et al. 2010). The apatite analyses contain 1.91-2.09 wt% SiO_2 (0.16 to 0.18 apfu) which is more than enough to provide a charge balance for the 1.25-1.36 wt% $(REE,Y)_2O_3$ (0.04-0.05 apfu). We suspect that the excess SiO_2 was contributed to the analyses by secondary fluorescence of Si in adjacent quartz.

The REE-rich apatite ("RE-Ap" in Table 3, Fig. 2) contains 7.21 average wt% REE_2O_3. The largest occurrence of REE-rich apatite is elongate, 44 × 6 μm (Fig. 7d), but it has been fractured into segments typically with dimensions of ~5 μm or less. It contains 3.17 average wt% SiO_2, which corresponds to 0.29 apfu per 25 negative charges and provides charge-balance for the REEs and Y (0.31 apfu). F and Cl are also present at 0.96 ± 0.11 and 1.32 ± 0.06 wt% (0.28 and 0.21 apfu), respectively (errors are one σ) which, based on apatite stoichiometry, only occupies 41.7-53.8% of the (F, Cl, OH) site, leaving open the possibility that this grain contains significant OH.

RE-merrillite is the third phosphate present in 12032,366-19. Concentrations of F and Cl are below detection limits (<0.02 and <0.01 wt%, respectively). Only on grain was large enough (15 × 5 μm) to provide a good analysis, and it contains 5.24 wt% FeO, 0.59 wt% MgO, and 15.1 wt% $(REE+Y)_2O_3$. The chondrite-normalized REE pattern (Fig. 10) shows that the RE-merrillite is LREE-rich. On the basis of our electron microprobe analyses, the REE-rich apatite has a similar chondrite-normalized REE pattern to that of the RE-merrillite but is about an order of magnitude lower in concentration.

Glass Inclusions. We observed inclusions of glass and two crystalline inclusions in pyroxene in 12032,366-19. The inclusions are more or less rounded and located at or near the center of the pyroxene grains. All of the inclusions are glass except for the largest (diameter of 58 μm), which has crystallized to an assemblage of K-feldspar, plagioclase, and quartz, and another, which has crystallized into K-feldspar and quartz. One of the largest glass inclusions has a composition with significantly higher SiO_2 than the bulk sample (e.g., 78.3 vs. 70.1 wt% SiO_2, Table 3). The bulk composition of the largest crystalline inclusion contains 70.6 wt% SiO_2. The inclusion's composition was calculated using a modal recombination technique that assumed the inclusion-hedenbergite boundary was originally smooth, like all other inclusion-hedenbergite boundaries in the section, until the inclusion crystallized additional hedenbergite onto the boundary. The hedenbergite within the assumed boundary is included in the modal recombination.

Bulk composition

The bulk composition of 12032,366-19, as estimated from Model 1 (constrained modal recombination), and the composition obtained by INAA are listed in Table 1. The phase abundances derived from both the image analysis and the modal recombination are listed in Table 2. Notable major oxide concentrations obtained from INAA include: 4.99 wt% FeO (Fig. 11), 2.10 wt% Na_2O, and 4.8 wt% K_2O (Table 1). Only four reported lunar granitic compositions have lower bulk FeO (12023,147-10; 14321,1027; 73215,43,3; 73255,27,2; Appendix 1). Samples 14321,1027 (149 mg); 73215,43,3 (20 mg); and 73255,27,3 (2 mg) are granitic clasts and have the lowest bulk FeO (2.3, 3.0, and 3.1 wt%, respectively; references are in Appendix 1). Sample 12023,147-10 (2.67 mg) is an igneous fragment with no evidence of brecciation. It contains 3.1 wt% FeO. Clast 14303,204 (70 mg) has a bulk FeO concentration of 5.6 wt% (Warren et al. 1983c), which is the most similar to that of 12032,366-19. Sample 15434,10 (27 mg), which has an igneous texture, has the highest bulk FeO (19 wt%) of any sample identified as lunar granite (identified as such from thin section 15434,10,136; Ryder and Martinez 1991)—likely a sampling issue from the coarseness of the texture compared to the size of the 39 mg chip analyzed by INAA (Ryder and Martinez 1991). The remaining eighteen samples listed in Appendix 1 have bulk compositions that range from 6.0 to 14 wt% FeO and have been identified as granitic lunar samples. High bulk FeO is likely a result of other lithologies being mixed with granitic lithologies during the formation of granitic breccias.

The bulk Na_2O (2.10 wt%) of 12032,366-19 is the highest of any lunar sample of which we are aware. The second most sodic lunar granitic composition is that of breccia 14001,28.4 (1.90 wt%, Morris et al. 1990), and others have bulk Na_2O as low as 0.19 wt% (breccia 73215,43,3).

Compared to high-K KREEP (Warren 1989), Ba, Rb, Cs, Yb, Lu, Ta, W, Th, and U concentrations are high in 12032,366-19 (Fig. 12), whereas the LREE are lower by a factor of ~0.6. Iridium and Au are below INAA detection limits (<1.3 ppb and <5 ppb, respectively), consistent with an unbrecciated rock unaffected by meteoritic contamination. REE abundances and relative concentrations are unlike typical Apollo 12 mare and nonmare materials, including KREEP, but are similar to other granites and felsites, exhibiting a characteristically V-shaped chondrite-normalized REE pattern (e.g., Blanchard and Budahn 1979; Jolliff 1991; Fig. 13). In 12032,366-19, the LREE-rich RE-merrillite and REE-rich apatite and the HREE-rich zirconolite (Fig. 10) are the most likely main contributors to the V-shaped chondrite-normalized REE pattern.

DISCUSSION

Granites are one of the rarest lithologies in the Apollo collection, implying that rocks of granitic composition make up only a small fraction of the lunar crust. However, granitic samples are relatively common among the nonmare components at Apollo 12 (five have been characterized thus far) compared to the other Apollo sites presumably because the site is located in the Procellarum KREEP Terrane, which has the highest abundances of K, Th, and U on the lunar surface (Lawrence et al. 1998). Given the high concentrations of those elements in granite, it logically follows that the source of most of the lunar granitic material would be in this terrane as well. The Apollo 14 and Apollo 15 sites also lie within this terrane, and both have yielded several granitic samples (Ryder 1976; Warren et al. 1983c; Jolliff 1991; Ryder and Martinez 1991) whereas we are aware of no granite clasts in the Apollo 16 collection. Moreover, silicic surface compositions associated with some of the “red spots” such as the Gruithuisen domes, Mairan domes, and Hansteen Alpha (Hawke et al. 2003; Wilson and Head 2003; Glotch et al. 2010), most of which are now known to be silica-rich (Glotch et al. 2010), occur within this terrane.

12032,366-19 compared to other lunar granites

Granite 12032,366-19 is of lunar origin. It contains no petrographic indication of hydrous alteration of any minerals (e.g., serpentinization of fayalite, sericitization of plagioclase). Micas and amphiboles are absent in 12032,366-19 (and other lunar samples) but are common in terrestrial granites.

Sample 12032,366-19 is unique among lunar samples. It contains no impact-generated glass or brecciated material, unlike many other lunar granites (Rutherford et al. 1976; Warren et al. 1983c; Morris et al. 1990; Jolliff 1991). The graphic intergrowth of K-feldspar and silica, commonly expressed as a granophyre, dominates most of the lunar granitic samples (e.g., 12013); however, significant amounts of plagioclase-silica intergrowths are far less common among reported samples. It is also common for lunar granites to contain shock-melted glass, but 12032,366-19 contains none. It is noteworthy that only a quarter or so of known lunar granites have any pyroxene in abundances large enough to analyze, and the Mg’ of the pyroxene in 12032,366-19, essentially endmember hedenbergite, is significantly lower than those of other lunar granites (Fig. 14).

Perhaps because all samples are exceedingly small by terrestrial sampling and analysis standards, a wide distribution in bulk compositions characterizes rocks (and assemblages) that have been classified as lunar granites or felsites. Appendix 1 includes several granitic bulk compositions for comparison with 12032,366-19. The 12032,366-19 REE concentrations are most similar (of those to which it has been compared thus far) to those of 12001,912-02; 12013,10,28; 12023,147-10; and 12033,517, all from Apollo 12. 12032,366-19 contains the second highest concentration of BaO (0.68 wt%) of which we are aware in a lunar sample (the highest is in sample 12032,366-07, another lithic fragment of granitic composition) and a substantial amount of Zr-bearing minerals. The most striking difference between 12032,366-19 and the other lunar granites is that its Na_2O/K_2O is higher by a factor of 2-5 than that of the others—a characteristic reflected by both the abundance and sodic nature of its plagioclase. To our knowledge, the texture and mineral assemblage of this sample is unique among studied lunar samples.

Lunar granites (pristine or otherwise) have U-Pb crystallization ages between 3.88 and 4.32 Ga (from zircon analyses; Meyer et al. 1996). Our calculation of a crystallization age of 3.87 ± 0.28 Ga for sample 12032,366-19 is consistent with the young end of that range.

Pristinity

Although 12032,366-19 was collected on the immediate surface of the Moon, it contains no evidence of any admixed meteoritic or regolith material. The bulk rock concentration of Ir is low, <1.3 ppb, corresponding to <0.2% meteoritic material (H chondrite equivalent). Moreover, metallic iron and troilite are absent. Metallic Fe, depending on Ni concentrations, would also indicate a meteoritic source (Papike et al.

1991). There are no spherules present in the sample, and there is no regolith adhering to the edge of the sample (Fig. 1) indicating that no regolith has been incorporated into 12032,366-19, which, if present, would have been obvious in the siderophile element concentrations.

Shock-melted glass is a common occurrence in many lunar granitic samples (e.g., 14303,204 is a felsite clast of which half is glass; Warren et al. 1983c). It is also common for veins of impact glass to cut through portions of granitic samples (e.g., 12033,507; Warren et al. 1987). The only glass in 12032,366-19 occurs as inclusions in hedenbergite and does not appear to be of shock-melted origin. These glass inclusions are more likely to be melt that became trapped within an early forming crystal. The granitic composition of the inclusion glass indicates that the hedenbergite was in equilibrium with the granite melt. The texture indicates that 12032,366-19 only experienced one episode of crystallization and has not experienced any re-melting since.

ZrO_2 – SiO_2 phase boundary

In sample 12032,366-19, baddeleyite (monoclinic) is in textural contact with quartz (Fig. 7a). The ZrO_2–SiO_2 phase diagram generated by Kaiser et al. 2008 indicates that ZrO_2 (tetragonal) and SiO_2 (cristobalite) are only stable together between 1673 and 1687°C. At lower temperatures, the phases should react to form zircon. We are unaware of another instance of zirconia and silica coexisting adjacent to one another. The presence of the other minerals or the chemical composition of the melt itself may have made the coexistence of baddeleyite and silica thermodynamically favorable. Alternatively, baddeleyite and silica may not have crystallized in thermodynamic equilibrium. The granophyric intergrowth of K-feldspar and quartz and plagioclase and quartz suggests that crystallization was rapid. In that case, the kinetics of crystallization may have allowed baddeleyite and silica to coexist outside of thermodynamic equilibrium. This particular occurrence warrants further investigation.

Petrogenesis

The following three methods of producing granitic compositions in the low-fO_2, low-pressure conditions near the lunar surface have been suggested: (1) high SiO_2 achieved by fractional crystallization of an evolved parent such as KREEP basalt or basaltic andesite glass (e.g., Longhi 1990); (2) high SiO_2 achieved by SLI (silicate liquid immiscibility; e.g., Hess et al. 1975; Rutherford et al. 1976; Neal and Taylor 1989; Jolliff 1991); and (3) partial melting of an enriched crustal protolith (e.g., KREEP basalt) by basaltic underplating (e.g., Lawrence et al. 2005; Hagerty et al. 2006). SLI tends to form very high SiO_2, low CaO and low FeO compositions (Table 5), so we do not favor it. (2) and (3) are both plausible based on terrestrial analogs, but are difficult to distinguish. Process (3), coupled with upward enrichment of high-silica melt is a very common process on Earth, leading to the formation of bimodal volcanics, i.e., basalt and rhyolite. We see this situation perhaps reflected in 12013. In the same vein, we do not see intermediate compositions (with SiO_2 between 52 and 70 wt%) when there should be more of the intermediate silica materials than high silica if (2) were the main process. We explore the methods of producing lunar granitic material, considering their ability to produce lithologies like 12032,366-19.

12032,366-19 contains K-feldspar, quartz, alkali-rich plagioclase, Fe-pyroxene, and Fe-olivine—a complete mineral assemblage consistent with late-stage fractional crystallization. These phases have relatively low melting temperatures compared to Mg-pyroxenes and Mg-olivine, and indicate of crystallization from a liquid that had already exhausted most of its Mg and was therefore in the extreme late stages of fractionation. The incompatible trace elements in 12032,366-19 are high compared to KREEP (Fig. 12). The concentrations of these elements in the liquid become higher as crystallization continues, and it logically follows that 12032,366-19 crystallized from a liquid that was at a late stage of fractional crystallization in order to explain such high concentrations of incompatible elements. This indication of the late-stage nature of the parent melt is complemented by the near absence of phosphates. Phosphorus is an incompatible element, and phosphates tend to crystallize late in the fractional crystallization process (Hess and Rutherford 1974, Hess et al. 1975, Warren et al. 1983c, Jolliff 1991, and Jolliff et al. 1999). Since phosphate in 12032,366-19 is present at only a trace level, the parent melt must have crystallized phosphates as part of a residual assemblage that was presumably segregated and left behind during gravity separation of the granitic mass, as hypothesized by Jolliff (1991). Separation of minerals that concentrated the middle REE (merrillite and apatite) explains the V-shaped REE pattern as a result of early phosphate crystallization, which would impart a middle REE depletion relative to the LREE and HREE on remaining residual melt.

Petrogenetic modeling

Because the texture of 12032,366-19 shows no direct (relict) evidence of liquid immiscibility—except, perhaps, the glass inclusions with ~78 wt% SiO_2 within hedenbergite (see below)—such as that seen in sample 14161,373, a mafic assemblage containing rounded segregations of K-feldspar and SiO_2 (Jolliff 1991, Jolliff et al. 1999), we tested whether the bulk composition could be achieved simply by fractional crystallization of a melt with a KREEP-like composition. We selected KREEP basalt (KB) 15434,18,199-A (composition compiled by Papike et al. 1998) and basaltic andesite glass (BAG) of Zeigler et al. (2006) as compositions to represent potential parent melts because both compositions (Table 5) represent alkali-rich melts that could plausibly have fractionally crystallized to produce felsic final assemblages. Compared to the KB composition, the BAG composition has higher Fe/Mg (2.8 vs. 1.4) and lower Al_2O_3 (12.9 vs. 15.2 wt%), but the SiO_2 contents are similar(BAG: 52.5 wt%; KB: 52.8 wt%). The compositions were modeled using MAGFOX (Longhi 1991) as resulting from extended fractional crystallization reaching 89.4 wt% crystallized (for KB) and 85.4 wt% crystallized (for BAG). The paths that the compositions of the residual liquids for KB and BAG follow are shown in Figs. 15 and 16. The compositions, temperatures, and viscosities of the residual liquids at ~25 wt% crystallization intervals are given in Table 6.

For the fractional crystallization of the KB melt, SiO_2 increases from ~53 to 55.4 wt% at 44 wt% crystallization when quartz begins to crystallize and then decreases back to 53 wt% at 71 wt% crystallization. Then SiO_2 increases to 57.5 wt% at 89.4 wt% crystallized. K_2O increases to 5 wt% at 89.4 wt% crystallization. Initially, Al_2O_3 decreases from ~16 to 12 wt% at 69 wt% crystallization and then increases to 14.6 wt%. FeO increases from 10 to 12 wt% until quartz begins to crystallize at 44 wt% crystallization, after which FeO increases more markedly, reaching a maximum of 15.3 wt% at 79 wt% crystallized. From there, FeO decreases to 12.6 wt% owing to crystallization of fayalitic olivine, ferropyroxene (Fo_{12} and $En_{10}Wo_{47}$, respectively), and ilmenite. P_2O_5 increases from 0.6 wt% to 3.5 wt% at 83 wt% crystallization. At that point, whitlockite (merrillite) begins to crystallize and drives the P_2O_5 down to 2.9 wt%. The KB residual liquid is closest to the field of immiscibility (Roedder 1951) at 44 wt% crystallization (Figs. 15, 16).

For the fractional crystallization of the BAG melt, SiO_2 initially increases slightly to 54 wt% at 21 wt% crystallization and then decreases to ~52 wt% at 49 wt% crystallization owing to the crystallization of quartz. SiO_2 then finally increases to 55 wt%. K_2O increases from 0.7 wt% to around 4% at 85.4 wt% crystallized. Plagioclase ($An_{86}Ab_{13}$) forms early and keeps Al_2O_3 relatively constant at around 13.2 wt%. FeO increases to 17.4 wt% at ~69 wt% crystallized, at which point fayalitic olivine saturates. The FeO increase is relatively gradual—a result of the saturation of pigeonite, ilmenite, and ferroaugite. The co-crystallization of fayalitic olivine, pigeonite, ferroaugite, and ilmenite drive FeO to a concentration of 15.3 wt% in the residual melt. The P_2O_5 concentration increases from 0.52 wt% to 3.4 wt% at 85.4 wt% crystallization without a phosphate saturating. The BAG residual liquid is enters the field of immiscibility (Roedder 1951) at 16.2 wt% crystallization (Figs. 15, 16).

Both the KB and BAG crystallization models have several shortcomings. Neither KB nor BAG produce, upon fractional crystallization, residual melt compositions as rich in SiO_2 (57.5 wt% and 55.1 wt%, respectively; Figs. 15 and 16) as observed in the granite (70.1 wt%)%), at least not at a stage when there is enough liquid left for plausible separation of melt from crystals. Low oxygen fugacity relevant to the lunar system prevents crystallization of magnetite, which in terrestrial liquid compositions occurs early and halts the FeO-enrichment trend, and causes the SiO_2 concentration of residual melt to increase to produce rhyolitic liquid compositions (e.g., Hess et al., 1975). Under lunar

fO_2 and low water content, FeO-rich residual melts would typically reach the field of silicate-liquid immiscibility prior to onset of Fe-Ti oxide crystallization. Both models drive TiO_2 to very low levels by the 80-85% solidification stage, yet in 12032,366-19, ilmenite is present and the bulk TiO_2 is 1.07 wt%. FeO concentrations in the model residual melts at this point are 12.3 wt% (KB) and 15.3 wt% (BAG), which is roughly three times that of 12032,366-19 (4.98 wt%). K_2O in 12032,366-19 (4.58 wt%) is similar to that predicted by the models (5.0 wt%, KB and 3.9 wt%, BAG). KB and BAG produce P_2O_5 of 2.9 wt% (KB) and 3.4 wt% (BAG) while that of 12032,366-19 is only 0.052 wt%. Also, the anorthite contents of KB ($An_{62.6}$) and BAG ($An_{62.5}$) are higher than that of 12032,366-19 ($An_{34.9}$). Most importantly, K-feldspar does not saturate in either the KB or BAG models. The crystallizing mineral assemblages at the 80-85% solidification stage of the KB and BAG models would be tonalitic based on QAPF classification (Fig. 15); however, if the normative K-feldspar from the residual liquid is included in the classification, the mineral assemblage for both models is that of quartz monzonite

Silicate liquid immiscibility

As noted above, a the key failure of extended fractional crystallization is that it does not generate SiO_2 concentrations in residual melts as high as observed in the granite (~70 wt%) while there is still a significant proportion of residual melt. Moreover the process of extended fractional crystallization should produce intermediate evolved compositions in greater volumes than granite, yet such compositions are not observed. In fact, evolved lunar rock compositions generally have bimodal distributions with respect to silica content (Hess et al. 1975; Rutherford et al. 1976). Also, the absence of intermediate lunar lithologies, something akin to terrestrial granodiorite (or dacite), which would be produced as a melt progressed from crystallizing mafic rocks to felsic rocks implies that another process may have occurred (Rutherford et al. 1976).

Silicate liquid immiscibility has long been suggested as a process responsible for the production of lunar granites while at the same time accounting for the absence of intermediate lithologies (e.g., Hess et al. 1975; Rutherford et al. 1976; Neal and Taylor 1989; Jolliff 1991). SLI is a process that can occur as a melt undergoes fractional crystallization. As crystallization proceeds and melt becomes progressively richer in Si, Fe, and incompatible elements, the melt can ultimately reach a composition that unmixes when the melt enters the field of SLI (Fig. 16). This process has been observed in the laboratory (Hess et al. 1975, Rutherford et al. 1976) and in nature (e.g., Skaergaard, Jakobsen et al. 2005; Bushveld, Lee 1979). One of the liquids is Fe-rich and incorporates the REE- and P-rich fraction of KREEP, which, if it separates physically from the felsic fraction, crystallizes as monzogabbro or monzodiorite. The complementary liquid is rich in Si and K, and if it separates physically from the Fe-rich liquid, would crystallize to a felsic or granitic assemblage (Rutherford et al. 1976; Taylor et al. 1980; Jolliff 1991; Table 5).

SLI could feasibly be combined with the fractional crystallization model to explain the bulk composition of 12032,366-19 in the following way: a parent melt of composition similar to BAG or KB undergoes extensive fractional crystallization until it reaches a point where SLI occurs (Fig. 16). As the melt unmixes into two liquids, the denser, Fe-rich liquid remains with the crystallizing (gabbroic) assemblage, and the lower-density felsic liquid rises and separates from the gabbroic fraction. Finally, the granitic liquid continues to crystallize producing the bulk composition of 12032,366-19.

However, in our models, as the KB composition crystallizes, it does not pass into the field of SLI, and BAG only grazes the boundary of the field before trending away from it (Fig. 16). This leads us to search for other possibilities to explain the petrogenesis of 12032,366-19.

Although SLI has been observed to occur on a small (micro) scale in lunar rocks, including mare basalts (Roedder and Weiblen 1970; Roedder and Weiblen 1971; Roedder and Weiblen 1972) and monzogabbro (Jolliff 1991), it is not clear that SLI could or did occur on a scale large enough to produce some of the large silicic volcanic constructs on the Moon such as the Gruithuisen domes, the Mairan domes, and Hansteen Alpha (Glotch et al. 2010). Partial melting produced by basaltic "underplating" has been suggested as an alternative process that could produce significant amounts of granitic material (Lawrence et al. 2005; Hagerty et al. 2006). This process involves the injection of basaltic magma into the lunar crust and partial melting of the overlying crustal material, which then intrudes to a shallow level, forming granite, or extrudes onto the surface as a large volume of rhyolitic material without producing intermediate lithologies. The efficacy of this process depends on the composition of the crust at the point of intrusion of basaltic melt and on the rheology and transport of the silica-rich material upward from the zone where it is formed. If the crust was anorthositic, it is unlikely that basaltic underplating would lead to a significant amount of melting because of the high melting point of anorthosite. If, however, basaltic melt intruded into a crust of KREEP-basalt or similar composition, which has a melting point around 1000º C, and if the crust in this region was already hot, then partial melting would have been much more likely and more volumetrically significant.

The glass inclusions with ~78 wt% SiO_2 within hedenbergite could be explained as a product of local SLI. A liquid with the composition of the glass inclusion combined with a relatively small amount of hedenbergite and a liquid with the composition of hedenbergite combined with the glass inclusion would be complementary liquids consistent with the miscibility gap of Roedder (1951). However, The glass inclusion composition could also be the result of the crystallization of hedenbergite from an inclusion with the bulk composition of 12032,366-19 onto the inner walls of the host hedenbergite grain. A third explanation appeals to the vagaries of late stage fractional crystallization.

Gravity separation of phases

If we take the mineral compositions that are in equilibrium with the KREEP basalt and BAG residual melts at the latest stages of crystallization as modeled above and adjust the proportions by increasing the low-density phases relative to the high-density phases, as might occur during gravity separation or flow differentiation, we can achieve the compositions of the pristine granites without appealing to SLI (Fig. 17; Columns 10 and 11, Table 7). For this gravity separation model, we add the K-feldspar from calculating the normative mineralogy of the residual liquid at the final stages of the KB and BAG models to the mineral assemblages predicted by the KB and BAG models. To obtain the pristine granite compositions, the concentrations of K-feldspar and quartz modeled above must increase by factors of 1.3 to 1.5 and 4.0 to 4.2, respectively. An exception for 12032,366-19 is its high Na_2O, which requires a more sodic plagioclase and an additional 0.3-0.5 wt% Na_2O content in either the KB or BAG starting melt composition in order for the crystallizing plagioclase to have ~$An_{33.5}$ to match that contained in the sample.

The obvious problem for this model is how to separate phases after a high degree of crystallization and at relatively high silica contents when the viscosity of the system is very high. The viscosities of the KB and BAG models, calculated using the KWare Magma program (Ken Wohletz, Version 2.49.0126) and the methods of Shaw (1972) and Bottinga and Weil (1972), become as high as ~67000 and ~3500 Pa·s, respectively. Separation of phases is also a problem in the case of the two liquids produced by SLI because the Si-rich phase similarly has a very high viscosity. Separation of the mafic and felsic phases in the lunar magmatic environment was not assisted by tectonic forces and processes involving significant concentrations of magmatic water as it is in terrestrial environments. The high-viscosity, silica-rich phase does not need to flow, it simply needs to rise through the much lower-viscosity mafic residual melt. Perhaps movements related to large impacts that occurred during the time of upper-crustal magmatism played a role in the segregation of these phases, for example, movement along faults or uplifts associated with basin ring formation, or movement related to isostatic adjustments following an impact and associated flow segregation.

Equilibrium crystallization and SLI

Compositions derived from crystallization modeling done using the MAGPOX program (Longhi 1991) plotted on the phase diagram of Roedder (1951) indicate that a liquid with the initial composition of KB is driven into the field of SLI after 56 wt% of crystallization in equilibrium with the crystallizing solids. Granitic compositions could be produced from the crystallization of a liquid of KB composition if the first 50% of crystallization occurred in equilibrium with the solids. If the immiscible liquids were physically separated, then the silicic liquid would solidify to produce a rock with ~70 wt% bulk SiO_2 (terrestrial examples include the silicic immiscible liquid compositions in Table 5).

IMPLICATIONS

Remote sensing data, Earth-based (near-IR reflectance spectra) and orbital (images from Clementine and LRO; spectra from Lunar Prospector gamma-ray spectrometer and LRO Diviner radiometer), have provided evidence for regions of silicic volcanism on the Moon. Sample 12032,366-19 (an igneous rock rich with K-feldspar, quartz, and plagioclase, along with near Fe end-member mafic minerals) is a candidate to be among the lunar samples most similar to the rocks that compose some of the lunar "red spots." Glotch et al. (2010) identified several of the red spots as regions of high-SiO_2 content from the Christiansen Feature in the LRO Diviner data. Perhaps the 12032,366-19 mineralogy is relevant to interpreting some of the features seen at the silicic volcanic complex that lies at the center of the Compton/Belkovich Th-anomaly (Jolliff et al. 2011), which has been modeled to have a Th concentration of 40-55 ppm (Lawrence et al. 2003). This concentration is similar to that for the bulk sample of 12032,366-19 (60.6 ppm) as well as other lunar granites (Appendix 1).

ACKNOWLEDGEMENTS

We thank Paul Carpenter for his assistance with trace element analysis on the electron microprobe and insight into Zr-Ti phases. We also thank Alian Wang and Weigang Kong for Raman spectroscopic measurements. This work was funded by NASA grant NNG04GG10G (RLK).

References Cited

Anders E. and Grevesse N. (1989) Abundances of the elements: meteoritic and solar. Geochimica et Cosmochimica Acta, 53, 197-214.

Barra, F., Swindle, T.D., Korotev, R.L., Jolliff, B.L., Zeigler, R.A., and Olson, E. (2006) ^{40}Ar-^{39}Ar dating on Apollo 12 regolith: Implications on the age of Copernicus and the source of non-mare materials. Geochimica et Cosmochimica Acta, 70, 6016–6031.

Blanchard, D.P., J.W. Jacobs, and J.C. Brannon (1977) Chemistry of ANT-suite and felsite clasts from the consortium breccia 73215 and of gabbroic anorthosite 79215. Procedings of the 8th Lunar and Planetary Science Conference, 2507-2524.

Blanchard, D.P. and J.R. Budahn (1979) Remnants from the ancient lunar crust: clasts from consortium breccia 73255. Procedings of the 10th Lunar and Planetary Science Conference, 803-816.

Bottinga, Y.A. and Weil, D.F. (1972) The viscosity of magmatic silicate liquids: a model for calculation. American Journal of Science, 272, 438-473.

Brown, G.M., Emeleus, C.H., Holland, J.G., and Phillips, R. (1970) Mineralogical, Chemical and petrological features of Apollo 11 rocks and their relationship to igneous processes. Proceedings of the Apollo 11 Lunar Science Conference, 195–219.

Carpenter, P., Counce, D., Kluk, E., and Nabelek, C. (2002) Characterization of Corning EPMA Standard Glasses 95IRV, 95IRW, and 95IRX. Journal of Research of the National Institute of Standards and Technology, 107, 703-718.

Deer, W.A., Howie, R.A., and Zussman, J. (1976) An Introduction to the Rock Forming Minerals. Longman Group Limited, London.

Dence, M.R., Douglas, J.A.V., Plant, A.G., and Traill, R.J. (1970) Petrology, mineralogy and deformation of Apollo 11 samples. Proceedings of the Apollo 11 Lunar Science Conference, 315–340.

Drake, M.J., and Weill, D.F. (1972) New rare earth element standards for electron microprobe analysis, Chemical Geology, 10, 179-181.

Freeman, J.J., Wang,A., Kuebler, K.E, Haskin, L.A. (2008) Characterization of natural feldspar by Raman spectroscopy for future planetary exploration. Canadian Mineralogist, 46, 1477–1500.

Glotch, T.D., Lucey, P.G., Bandfield, J.L., Greenhagen, B.T., Thomas, I.R., Elphic, R.C., Bowles, N., Wyatt, M.B., Allen, C.C., Hanna, K.D., Paige, D.A. (2010) Highly silicic compositions on the Moon. Science, 329, 1510.

Haines, E.L., Albee, A.L., Chodos, A.A., and Wasserburg, G.J. (1971) Uranium-bearing minerals of lunar rock 12013. Earth and Planetary Science Letters, 12, 145-154.

Hagerty, J.J., Lawrence, D.J., Hawke, B.R., Vaniman, D.T., Elphic, R.C., and Feldman, W.C. (2006) Refined thorium abundances for lunar red spots: Implications for evolved, nonmare volcanism on the Moon. Journal of Geophysical Research, 111, E06002.

Hawke, B.R., Lawrence, D.J., Blewett, D.T., Lucey, P.G., Smith, G.A., Spudis, P.D., and Taylor, G.J. (2003), Hansteen Alpha: A volcanic construct in the lunar highlands, Journal of Geophysical Research, 108, 5069.

Hess, P.C. and Rutherford, M.J. (1974) Element fractionation between immiscible melts. Abstracts of the Lunar and Planetary Science Conference, 5, 328-330.

Hess, P.C., Rutherford, M.J., Guillemette, R.N., Ryerson, F.J., and Tuchfeld, H.A. (1975) Residual products of fractional crystallization of lunar magmas - an experimental study. Proceedings of the 6th Lunar Science Conference, 895-909.

Hovington, P., Drouin, D., and Gauvin, R. (1997) CASINO: A new Monte Carlo code in C language for electron beam interaction—Part I: Description of the program. Scanning,19, 1-14.

Hubbard, N.J., P.W. Gast, and H. Wiesmann (1970) Rare earth alkaline and alkali metal and 87/86 Sr data for sub-samples of lunar sample 12013. Earth and Planetary Science Letters, 9, 181-184.

Jakobsen, J.K., Veksler, I.V., Tegner, C., and Brooks, C.K. (2005) Immiscible iron- and silica-rich melts in basalt petrogenesis documented in the Skaergaard intrusion. Geology, 33, 885-888.

Jarosewich, E., Nelen, J.A., and Norberg, J.A. (1980) Reference samples for electron microprobe analysis. Geostandards Newsletter, 4, 43–47.

Jolliff, B.L. (1991) Fragments of quartz monzodiorite and felsite in Apollo 14 soil particles. Proceedings of the 21st Lunar and Planetary Science Conference, 101–118.

Jolliff, B.L., Floss, C., McCallum, I.S., and Schwartz, J.M. (1999) Geochemistry, petrology, and cooling history of 14161, 7373: A plutonic lunar sample with textural evidence of granitic-fraction separation by silicate-liquid immiscibility. American Mineralogist, 84, 821-837.

Jolliff, B.L., Korotev, R.L., and Haskin, L.A. (1991) Geochemistry of 2-4-mm particles from Apollo 14 soil (14161) and implications regarding igneous components and soil-forming processes. Proceedings of the 21st Lunar and Planetary Science Conference, 193–219.

Jolliff, B.L., Wiseman, S.A., Lawrence, S.J., Tran, T.N., Robinson, M.S., Sato, H., Hawke, B.R., Scholten, F., Oberst, J., Hiesinger, H., van der Bogert, C.H., Greenhagen, B.T., Glotch, T.D., and Paige, D.A. (2011) Non-mare silicic volcanism on the lunar farside at Compton-Belkovich. Nature Geoscience, 4, 566-571.

Kaiser, A., Lobert, M., and Telle, R. (2008) Thermal stability of zircon ($ZrSiO_4$). Journal of the European Ceramic Society, 28, 2199-2211.

Keil, K. and Prinz, M. (1971) Mineralogy and composition of Apollo 11 lunar samples. Proceedings of the Second Lunar Science Conference, 319-341.

Keil, K., Bunch, T.E., and Prinz, M. (1970) Mineralogy and composition of Apollo 11 lunar samples. Proceedings of the Apollo 11 Lunar Science Conference, 561–598.

Korotev, R.L. (1996) A self-consistent compilation of elemental concentration data for 93 geochemical reference samples. Geostandards Newsletter, 20, 217–245.

Korotev, R.L., Jolliff, B.L., Zeigler, R.A., Seddio, S.M., and Haskin, L.A. (2011) Apollo 12 revisited. Geochimica et Cosmochimica Acta, 75, 1540-1573.

Krasov, N.F. and Clocchiatti, R. (1979). Immiscibility in silicate melts and its possible petrogenetic importance, as shown by study of melt inclusions. Transactions (Doklady) of the USSR Academy of Sciences, 248, 92-95.

Lawrence, D.J., Hawke, B.R., Hagerty, J.J., Elphic, R.C., Feldman, W.C., Prettyman, T.H., and Vaniman, D.T. (2005) Evidence for a high-Th, evolved lithology on the Moon at Hansteen Alpha. Geophysical Research Letters, 32, L07201.

Lawrence, D.J., Feldman, W.C., Barraclough, B.L., Binder, A.B., Elphic, R.C., Maurice, S., and Thomsen, D.R. (1998) Global elemental maps of the moon: The Lunar Prospector Gamma-Ray Spectrometer. Science, 281, 1484.

Laul, J.C. (1986) Chemistry of the Apollo 12 highland component. Proceedings of the 16th Lunar and Planetary Science Conference, D251–D261.

Lee, C.A. (1979) Spheroidal pyroxenite aggregates in the Bushveld Complex — a special case of silicate liquid immiscibility. Earth and Planetary Science Letters, 44, 295-310.

Longhi, J. (1990) Silicate liquid immiscibility in isothermal crystallization experiments. Proceedings of the 20th Lunar and Planetary Science Conference, 13-24.

Longhi, J. (1991) Comparative liquidus equilibria of hypersthene-normative basalts at low pressure. American Mineralogist, 76, 785-800.

Marvin, U.B., Wood, J. A., Taylor, G. J., Reid Jr., J. B., Powell, B. N., Dickey Jr., J. S., and Bower, J. F. (1971) Relative proportions and probable sources of rock fragments in the Apollo 12 soil samples. Proceedings of the Second Lunar Science Conference, 679-699.

McCubbin, F.M., Steele, A., Nekvasil, H., Schnieders, A., Rose, T., Fries, M., Carpenter, P.K., and Jolliff, B.L. (2010) Detection of structurally bound hydroxyl in fluorapatite from Apollo Mare basalt 15058,128 using TOF-SIMS. American Mineralogist, 95, 1141-1150.

Meyer, C., Williams, I.S., and Compston, W. (1996) Uranium-lead ages for lunar zircons: Evidence for a prolonged period of granophyre formation from 4.32 to 3.88 Ga. Meteoritics and Planetary Science, 21, 370-387.

Montel, J.-M., Foret, S., Veschambre, M., Nicollet, C., and Provost, A. (1996) Chemical Geology., 131, 37-53.

Morgan, J.W. and Ehman, W.D. (1970) Lunar rock 12013; O, Si, Al and Fe abundances. Earth and Planetary Science Letters, 9, 164.

Morris, R.W., Taylor, G.J., Newsom, H.E., and Keil, K. (1990) Highly evolved and ultramafic lithologies from Apollo 14 soils. Proceedings of the 20th Lunar and Planetary Science Conference, 61–75.

Neal, C.R., and Taylor, L.A. (1989), The nature of barium partitioning between immiscible melts: A comparison of experimental and natural systems with reference to lunar granite petrogenesis. Proceedings of the 19th Lunar and Planetary Science Conference, 19th, 209.

Papike, J.J., Ryder, G., and Shearer, C.K. (1998) Lunar samples. Planetary Materials, Reviews in Mineralogy, 36, 5-1.

Papike, J.J., Taylor, L., and Simon, S. (1991) Lunar minerals. The Lunar Sourcebook, Cambridge University Press, 121-181.

Philpotts, A.R. (1981). Liquid immiscibility in silicate melt inclusions in plagioclase phenocrysts. Bulletin de Mine¤ralogie, 104, 317-324.

Philpotts, A.R. (1982). Compositions of immiscible liquids in volcanic rocks. Contributions to Mineralogy and Petrology, 80, 201-218.

Quick, J.E., Albee, A.L., Ma, M.-S., Murali, A.V., and Schmitt, R.A. (1977) Chemical compositions and possible immiscibility of two silicate melts in 12013. Procedings of the 8th Lunar and Planetary Science Conference, 2153-2189.

Quick, J.E., James, O.B., and Albee, A.L. (1981) Petrology and petrogenesis of lunar breccia 12013. Proceedings of the 12th Lunar and Planetary Science Conference, 117-172

Rasmussen, B., Fletcher, I.R., and Muhling, J.R. (2008) Pb/Pb geochronology, petrography and chemistry of Zr-rich accessory minerals (zirconolite, tranquillityite and baddeleyite) in mare basalt 10047. Geochimica et Cosmochimica Acta, 72, 5799-5818.

Roedder, E. (1951) Low temperature liquid immiscibility in the system K_2O-FeO-Al_2O_3-SiO_2. American Mineralogist, 36, 282-286. Proceedings of the 3rd Lunar Science Conference, 251-279.

Roedder, E. and Weiblen, P.W. (1970) Lunar pertrology of silicate melt inclusions, Apollo 11 rocks. Proceedings of the Apollo 11 Lunar Science Conference, 801-837.

Roedder, E. and Weiblen, P.W. (1971) Petrology of silicate melt inclusions, Apollo 11 and Apollo 12 and terrestrial equivalents. Proceedings of the Second Lunar Science Conference, 801-837.

Roedder, E. and Weiblen, P.W. (1972) Petrographic features and petrologic significance of melt inclusions in Apollo 14 and 15 rocks. Proceedings of the Third Lunar Science Conference, 801-837.

Rutherford, M.J., Hess, P.C., Ryerson, F.J., Campbell, H.W., and Dick, P.A. (1976) The chemistry, origin and petrogenetic implications of lunar granite and monzonite. Proceedings of the 7th Lunar Science Conference, 1723-1740.

Ryabov, V.V. (1989). Liquation in Natural Glasses: the Example of Traps. Novosibirsk: Nauka.

Ryder, G. (1976) Lunar sample 15405: remnant of a KREEP basalt-granite differentiated pluton. Earth and Planetary Science Letters, 29, 255-268.

Ryder, G. and Martinez, R.R. (1991) Evolved hypabyssal rocks from Station 7, Apennine Front, Apollo 15. Proceedings of the 21st Lunar and Planetary Science Conference, 137-150.

Schnetzler, C.C., J.A. Philpotts, and M.L. Bottino (1970) Li, K, Rb, Sr, Ba and rare-earth concentrations, and Rb-Sr age of lunar rock 12013. Earth and Planetary Science Letters, 9, 185-192.

Seddio, S.M., Korotev, R.L., Jolliff, B.L., and Zeigler, R.A. (2009) Petrographic diversity in Apollo 12 regolith rock particles**.** Lunar and Planetary Science Conference XL. Lunar and Planetary Institute, Houston. #2415 (abstract).

Shaw, H.R. (1972) Viscosities of magmatic silicate liquids: an empirical method of prediction. American Journal of Science, 272, 870-893.

Snyder, G.A., Taylor, L.T., Liu, Y-.G., and Schmitt, R.A. (1992) Petrogenesis of the western highlands of the moon - Evidence from a diverse group of whitlockite-rich rocks from the Fra Mauro formation. Proceedings of Lunar and Planetary Science, 22, 399-416.

Stormer, J.C., Pierson, M.L., and Tacker, R.C., (1993) Variation of F-X-ray and Cl-X-ray intensity due to anisotropic diffusion in apatite during electron-microprobe analysis. American Mineralogist, 78, 641-648.

Taylor, G.J., Warner, R.D., Keil, K., Ma, M.-S., and Schmitt, R.A. (1980) Silicate liquid immiscibility, evolved lunar rocks and the formation of KREEP. Proceedings of the Conference of the Lunar Highlands Crust, 339-352.

Wakita, H. and Schmitt, R.A. (1970) Elemental abundances in seven fragments from lunar rock 12013. Earth and Planetary Science Letters, 9, 169-176.

Wark, D.A, Reid, A.F., Lovering, J.F., and El Goresy, A. (1973) Zirconolite (versus zirkelite) in lunar rocks. Abstracts of the Lunar and Planetary Science Conference, 4, 764 (abstract).

Warren, P.H. (1989) KREEP: major-element diversity, trace-element uniformity (almost). Workshop on Moon in Transition: Apollo 14, KREEP, and Evolved Lunar Rocks, 149-153 (abstract).

Warren, P.H., Jerde, E.A., and Kallemeyn, G.W. (1987) Pristine Moon rocks: a “large” felsite and a metal-rich ferroan anorthosite. Proceedings of the 17th Lunar and Planetary Science Conference, E303–E313.

Warren, P.H., Taylor, G.J., Keil, K., Kallemeyn, G.W., Rosener, P.S., and Wasson, J.T. (1983a) Sixth foray for pristine nonmare rocks and an assessment of the diversity of lunar anorthosites. Proceedings of the 13th Lunar and Planetary Science Conference, A615-A630.

Warren, P.H., Taylor, G.J., Keil, K., Kallemeyn, G.W., Shirley, D.N., and Wasson, J.T. (1983b) Seventh Foray - Whitlockite-rich lithologies, a diopside-bearing troctolitic anorthosite, ferroan anorthosites, and KREEP. Proceedings of the 14th Lunar and Planetary Science Conference, B151–B164.

Warren, P.H., Taylor, G.J., Keil, K., Shirley, D.N., and Wasson, J.T. (1983c) Petrology and chemistry of two 'large' granite clasts from the moon. Earth and Planetary Science Letters, 64, 175–185.

Wilson, L., and Head, J.W. (2003), Lunar Gruithuisen and Mairan domes: Rheology and mode of emplacement. Journal of Geophysical Research, 108, 5012.

Zeigler, R.A., Korotev, R.L., Jolliff, B.L., Haskin, L.A., and Floss, C. (2006) The geochemistry and provenance of Apollo 16 mafic glasses. Geochimica et Cosmochimica Acta, 70, 6050-6067.

Table 1. The bulk composition of 12032,366-19.

	M1	% Error	INAA	1σ		M1	INAA	1σ
SiO_2	70.1	0.15	-	-	**Sm**	-	24.6	0.3
TiO_2	1.07	1.8	-	-	**Eu**	-	3.01	0.03
Al_2O_3	13.5	0.23	-	-	**Tb**	-	6.56	0.07
FeO	4.98	0.54	4.99	0.05	**Yb**	-	51.8	0.5
MnO	0.07	5.7	-	-	**Lu**	-	7.44	0.08
MgO	0.14	0.81	-	-	**Sc**	-	8.7	0.09
CaO	3.04	0.41	2.91	0.18	**Co**	-	0.77	0.02
BaO	0.68	1.1	0.68	0.01	**Ni**	-	<25	-
Na_2O	2.47	0.52	2.10	0.02	**Zn**	-	16	3
K_2O	4.58	0.21	4.80	0.24	**Rb**	-	96	2
P_2O_5	0.052	4.5	-	-	**Sr**	-	167	12
SUM	100.7	-	-	-	**Cs**	-	3.67	0.04
Cr	<200	-	11.3	0.6	**Ta**	-	10.4	0.1
Zr	1500	-	1500	20	**W**	-	9	1
Hf	37.8	-	45.5	0.5	**Ir**	-	<1.3	-
Nb	304	-	-	-	**Au**	-	<5	-
La	11.3	-	79.4	0.8	**Y**	457	-	-
Ce	106	-	182	2	**Th**	126	60.6	0.6
Nd	83.2	-	82	2	**U**	52.7	20.7	0.2

Oxide values are in wt%; element values are in ppm except Ir and Au which are in ppb. The bulk composition of was measured by INAA (Korotev et al. 2007); uncertainties (1σ) are 1 standard deviation estimates of analytical uncertainty based mainly on counting statistics. The "M1" (Model 1) composition and "% Error" were derived by modal recombination using the average phase compositions from the microprobe (Table 2) to "best fit" the bulk rock INAA data (see text).

Table 2. Modal mineralogy of 12032, 366-19.

		Abundance	
Phase	Composition	Image	Model 1
K-feldspar	$An_{1.2-6.1}Ab_{25-33}Or_{58-74}Cn_{0.4-3.9}$	49	43.5
Quartz	$(Si,Al,Fe,Ti)O_2$	31	26
Plagioclase	$An_{35-48}Ab_{52-64}Or_{0.9-1.3}Cn_{0.0-0.1}$	6.2	19
Pyroxene	$En_{4.6-6.2}Fs_{51-52}Wo_{43-44}$	7.3	6.0
Olivine	$Fo_{2.7}Fa_{97}$	4.5	3.1
Ilmenite	$Il_{99.6}Gk_{0.4}$	1.8	1.7
Zirconolite	$(Fe,Y,Ca,REE)(Zr,Hf,U,Th)(Ti,Nb,Al,Si,Ta)_2O_7$	0.13	0.30
REE-rich apatite	$(Ca,REE,Y,Fe)_5([P,Si]O_4)_3(F,Cl)$	Trace	0.2
Apatite	$(Ca,Fe)_5(PO_4)_3(F,Cl)$	Trace	0.1
RE-merrillite	$(Ca,REE)_{16}(REE,Y)_2(Fe,Mg)_2([P,Si]O_4)_{14}$	Trace	0.08
ZrO_2	$Zr_{98.4}Hf_{1.6}$	0. 07	0.058
Sum		100	100

Cn = Celsian (Ba-feldspar end-member), Gk = Geikielite (Mg endmember of ilmenite solid-solution), Zr = Zirconium, Hf = Hafnium.

"Image" is the modal mineralogy of the 12032, 366-19 polished section directly determined by image analysis. "Model 1" was derived from a modal recombination using the average mineral compositions from the microprobe to "best fit" the bulk rock compositions from INAA (see text). All values are converted to weight percent. Zirconolite and phosphate formulae are idealized. Compositions are in Tables 3, 4a, and 4b.

Table 3. Minerals in 12032,366-19.

	Kfs	Kfs*	Qz	Pl	Hd	Fa	Ilm	Apatite	RE-Ap	Merr	Glass Incl.	M1
N	66	3	11	16	6	5	1	3	13	1	1	-
SiO_2	64.2	67.2	101.5	58.6	47.6	29.4	<0.03	2.01	3.17	0.90	78.3	70.0
TiO_2	0.063	0.04	<0.05	<0.04	0.92	0.13	51.1	n.a.	n.a.	n.a.	0.13	1.04
Al_2O_3	20.3	18.8	0.21	26.3	0.69	<0.02	<0.02	<0.02	0.05	<0.02	12.4	13.5
Cr_2O_3	<0.04	<0.04	<0.04	<0.04	<0.04	<0.04	<0.04	n.a.	n.a.	n.a.	<0.03	<0.02
FeO	0.12	0.46	0.21	0.21	29.3	68.6	47.4	0.90	1.79	5.24	1.10	4.99
MnO	<0.04	<0.04	<0.04	<0.04	0.34	0.83	0.43	<0.03	0.09	0.07	<0.04	0.12
MgO	<0.02	<0.02	<0.02	<0.02	1.65	1.06	0.12	<0.02	<0.02	0.59	<0.01	0.13
CaO	1.34	0.23	<0.10	8.56	19.2	0.17	<0.02	54.6	46.6	36.9	0.48	2.9
BaO	1.43	0.26	<0.06	<0.04	<0.05	<0.04	<0.05	n.a.	n.a.	n.a.	0.079	0.68
Na_2O	3.71	2.43	<0.04	6.57	0.10	<0.05	<0.05	0.10	0.17	0.07	0.86	2.10
K_2O	9.82	12.6	0.02	0.19	<0.01	<0.01	<0.01	n.a.	n.a.	n.a.	2.95	4.8
P_2O_5	<0.01	<0.01	<0.02	<0.01	<0.01	<0.01	<0.01	38.4	33.9	40.4	<0.01	0.039
Y_2O_3	n.a.	n.a.	n.a.	n.a.	n.a.	n.a.	n.a.	0.18	1.30	2.45	n.a.	n.a.
REE_2O_3	n.a.	n.a.	n.a.	n.a.	n.a.	n.a.	n.a.	1.13	7.21	12.6	n.a.	n.a.
F	n.a.	n.a.	n.a.	n.a.	n.a.	n.a.	n.a.	1.47	0.96	<0.02	n.a.	n.a.
Cl	n.a.	n.a.	n.a.	n.a.	n.a.	n.a.	n.a.	1.34	1.32	<0.01	n.a.	n.a.
-O=F	-	-	-	-	-	-	-	0.62	0.40	-	-	-
-O=Cl	-	-	-	-	-	-	-	0.34	0.30	-	-	-
Sum	101.0	102.0	102.4	100.6	99.8	100.1	100.2	99.3	95.9	99.2	96.4	100.0

Ilmenite also contains ~1 wt% Nb_2O_5, but V_2O_5 was below the detection limit; for oxide abundances in zirconolite, see Table 4a.

All values are reported in weight percent (wt%). *N* is the number of analyses averaged. “Kfs*” is a single analysis of a K-feldspar in an inclusion within a hedenbergite grain. “RE-Ap” refers to apatite analyses with high REE concentration. “Merr” refers to RE-merrillite. The “M1” (Model 1) composition was derived by modal recombination using the average phase compositions from the microprobe (Table 2) to “best fit” the bulk rock INAA data (see text and Table 1). “n.a.” means “not analyzed.” REE_2O_3 was estimated from La, Ce, Nd, Gd, Y, and Yb included in the analyses (details in Experimental Procedures).

Table 4a. Zirconolite analyses containing the lowest concentrations of SiO_2 and those in which PbO was included.

Spot	**Sum**	**ZrO_2**	**TiO_2**	**Y_2O_3**	**FeO**	**Nb_2O_5**	**CaO**	**ThO_2**	**UO_2**	**PbO**	**HfO_2**	**Ta_2O_5**	**Al_2O_3**	**SiO_2**	**MnO**
1930	97.48	28.73	24.28	9.85	9.32	7.42	4.30	2.46	1.10	-	0.58	0.32	0.13	<0.01	0.09
1931	97.52	28.72	24.25	9.92	9.37	7.29	4.26	2.34	1.06	-	0.57	0.31	0.23	0.21	0.10
1936	98.74	30.21	24.05	9.73	8.84	7.81	4.70	1.45	0.50	-	0.81	0.29	0.11	0.31	0.11
1938	97.36	29.57	24.11	8.96	8.59	7.27	4.62	2.33	0.72	-	0.67	0.32	0.17	0.41	0.08
1943	94.55	21.43	17.43	6.67	6.65	5.07	3.18	1.39	0.37	0.60	0.63	0.24	0.13	21.08	0.06
1944	99.00	22.05	18.61	6.85	7.12	5.19	3.30	1.38	0.38	0.63	0.64	0.27	0.11	22.21	0.09
1945	91.95	23.81	19.15	7.18	7.27	5.65	3.61	1.71	0.43	0.74	0.62	0.22	0.12	11.05	0.07
1946	103.94	24.15	20.23	7.62	7.47	5.94	3.75	1.29	0.40	0.54	0.66	0.18	0.14	19.81	0.06
12013	89.7	17.2	22.1	9.1	11.6	8.3	3.0	4.1	3.4	-	-	-	-	2.1	-
Mare	100.28	30.61	28.51	9.05	9.70	3.91	3.18	0.11	0.05	-	0.60	0.24	0.41	0.08	0.00

Spot	**La_2O_3**	**Ce_2O_3**	**Pr_2O_3***	**Nd_2O_3**	**Sm_2O_3***	**Gd_2O_3***	**Tb_2O_3***	**Dy_2O_3***	**Ho_2O_3***	**Er_2O_3***	**Tm_2O_3***	**Yb_2O_3**	**Lu_2O_3***
1930	0.23	1.59	0.19	1.38	0.52	0.81	0.16	1.16	0.28	0.98	0.17	1.22	0.21
1931	0.17	1.61	0.18	1.44	0.54	0.83	0.16	1.17	0.29	0.97	0.16	1.17	0.19
1936	0.30	2.26	0.23	1.58	0.58	0.86	0.17	1.18	0.28	0.93	0.15	1.11	0.18
1938	0.24	2.28	0.21	1.60	0.57	0.83	0.16	1.11	0.26	0.88	0.15	1.09	0.18
1943	0.20	1.74	0.33	2.19	1.19	0.85	0.15	1.06	0.25	0.75	0.12	0.83	0.14
1944	0.24	1.83	0.35	2.30	1.24	0.88	0.16	1.10	0.26	0.79	0.13	0.88	0.15
1945	0.26	1.82	0.35	2.30	1.26	0.90	0.16	1.13	0.27	0.81	0.13	0.90	0.15
1946	0.32	2.42	0.45	2.88	1.49	1.04	0.18	1.23	0.28	0.82	0.13	0.85	0.13
12013	0.2	1.7	-	-	-	-	-	-	-	-	-	-	-
Mare	0.19	1.64	0.47	3.48	1.67	2.62	-	2.34	-	0.99	-	0.43	-

REE oxides with * are estimated concentrations based on the measured REE values (see text). All values are in wt%. “Mare” is an average of 12 analyses from 7 zirconolite grains in 10047,11, 10047,227 and 10047,230 (Rasmussen et al. 2008). “12013” is an average of two zirconolite analyses from granitic lunar breccia 12013 (Haines et al. 1971). The * does not apply to “Mare” or “12013.” “-” means “not reported.”

Table 4b. Zirconolite formula calculation.

A	Ca	0.3220	0.3179	0.3455	0.3441
	Fe	0.5449	0.5456	0.5065	0.4999
	Mn	0.0055	0.0059	0.0066	0.0048
	Sum	0.8724	0.8694	0.8587	0.8487
B	Y	0.3665	0.3676	0.3549	0.3316
	La	0.0059	0.0045	0.0077	0.0061
	Ce	0.0406	0.0411	0.0568	0.0580
	Pr*	0.0048	0.0045	0.0057	0.0054
	Nd	0.0345	0.0358	0.0388	0.0397
	Sm*	0.0126	0.0130	0.0137	0.0137
	Gd*	0.0187	0.0191	0.0195	0.0190
	Tb*	0.0037	0.0037	0.0038	0.0036
	Dy*	0.0260	0.0263	0.0261	0.0249
	Ho*	0.0063	0.0064	0.0062	0.0059
	Er*	0.0214	0.0211	0.0201	0.0192
	Tm*	0.0036	0.0035	0.0033	0.0032
	Yb	0.0261	0.0249	0.0231	0.0232
	Lu*	0.0043	0.0041	0.0037	0.0038
	Sum	0.5753	0.5757	0.5834	0.5573
C	Zr	0.9794	0.9753	1.0100	1.0029
	Hf	0.0116	0.0113	0.0158	0.0132
	U	0.0171	0.0164	0.0076	0.0111
	Th	0.0391	0.0370	0.0226	0.0369
	Sum	1.0473	1.0400	1.0560	1.0641
D	Ti	1.2761	1.2701	1.2399	1.2610
	Si	0.0000	0.0148	0.0214	0.0287
	Nb	0.2346	0.2295	0.2419	0.2285
	Ta	0.0062	0.0059	0.0054	0.0060
	Al	0.0104	0.0190	0.0088	0.0139
	Sum	1.5272	1.5393	1.5175	1.5380
M_I	A	0.8724	0.8694	0.8587	0.8487
	B	0.1276	0.1306	0.1413	0.1513
	Sum	1.0000	1.0000	1.0000	1.0000
M_{II}	C	0.5523	0.5549	0.5579	0.5939
	B	0.4477	0.4451	0.4421	0.4061
	Sum	1.0000	1.0000	1.0000	1.0000
M_{III}	D	1.5272	1.5393	1.5175	1.5380
	Zr	0.4272	0.4204	0.4521	0.4090
Sum	1.9544	1.9597	1.9696	1.9470	
M_I+M_{II}+M_{III}		**3.9544**	**3.9597**	**3.9696**	**3.9470**

Methodology follows that of Wark et al. (1973) for four selected analyses. Ideally, M_I, M_{II}, and M_{III} should sum to 4. Elements with a * are estimated concentrations based on the measured REE values (see text).

Table 5. KB and BAG, and silicic immiscible liquid compositions.

	KB[1]	BAG[2]	SLI[3]	SLI[4]	SLI[4]	SLI[5]	SLI[6]
SiO_2	52.8	52.53	73.3	71.8	79.7	68.42	72.18
TiO_2	2.14	3.58	0.8	0.7	0.6	1.55	0.60
Al_2O_3	15.2	12.9	12.1	10.2	10.6	8.1	13.38
Cr_2O_3	0.29	0.13	-	-	-	-	-
FeO	10.1	13.28	3.2	4.0	3.5	7.26	4.10
MnO	0.15	0.18	0.0	0.0	0.0	0.06	0.26
MgO	7.4	4.82	0.0	1.1	0.6	1.92	1.06
CaO	9.4	9.1	1.8	6.5	1.2	2.84	2.90
Na_2O	0.89	0.97	3.1	2.2	2.2	2.33	0.75
K_2O	0.65	0.68	3.3	3.5	1.6	2.84	1.40
P_2O_5	0.62	0.51	0.07	0.0	0.0	0.0	0.37
SUM	99.6	98.68	97.7	100.0	100.0	95.3	97.0

Units are wt%. [1]Compiled by Papike et al. 1998. [2]Zeigler et al. 2006. [3]Philpotts 1982. [4]Philpotts 1981. [5]Krasov and Clocchiatti 1979. [6]Ryabov 1989.

Table 6. Compositions and characteristics of residual liquids in KB and BAG fractional crystallization models.

Wt%	**KB**					**BAG**				
Liquid	**100**	**75.3**	**51.3**	**26.1**	**10.6**	**100**	**74.69**	**50.19**	**25.67**	**14.58**
SiO_2	53.0	54.3	54.5	53.0	57.6	53.2	53.4	52.2	53.5	55.1
TiO_2	2.2	2.7	4.0	3.2	0.4	3.6	4.7	4.4	2.1	0.5
Al_2O_3	15.3	13.9	12.9	12.5	14.6	13.1	12.1	11.7	12.1	13.4
Cr_2O_3	0.3	0.1	0.1	0.1	0.2	0.1	0.1	0.1	0.1	0.1
FeO	10.1	11.3	12.9	14.7	12.6	13.5	14.5	15.9	17.2	15.3
MgO	7.4	5.8	3.5	1.8	0.4	4.9	3.4	2.5	1.2	0.3
MnO	0.2	0.2	0.2	0.3	0.4	0.2	0.2	0.3	0.3	0.4
CaO	9.4	9.0	8.6	8.5	4.2	9.2	9.0	9.5	7.7	5.6
K_2O	0.7	0.8	1.2	2.2	5.0	0.7	0.9	1.3	2.3	3.9
Na_2O	0. 9	1.0	1.1	1.4	1.9	1.0	1.1	1.2	1.6	1.9
P_2O_5	0.6	0.8	1.2	2.3	2.5	0.5	0.7	1.0	1.9	3.4
T(°C)	1147	1122	1078	1047	915	1092	1077	1062	1036	1017
η_S	125	260	618	702	66700	285	412	365	864	2650
$\eta_{B\text{-}W}$	106	196	471	787	20100	279	420	511	1120	3530

Oxides and temperatures are calculated by the MAGFOX program (Longhi 1991). η_S and $\eta_{B\text{-}W}$ are the dynamic viscosities calculated using the KWare Magma program (Ken Wohletz, Version 2.49.0126) by the methods of Shaw (1972) and Bottinga and Weil (1972), respectively.

Table 7. Bulk compositions of 12032,366-19, selected lunar granites, and selected high SiO_2 immiscible liquids.

	1	2	3	4	5	6	7	8	9	10	11
SiO_2	70.0	73.0	70.8	74.2	68.1	75.5	76.4	74.2	65.8	70.2	70.2
TiO_2	1.04	0.60	0.60	0.33	0.90	0.26	0.7	0.7	2.3	1.17	1.16
Al_2O_3	13.5	11.9	12.7	12.5	10.2	12.3	12.2	11.1	10.6	13.3	13.4
FeO	4.93	0.90	6.30	2.32	6.99	3.10	1.8	6.9	8.5	4.62	4.97
MnO	0.13	0.12	0.10	0.02	-	0.04	-	-	-	-	-
MgO	0.14	0.70	0.40	0.07	1.53	0.20	0.5	0.1	1.5	0.34	0.25
CaO	3.0	1.40	1.00	1.25	4.89	0.50	1.1	2.1	5.7	3.88	3.51
BaO	0.77	0.65	-	0.24	-	0.61	-	-	-	-	-
Na_2O	2.49	1.40	1.10	0.52	0.79	0.53	0.5	0.4	1.6	1.67	1.91
K_2O	4.5	6.80	7.40	8.60	3.39	7.55	6.1	4.2	4.3	4.76	4.58
P_2O_5	0.039	-	0.70	-	-	-	0.01	0.2	0.3	-	-
ZrO_2	0.203	0.15	-	0.09	-	-	-	-	-	-	-
Hf	41.9	24	-	13.9	-	16	-	-	-	-	-
Cr	56	1010	0	17	-	70	-	-	-	0	0
Y	494	-	-	-	-	-	-	-	-	-	-
Th	132	41	-	65	-	9.5	-	-	-	-	-
U	45	12.3	-	23.4	-	-	-	-	-	-	-
SUM	100.8	97.6	101.1	100.1	96.7	100.6	99.3	99.9	100.6	100.0	100.0

Oxide units are wt%. Element units are ppm. 1. 12032,366-19: This study – microprobe and modal recombination. 2. 12013,10 light: Hubbard et al. 1970, Schnetzler et al. 1970, Wakita and Schmitt 1970, and Quick et al. 1977. 3. 12070,102-5: Potash rhyolite, Marvin et al. 1971. 4. 14321,1027: Pristine granite clast, Warren et al. 1983c. 5. 15405,12: Granite fragments, Ryder 1976. 6. 73255,27,3: Felsite clast, Blanchard and Budahn 1979. 7. Average compositions of six immiscible granitic inclusions in sample 14310,5, Roedder and Weiblen 1972. 8. Experimentally-produced high SiO_2 liquid from the fractionation of sample 12038,105, Hess et al. 1975. 9. Experimentally-produced high SiO_2 liquid from the fractionation of a composition similar to 15405 KREEP basalt, Rutherford et al. 1976. 10 and 11 are modeled compositions of low-density minerals in equilibrium with the melts of KB and BAG, respectively, in the last stages of fractional crystallization.

Figure 1. Photograph of sample 12032,366-19 top (a) and bottom (b) with a 1-mm grid in the background. K-feldspar, plagioclase, and silica appear white. Hedenbergite, fayalite, and ilmenite are the dark phases.

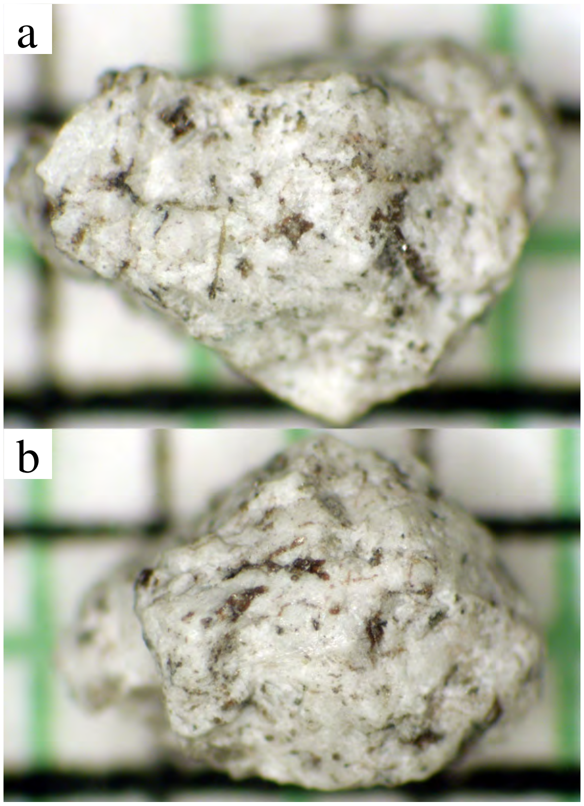

Figure 2. Positive linear time dependence of F X-ray count-rates (counts per second). (a) and (a) are analyses of the REE-rich apatite. (c) is an analysis of apatite. (d) is an analysis of the Durango fluorapatite (Jarosewich et al. 1980) standard. (a), (b), and (c) were analyzed with a 2 μm beam diameter and a 25 nA current. (d) was analyzed with a 20 μm beam diameter and a 25 nA current.

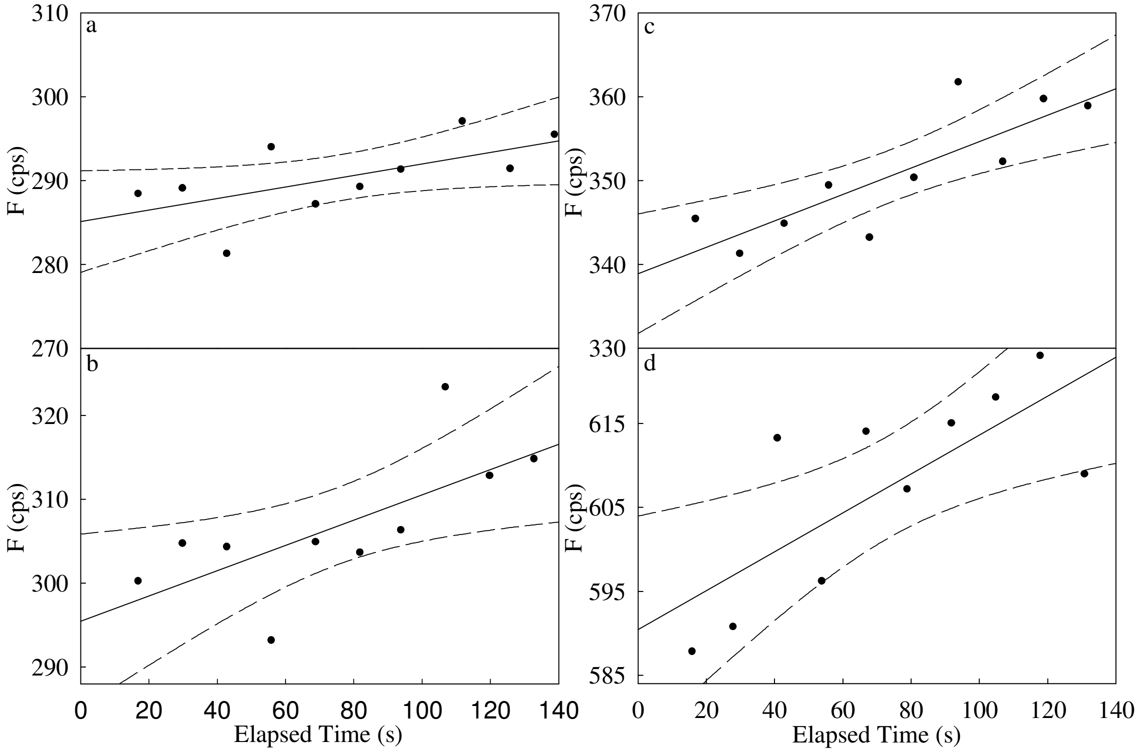

Figure 3. Back-scattered electron (BSE) image mosaic of 12032,366-19. In order of brightness from darkest to brightest, minerals are quartz, sodic plagioclase, K-feldspar, hedenbergite, fayalite and ilmenite, and zirconolite and baddeleyite. See Fig. 4 for phase identifications based on X-ray analysis.

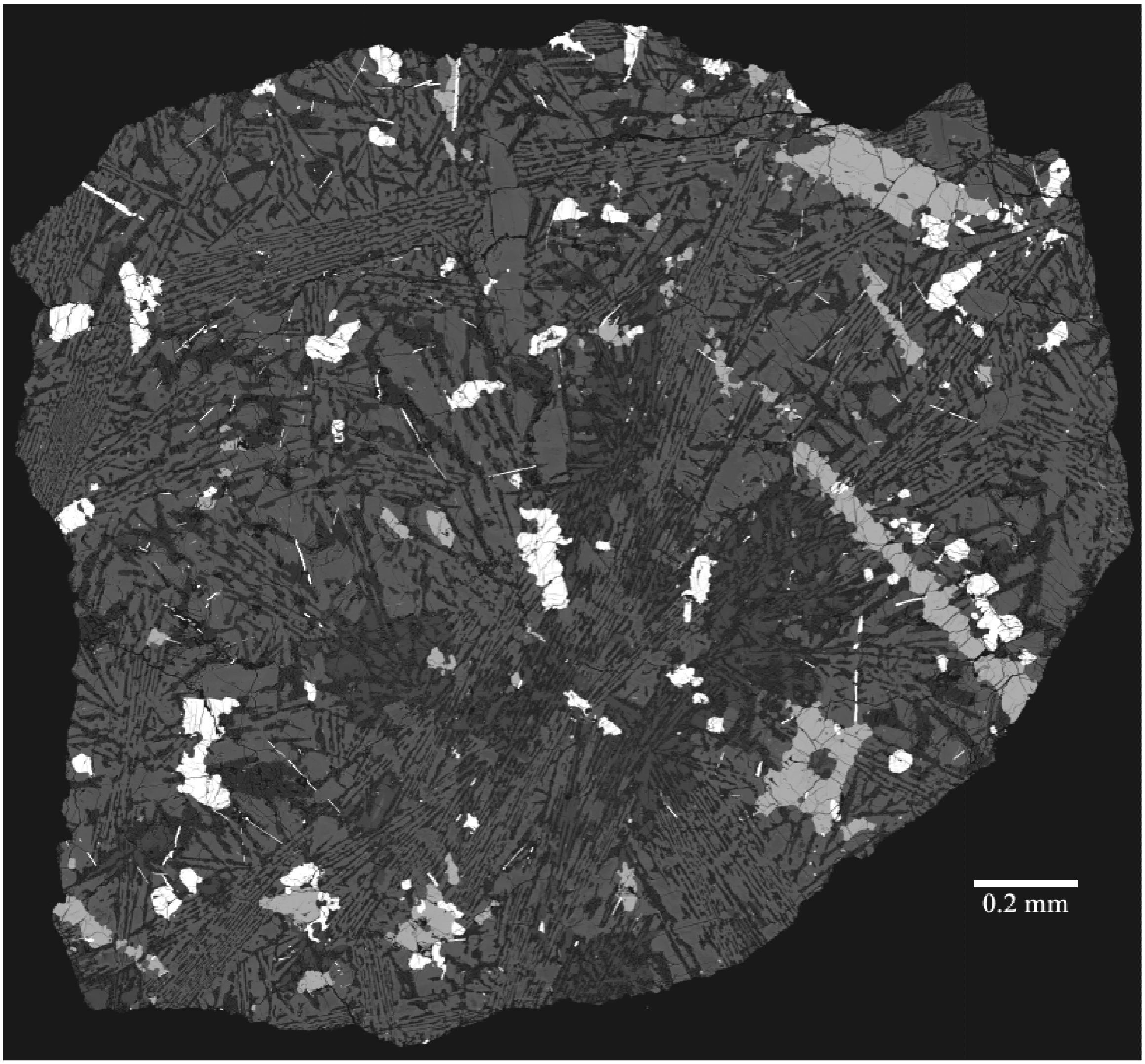

Figure 4. a. An RGB image of 12032, 366-19 with K in the red channel, Na in the green channel, and Fe in the blue channel. With this color scheme, K-feldspar is orange, more sodic K-feldspar is light orange, plagioclase is green, olivine is bright blue, pyroxene is darker blue, and quartz is represented as black. **b.** An RGBGray image of 12032, 366-19 with Ca in the red channel, Zr in the green channel, Ti in the blue channel, and Si in the gray channel. With this color scheme, pyroxene is pink, plagioclase is dull pink, ilmenite is blue, zirconolite and ZrO_2 are green.

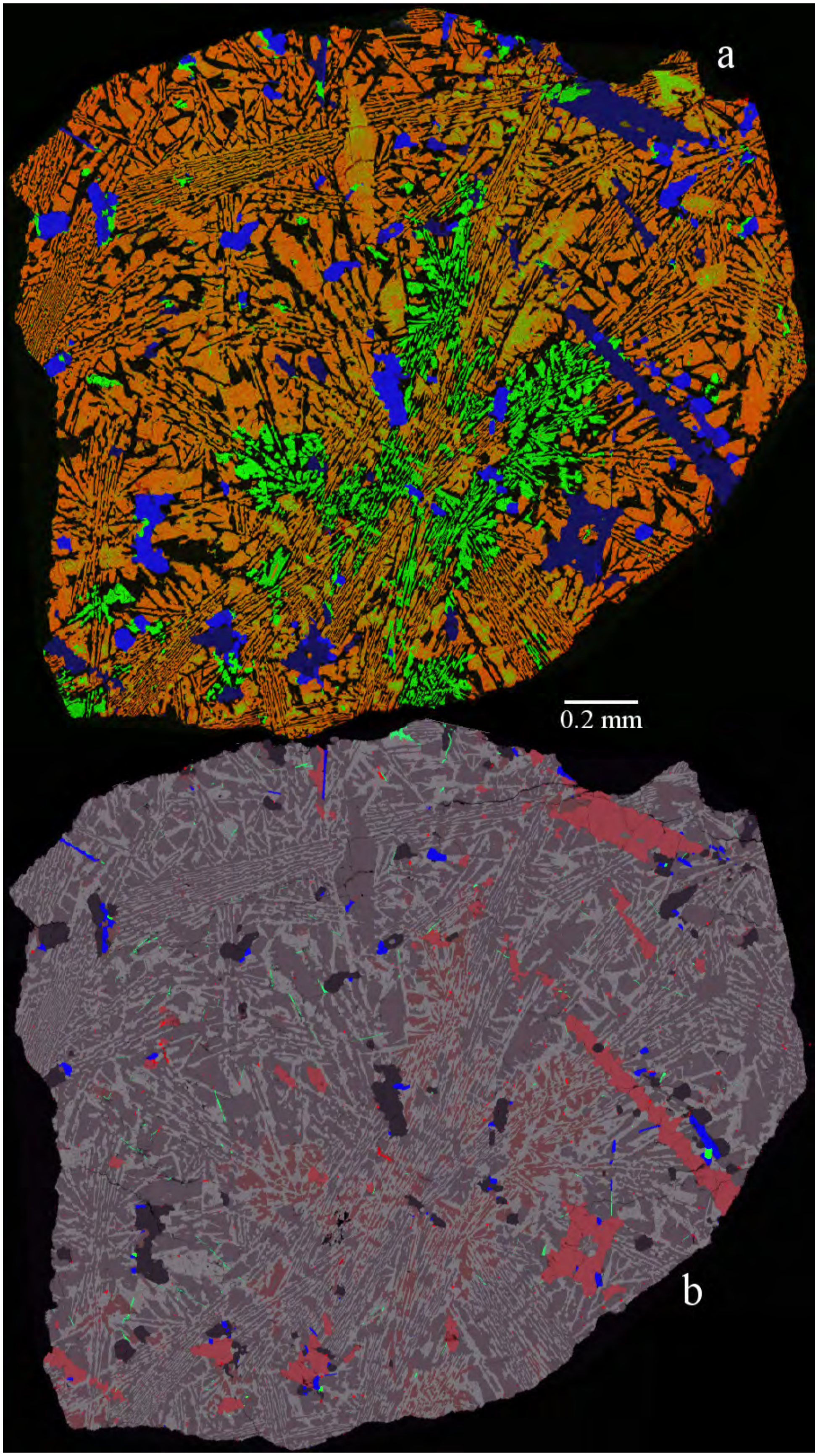
a
0.2 mm
b

Figure 5. Three BSE images of the largest zirconolite grain taken at varying accelerating voltages of 5, 15, and 25 kV. “x” points to a region that is covered by a thin layer of K-feldspar. “y” points to a region where the zirconolite is thin. The thin layers become transparent in the images taken at higher accelerating voltages since the backscattered electrons penetrate deeper into the sample at higher accelerating voltages.

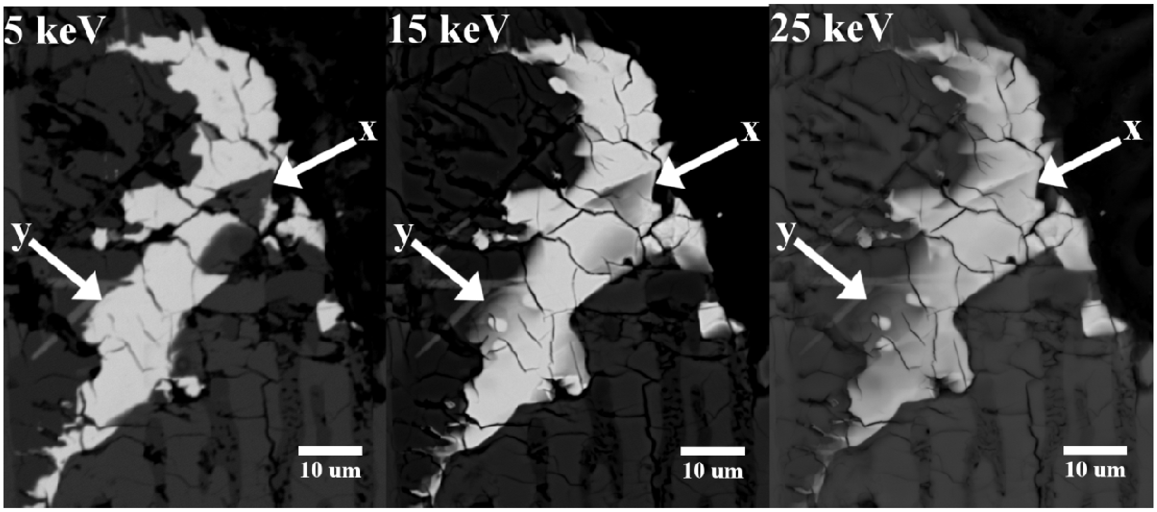

Figure 6. Feldspar ternary diagram showing the K-feldspar and plagioclase compositions found in 12032,366-19. The composition has been normalized to An, Ab, and Or. The celsian (Cn) component is represented by the symbol color.

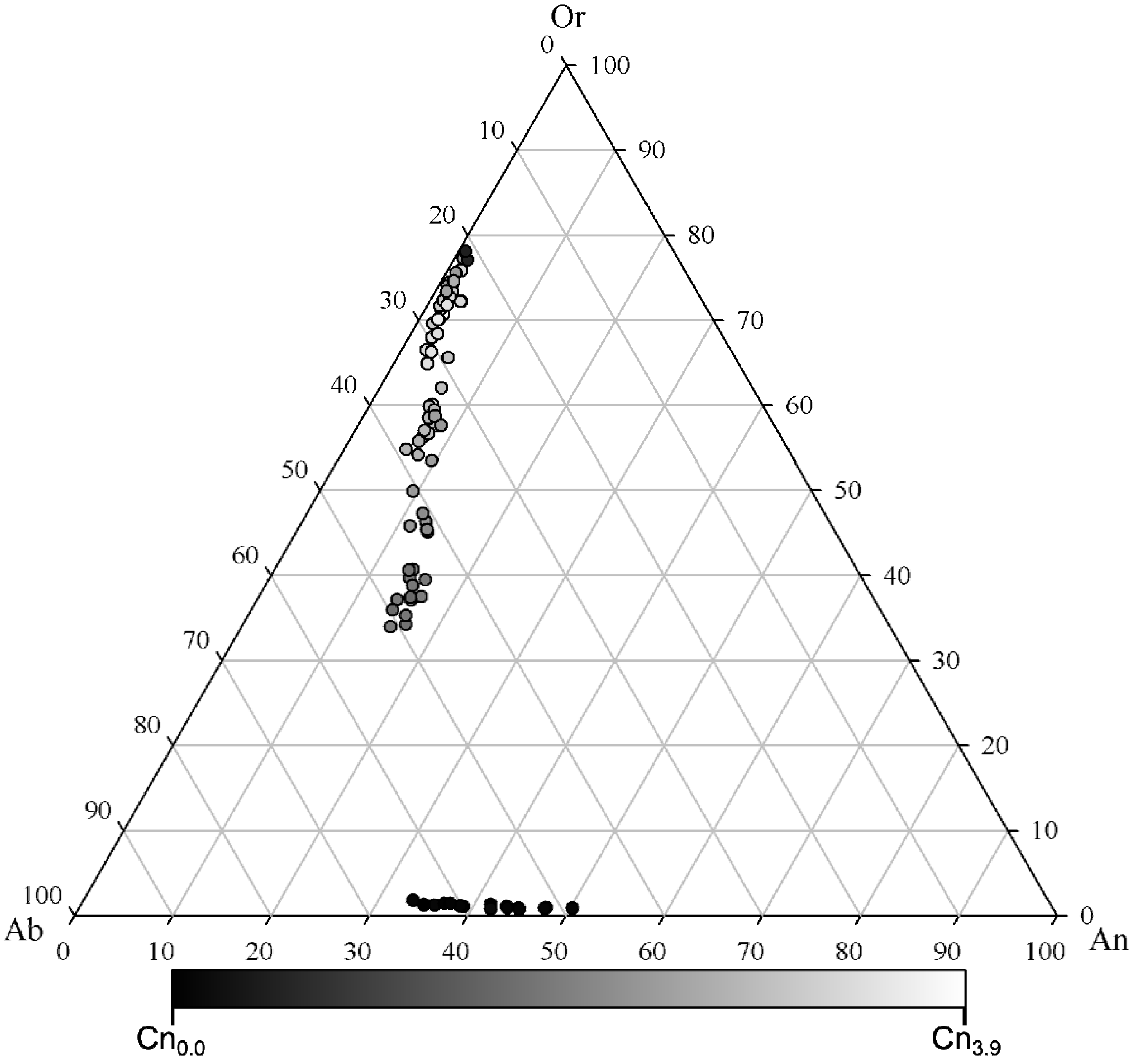

Figure 7. BSE images of textures in 12032,366-19. All 4 BSE images are stretched to the same extent. Hd = hedenbergite, Kfs = K-feldspar, Fa = Fayalite, Ilm = ilmenite, Qz = quartz, and Pl = plagioclase. **a**. The large medium-gray phase transects the image is hedenbergite. The white arrow points to an ilmenite of a typical grain size in this sample. The black arrow points to the largest occurrence of baddeleyite in 12032,366-19. The ZrO_2 is bordered mostly by a coarse ilmenite grain and silica to a lesser extent. **b.** A finely elongate example of zirconolite lies diagonally in the center of the image and is nearly paralleled by another occurrence in the bottom left. **c.** The white arrow points to the irregularly-shaped occurrence of zirconolite discussed in text. The gray arrow points to another occurrence of zirconolite. **d.** The white arrow points to the largest phosphate occurrence; it is REE-rich apatite (Table 3).

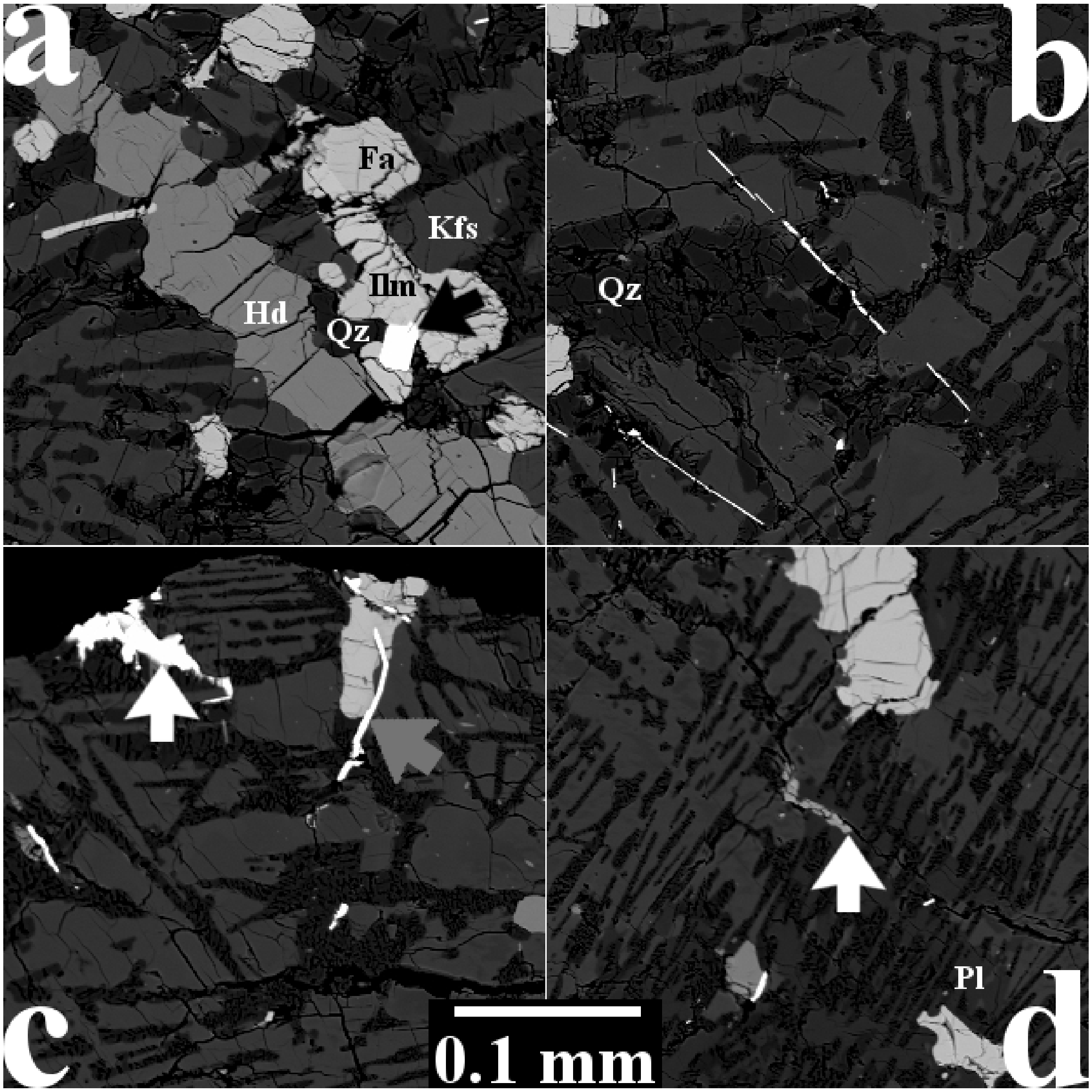
a
Fa
Kfs
Ilm
Hd
Qz
b
Qz
c
0.1 mm
d
Pl

Figure 8. Raman spectra of quartz in 12032,366-19. The "Standard" spectrum is from the RRUFF database.

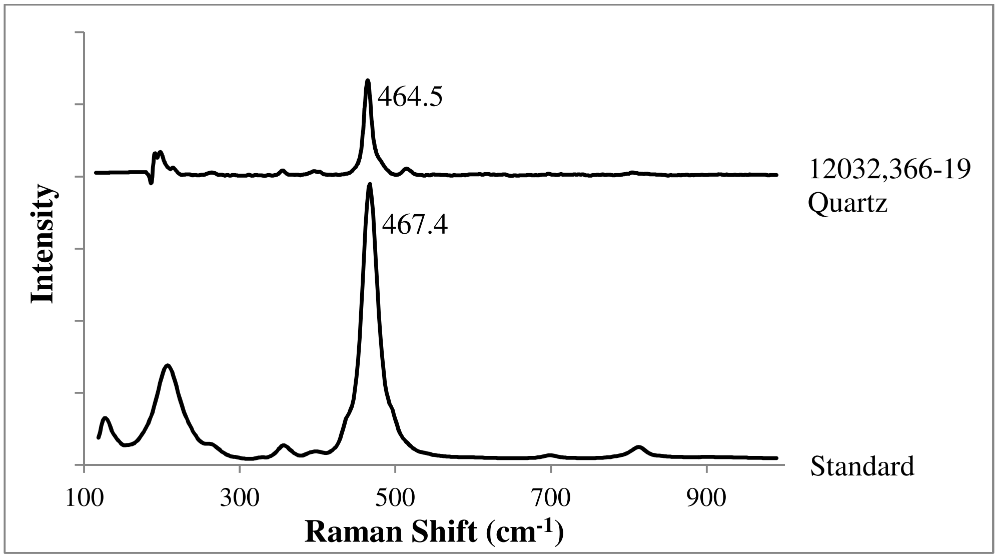

Figure 9. Variations in concentrations of ZrO_2 and other elements with SiO_2 in zirconolite of 12032,366-19 reveals that, in general, the more SiO_2 contained in an analysis, the lower the concentration of everything else. ZrO_2, however, increases as the concentrations of most other oxides increase (except for SiO_2) indicating that the actual zirconolite composition contains little or no SiO_2.

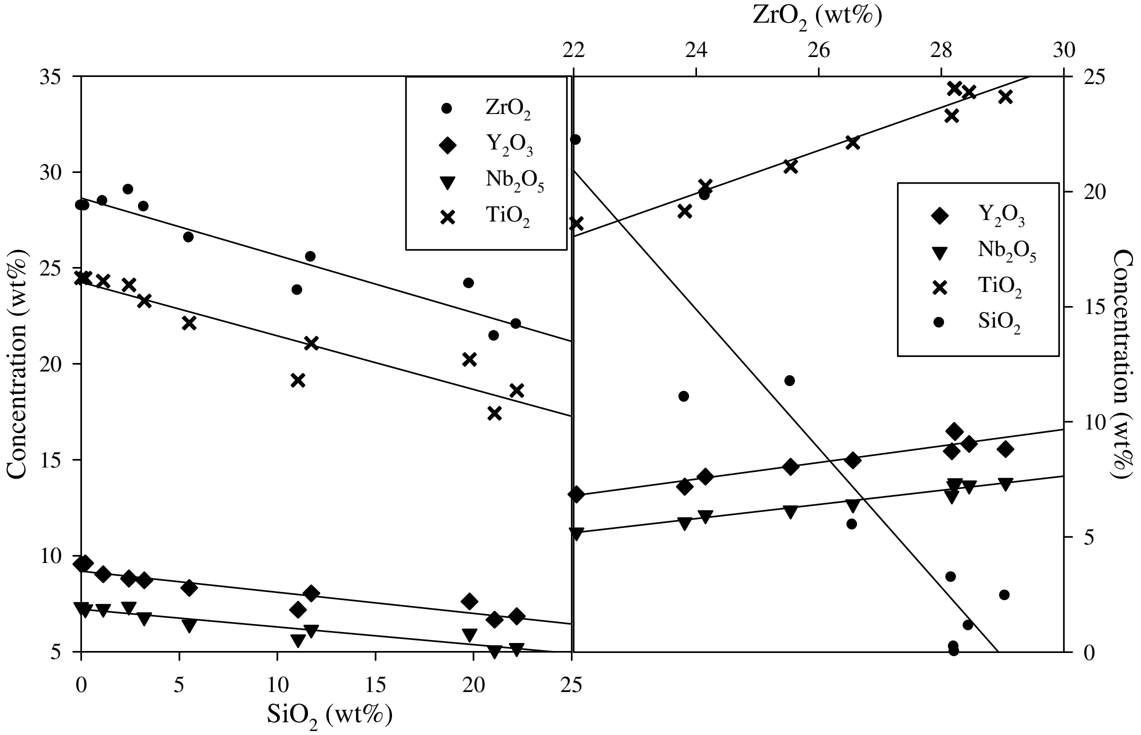

Figure 10. REE plots of zirconolite (shaded gray) and merrillite (shaded gray with diagonal lines) in 12032,366-19. The gray regions are the ranges of concentrations for the four zirconolite analyses with the lowest SiO_2 and the two merrillite analyses; the black solid lines represent the average concentrations. Yttrium is plotted with the REEs (Korotev 1996). The analyzed elements are indicated on the horizontal axis. *Gd was analyzed on merrillite but not zirconolite. The other REE concentrations were estimated (see text). Europium is assumed to be present in low concentration assuming the zirconolite and merrillite crystallized after plagioclase. Chondrite values are those of Anders and Grevesse (1989) for CI chondrites multiplied by a factor of 1.36 to maintain consistent values with older literature, in which data were normalized to ordinary chondrites (Korotev 1996).

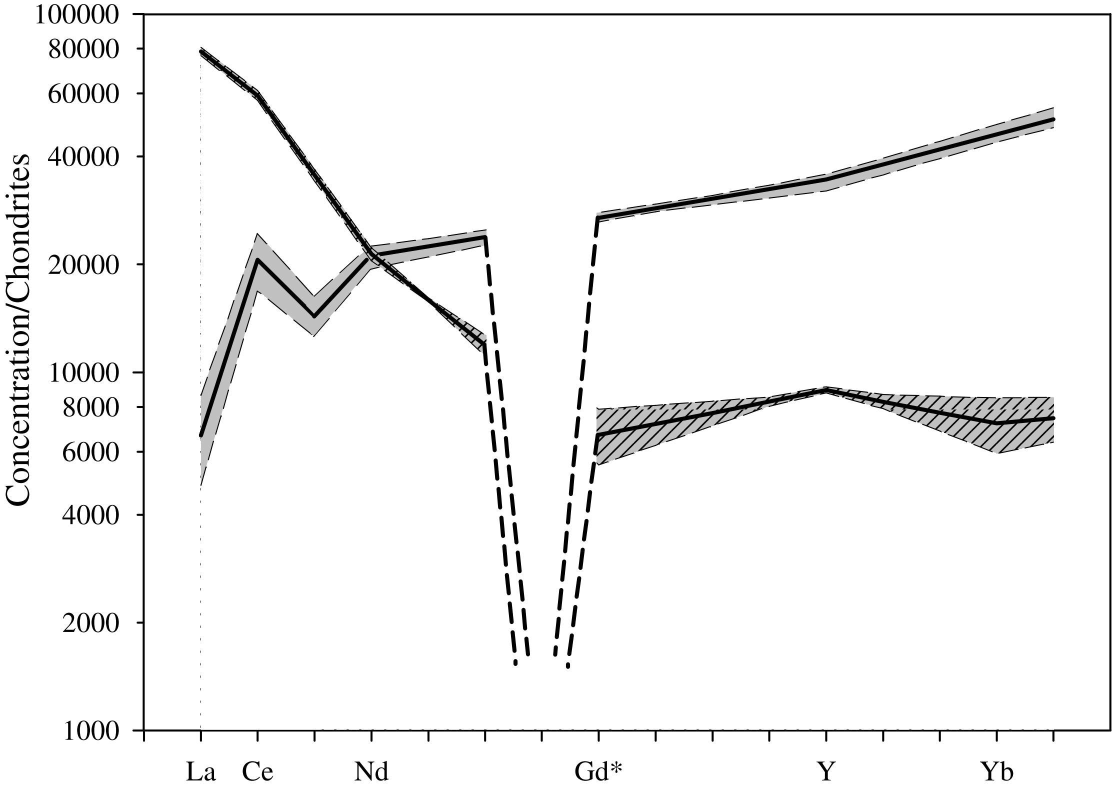

Figure 11. Compositional diagram for Apollo 12 rock fragments (after Fig. 3 of Korotev et al. 2011). Sample 12032,366-19 is shown by the star, plotting at just over 60 ppm Th. The color of each symbol corresponds to the Ba (red channel), Zr (green channel), and Cr (blue channel) concentrations. The granites and a few other points that are enriched in Ba relative to Zr are readily distinguished from those that have normal KREEP-like Ba/Zr (light green).

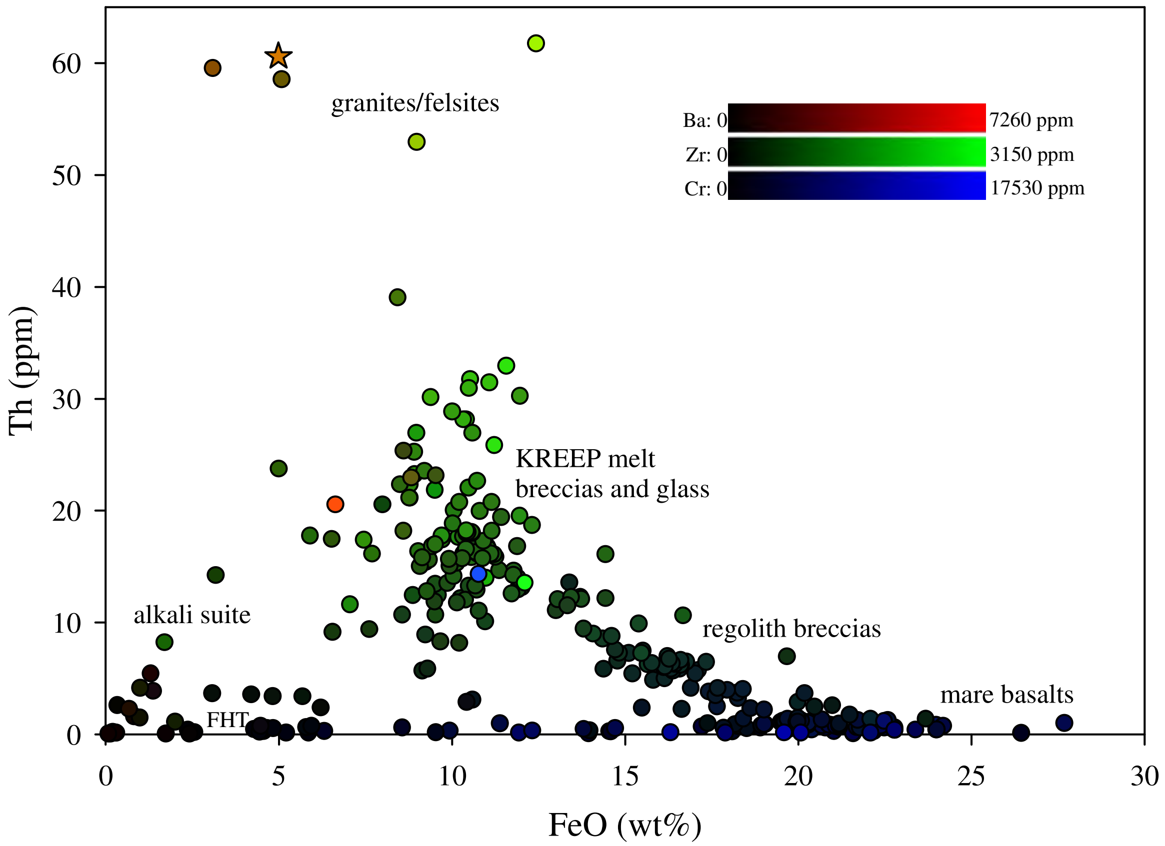

Figure 12. Bulk elemental concentrations of 12032,366-19 compared to High-K KREEP (Warren 1989).

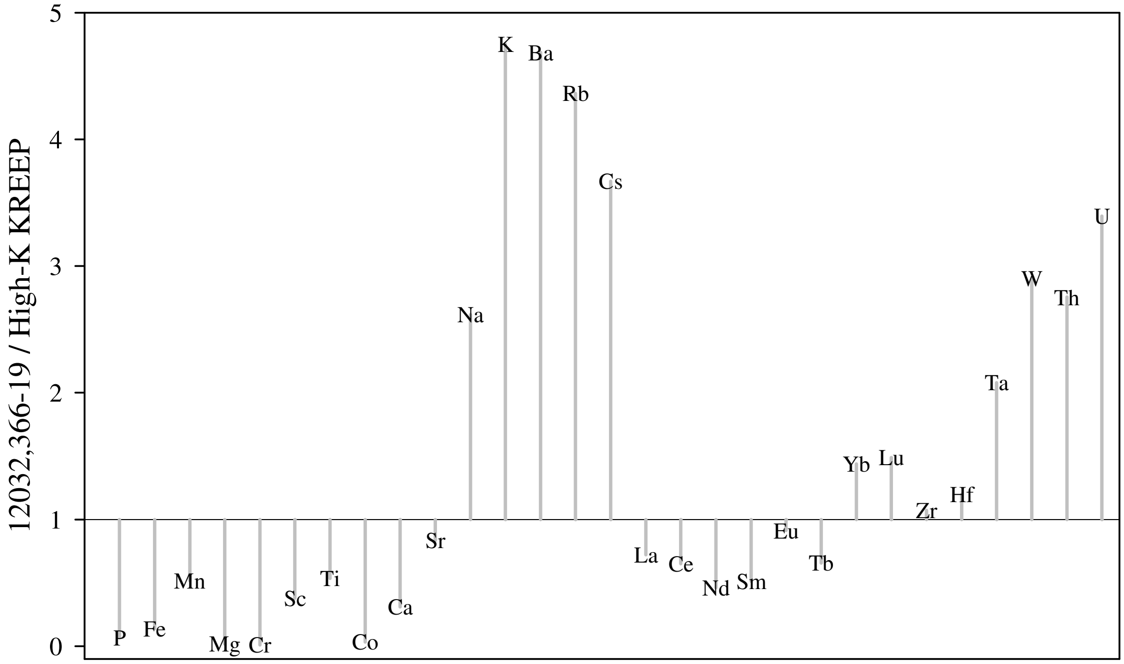

Figure 13. Compared to typical Apollo 12 regolith (Korotev et al. 2011), 12032,366-19 has a “V”-shaped REE pattern common to lunar granitic materials (12013, Quick et al. 1977; 12033,517,Warren et al. 1987; 14321,1028, Warren et al. 1983a; 15434,10, Ryder and Martinez 1991; 73255,27, Blanchard and Budahn 1979; and 14161,7269, Jolliff et al. 1991). 14303,206 (Warren et al. 1983b) has a REE pattern similar to the typical Apollo 12 soil. Chondrite values are those of Anders and Grevesse (1989) for CI chondrites multiplied by a factor of 1.36 to maintain consistent values with older literature, in which data were normalized to ordinary chondrites (Korotev 1996). The analyzed elements are indicated on the horizontal axis; the other REE concentrations were estimated (see text). Samples with “*” include Dy; samples with “**” include Dy and Ho. Ce was estimated for 14161,7269.

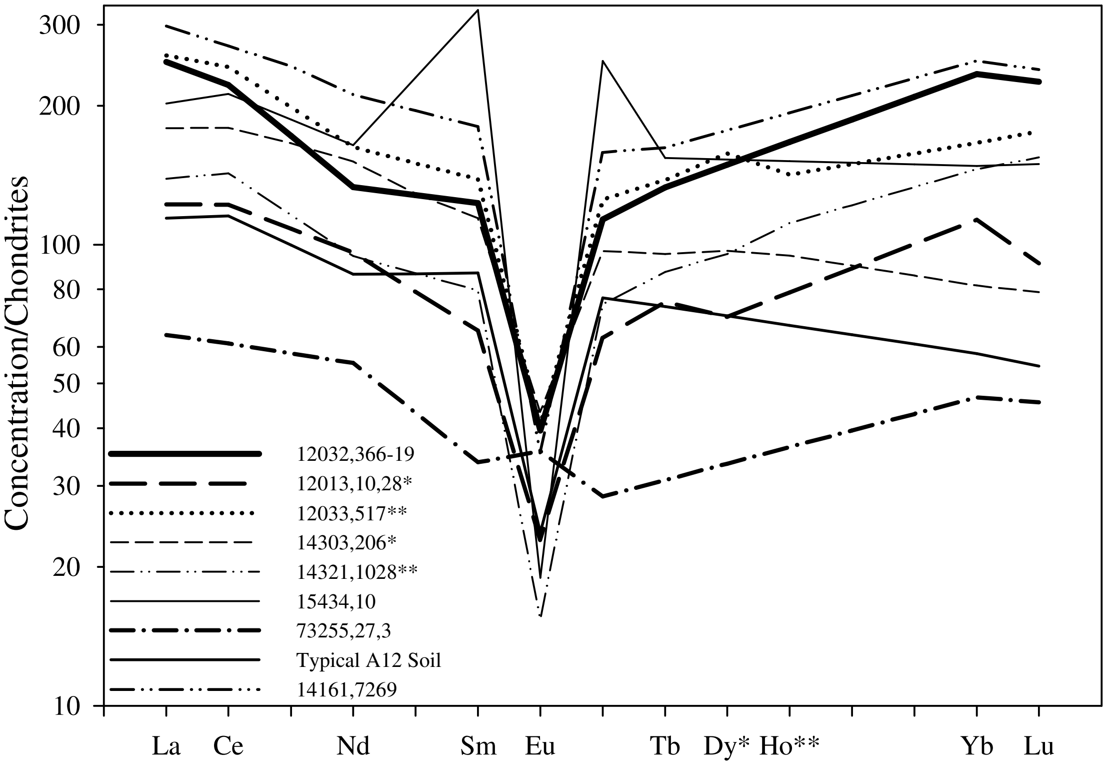

Figure 14. Mg# of pyroxenes in lunar granites (12032,366-19; 12033,507; 14303,204; 15405,12; and 15434,10) and two quartz-monzogabbros (14161,7069 and 14161,7373) plotted against the An content of the plagioclase in the same samples. The coexisting pyroxene and plagioclase from fractional crystallization modeling is also plotted. The earlier crystallization is in the upper-right and crystallization proceeds down to the lower-left. The KB starting composition produced 3 pyroxenes; the BAG starting composition produced 2 pyroxenes. The gray rectangle represents the region occupied by 14303,204; 15405,12; and 15434,10, which each considerably overlap each other. 12033,507 and 14303,204 (Warren et al. 1987). 14161,7069 and 14161,7373 (Jolliff 1991). 15405,12 (Ryder 1976). 15434,10 (Ryder and Martinez 1991).

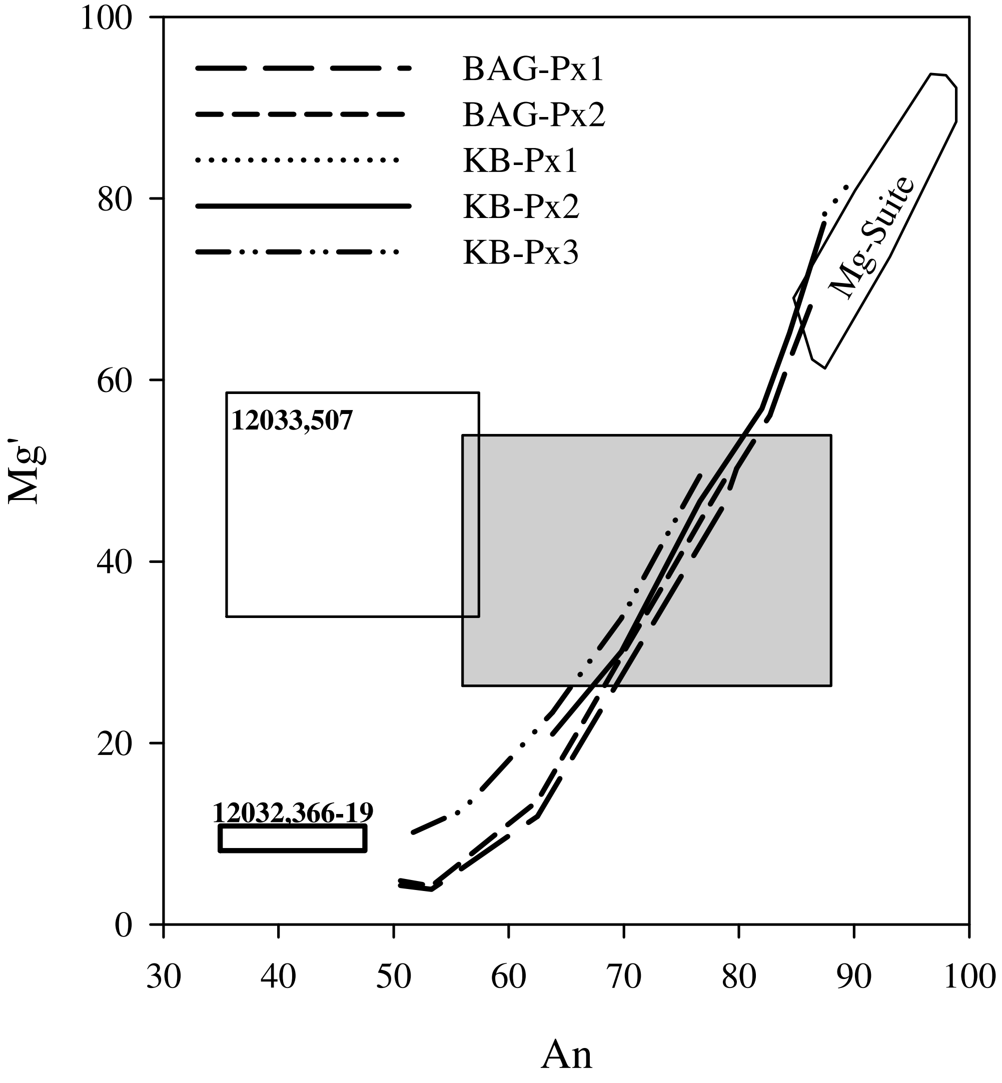
BAG-Px1
BAG-Px2
KB-Px1
KB-Px2
KB-Px3
Mg-Suite
12033,507
12032,366-19
Mg'
An
0
20
40
60
80
100
30
40
50
60
70
80
90
100

Figure 15. SiO_2, Al_2O_3, FeO, CaO, MgO, TiO_2, K_2O, P_2O_5, and Na_2O plotted vs. residual liquid along with the crystallizing mineral assemblage plotted vs. residual liquid (all in wt%). The plotted lines representing the wt% minerals crystallizing are qualitatively smoothed representations of the output of the MAGFOX program (Longhi 1991). Rock names of the crystallizing mineral assemblages (based on the QAPF diagram) and indicated by the background shade.

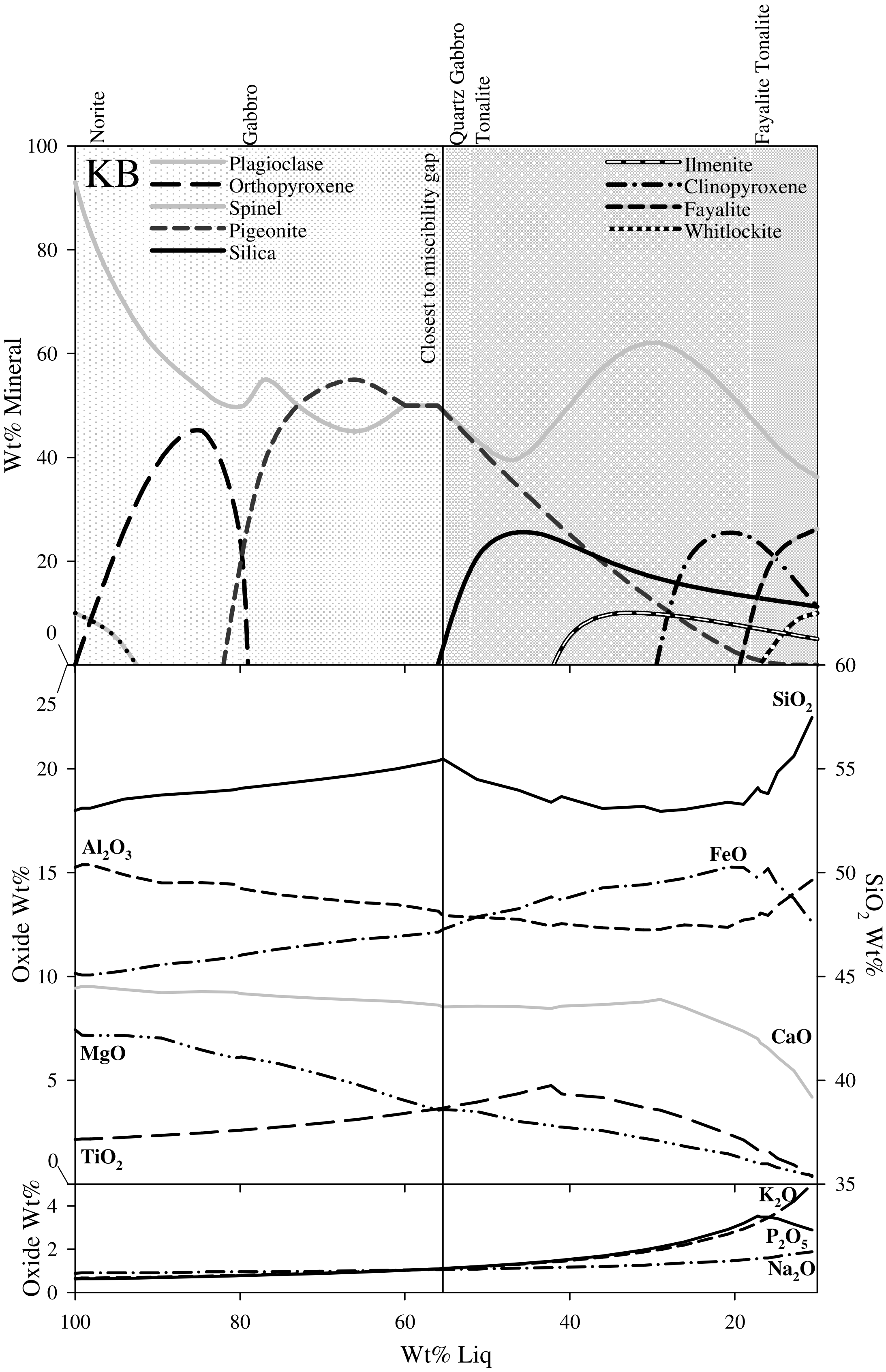

Norite
Gabbro
Quartz Gabbro
Tonalite
Fayalite Tonalite
Closest to miscibility gap
KB
Plagioclase
Orthopyroxene
Spinel
Pigeonite
Silica
Ilmenite
Clinopyroxene
Fayalite
Whitlockite
Wt% Mineral
100
80
60
40
20
0
Oxide Wt%
25
20
15
10
5
0
SiO_2
Al_2O_3
FeO
CaO
MgO
TiO_2
SiO_2 Wt%
60
55
50
45
40
35
Oxide Wt%
4
2
0
K_2O
P_2O_5
Na_2O
100
80
60
40
20
Wt% Liq

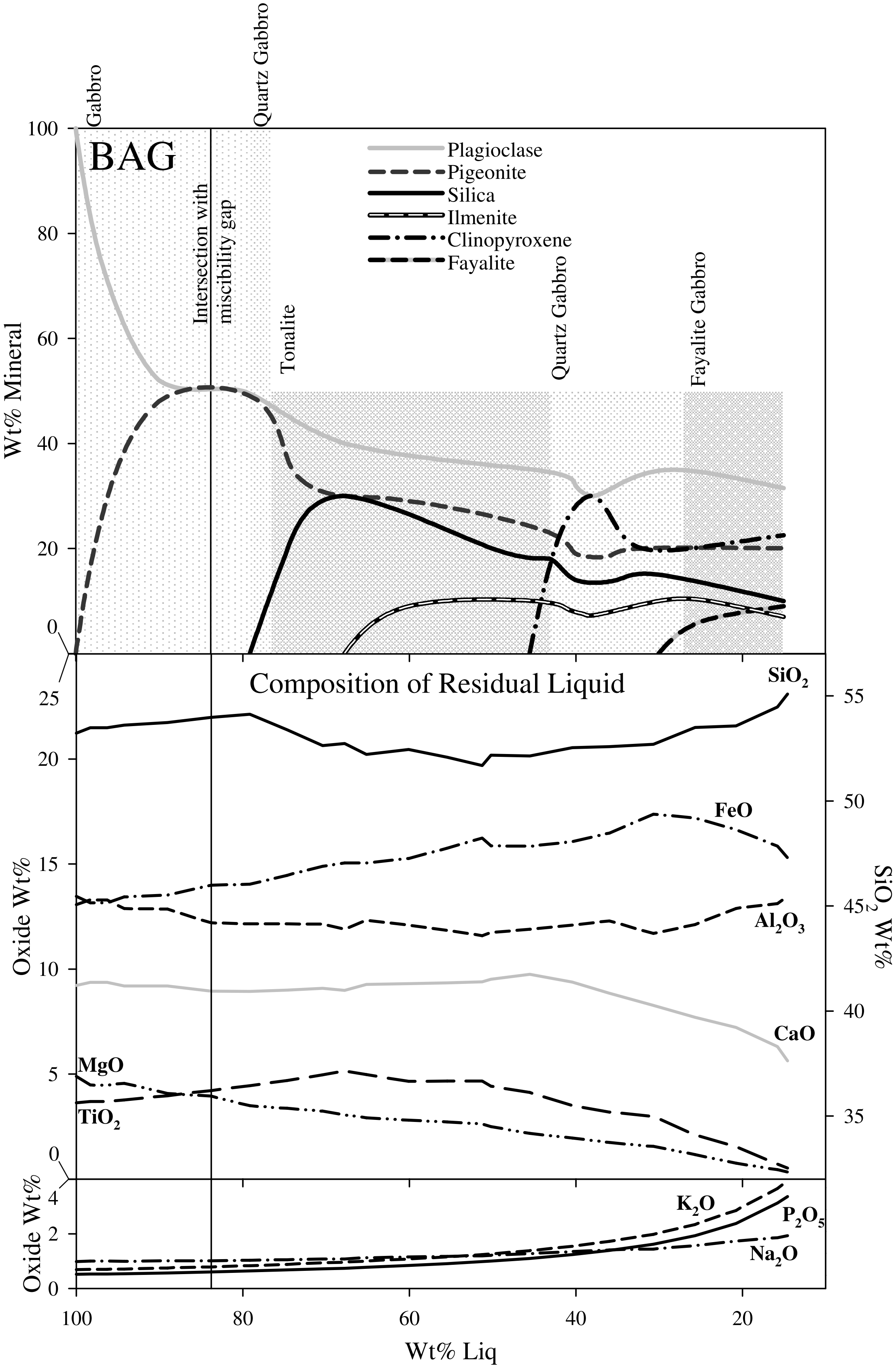
BAG
Gabbro
Quartz Gabbro
Intersection with miscibility gap
Tonalite
Quartz Gabbro
Fayalite Gabbro
Plagioclase
Pigeonite
Silica
Ilmenite
Clinopyroxene
Fayalite
Wt% Mineral
100
80
60
40
20
0
Composition of Residual Liquid
SiO_2
FeO
Al_2O_3
CaO
MgO
TiO_2
Oxide Wt%
25
20
15
10
5
0
SiO_2 Wt%
55
50
45
40
35
K_2O
P_2O_5
Na_2O
Oxide Wt%
4
2
0
100
80
60
40
20
Wt% Liq

Figure 16. Ternary diagram illustrating the compositional paths that the KB and BAG residual melt compositions follow during fractional crystallization. Note that the BAG path barely intersects the field of SLI, while the KB path does not intersect it. The granitic compositions (natural and experimental) of Table 7 are also plotted. All units are in wt%.

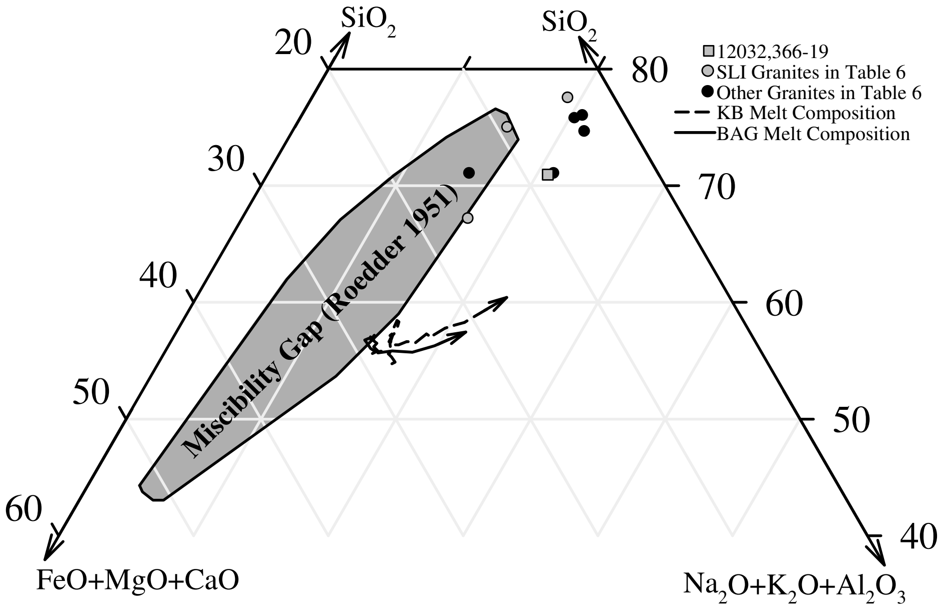

Figure 17. Illustration depicting a gravity separation model that could have produced a mineralogy like that of 12032,366-19 without requiring SLI.

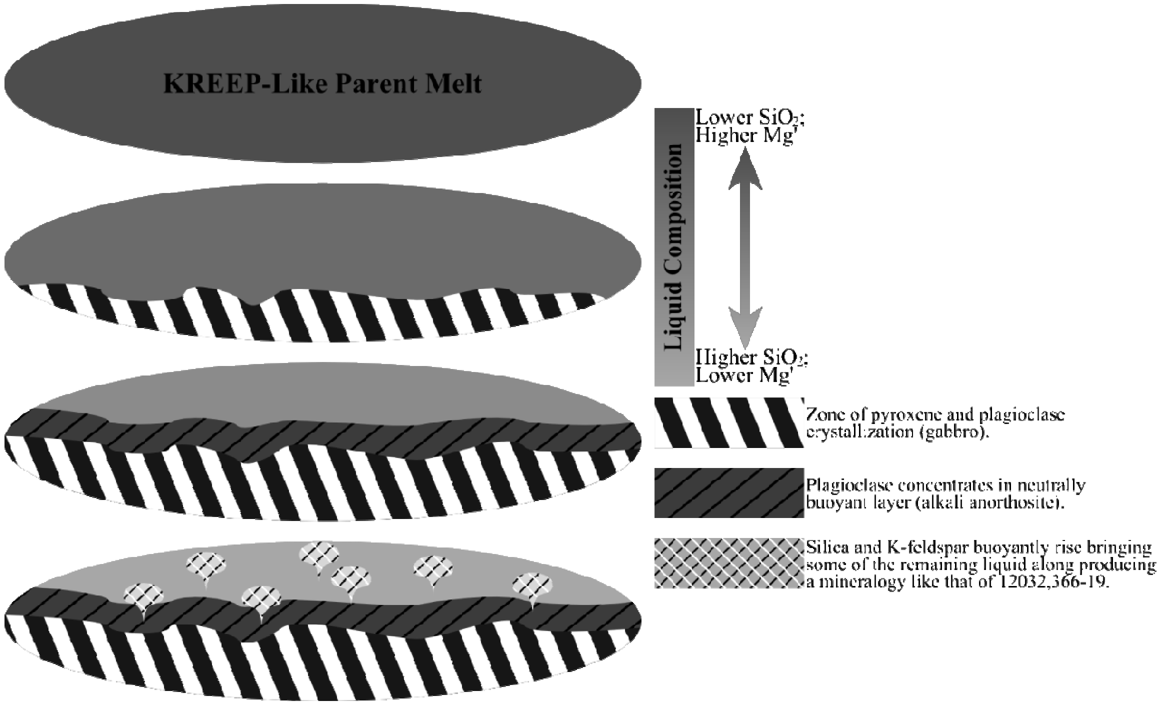

Appendix 1. Bulk compositions of selected lunar granites and felsites.

Sample	12032, 366-19A	12032, 366-19B	12001, 909-14	12003, 254	12013, 10,12a	12013, 10,16b	12013, 10,28	12013, 10A	12023, 147-10	12032, 367-04	12033, 517	12033, 634-30	12033, 634-34
Method	M1	INAA	INAA	INAA	INAA	INAA	INAA	INAA*	INAA	INAA	INAA, RNAA	INAA	INAA
SiO_2	70.1	-	-	-	-	-	-	60.8	-	-	65.0	-	-
TiO_2	1.07	-	-	0.8	0.30	0.75	0.86	1.50	-	-	1.50	-	-
Al_2O_3	13.5	-	-	11.6	10.1	11.1	9.8	12.8	-	-	12.9	-	-
FeO	4.98	4.99	8.45	10.7	14.0	9.60	6.00	10.68	3.11	8.62	7.60	9.00	12.5
MnO	0.07	-	-	0.14	0.15	0.12	0.08	0.15	-	-	0.04	-	-
MgO	0.14	-	-	5.5	8.50	6.30	5.50	-	-	-	2.40	-	-
CaO	3.04	2.9	6.9	5.4	4.6	4.1	3.8	7.1	3.0	9.1	4.9	9.2	6.4
BaO	0.68	0.68	0.22	0.40	0.42	0.46	0.46	-	0.44	0.19	0.51	0.48	0.51
Na_2O	2.47	2.10	1.37	1.3	1.12	1.28	1.17	1.25	1.22	1.27	1.47	1.66	1.04
K_2O	4.58	4.8	2.9	2.4	2.60	3.74	3.03	1.65	5.60	2.20	2.96	3.40	3.90
P_2O_5	0.052	-	-	-	-	-	-	-	-	-	-	-	-
Total	100.7	-	-	-	-	-	-	-	-	-	-	-	-
Mass	Section	21.28	7.01	8.10	5.25	1.21	0.98	Mass weighted	2.67	7.39	99.3	7.50	6.96

Oxides are in wt%; elements are in ppm except for Ir and Au which are in ppb. "-" means "not reported." "n.d." means "not detected." "EPMA" implies a defocused beam analysis. "RNAA" stands for radiochemical neutron activation analysis. "Mass" refers to the mass of the sample analyzed in mg. 12032,366-19 A (Model 1 from EPMA, this study). 12032,366-19 B; 12001,909-14 (INAA data, this study). 12003,254 (Laul 1986). 12013,10,12a; 12013,10,16b; 12013,10,28 (Quick et al. 1977). 12013,10 A (12013,10 weighted mean; Wakita and Schmitt 1970). 12013 light (Hubbard et al. 1970, Schnetzler et al. 1970, Wakita and Schmitt 1970, and Quick et al. 1977). 12023,147-10; 12032,367-04 (INAA data, this study). 12033, 517 (Warren et al. 1987). 12033,634-30; 12032,634-34 (INAA data, this study). 12070,102-5 (Marvin et al. 1971). 14001,28.2, 14001,28.3, and 14001,28.4 (Morris et al. 1990). 14004,94 and 14004,96 (Snyder et al. 1992). 14161,7269 (Jolliff et al. 1991). 14303,204, 14321,1027 (Warren et al. 1983c). 15405,12 (Ryder 1976). 15434,10 (Ryder and Martinez 1991). 73215,43,3 (Blanchard et al. 1977). 73255,27,3 (Blanchard and Budahn 1979).

*SiO_2 was calculated.

Appendix 1 continued.

Sample	12070, 102-5	14001, 28.2	14001, 28.3	14001, 28.4	14004, 94	14004, 96	14161, 7269	14303, 204	14321, 1027	15405, 12	15434, 10	73215, 43,3	73255, 27,3
Methods	EPMA	INAA	INAA	INAA	INAA	INAA	INAA EPMA	INAA	INAA	EPMA	FB	INAA	INAA
SiO_2	70.80	-	-	-	-	-	71.9	-	74.20	68.08	56.9	-	-
TiO_2	0.60	1.80	1.40	1.00	1.35	1.14	0.54	0.75	0.33	0.90	1.13	-	0.26
Al_2O_3	12.70	9.6	8.8	11.3	12.3	13.2	12.6	18.5	12.50	10.15	6.4	-	12.30
FeO	6.30	9.10	12.2	11.0	7.70	6.30	2.26	5.57	2.32	6.99	18.6	2.98	3.10
MnO	0.10	0.11	0.13	0.13	0.11	0.08	0.02	0.06	0.02	-	0.28	-	0.04
MgO	0.40	<1.2	<0.83	<0.99	-	-	0.03	3.30	0.07	1.53	4.7	-	0.20
CaO	1.00	3.9	5.5	5.7	5.1	5.1	0.93	8.8	1.25	4.89	8.3	-	0.50
BaO	-	0.40	0.26	0.35	0.29	0.31	0.11	0.23	0.24	-	0.20	-	0.61
Na_2O	1.10	1.70	1.40	1.90	1.56	1.54	0.56	1.25	0.52	0.79	0.56	0.19	0.53
K_2O	7.40	3.40	2.10	2.50	3.10	3.20	10.06	3.60	8.60	3.39	2.17	7.00	7.55
P_2O_5	0.70	-	-	-	-	-	0.13	-	-	-	1.33	-	-
Total	101.1	-	-	-	-	-	99.3	-	100.1	96.7	100.6	-	100.6
Mass	Section	34.2	15.3	15.0	133.3	97.1	36.4	70	149	Section	27	20	2.0

Appendix 1 continued.

	12032, 366-19A	12032, 366-19B	12001, 909-14	12003, 254	12013, 10,12a	12013, 10,16b	12013, 10,28	12013, 10A	12013, 10 B	12013 light	12023, 147-10	12032, 367-04	12033, 507	12033, 634-30	12033, 634-34
Cr	<200	11.3	610	1539	1723	1034	589.4	1410	1471	1010	31	8.62	479.5	66	19
Zr	1500	1500	1470	610	690	1130	720	-	766	1130	970	9.1	1310	2500	3020
Hf	37.8	45.5	38.9	4.7	27	23	25	23.0	26.1	24	31.5	0.19	37	65.1	78.2
La	11.3	79.4	115.6	50	57	64	39	66	55	68	77.0	1.274	82	213.0	181.2
Ce	106	182	289	110	151	170	100	-	111	126	184	2.20	199	539	435
Nd	83.2	82	159	56	74	91	59	-	75	64	80		100	310	212
Sm	-	24.6	46.3	14.1	19	20	13	25.0	18	16	23.8		28	87.8	62.8
Eu	-	3.01	2.60	2.7	2.14	1.85	1.74	2.00	2.04	2.54	2.38	1119	3.10	5.03	3.84
Tb	-	6.56	9.84	4	5.2	4.9	3.7	-	5.0	4.9	6.06	900	6.8	18.29	15.22
Yb	-	51.8	45.90	32	30.0	35.0	25.0	30.0	26.6	33.4	43.7	22.8	36.7	68.10	90.20
Lu	-	7.44	6.17	4.8	4.2	5.2	3.0	4.1	4.2	5.1	6.19	80.5	5.8	9.29	12.48
Sc	-	8.7	16.7	23.2	25.0	21.0	17.0	27	23	21	6.3	203	14.9	26.0	23.6
Co	-	0.8	9.3	12	24.0	12.0	8.6	26	20	20	0.8	107	8.0	7.5	4.7
Ni	-	<25	<50.	<40	-	-	-	-	-	-	<50	32.90	22.0	<70	<160
Rb	-	96	74	-	87	124	101	-	94.9	141	172	2.84	79	63	77
Sr	-	167	145	180	-	-	-	-	-	168	134	6.90	156	227	180
Cs	-	3.67	3.22	-	3.1	4.0	4.3	-	3.4	4	4.98	28.90	3.0	2.10	2.26
Ta	-	10.4	6.9	7.7	-	-	-	-	6.7	6.6	8.8	4.020	-	9.1	9.4
W	-	8.7	4.5	-	-	-	-	-	-	-	3.7	21.0	-	4.0	7.5
Ir	-	<0.0013	<5.	-	-	-	-	-	-	-	<4.	17.2	1.27	<5.	<6.
Au	-	<0.005	<5.	-	-	-	-	-	-	-	<11.	81	0.51	<9.	<6.
Th	126	60.6	39.0	37	48	45	36	22	45.5	41	59.5	53	40	52.9	61.7
U	52.7	20.7	11.2	11.3	14	12	10	8	13.4	12.3	19.5	171	12	16.1	18.9

Appendix 1 continued.

	12070, 102-5	14001, 28.2	14001, 28.3	14001, 28.4	14004, 94	14004, 96	14161, 7269	14303, 204	14321, 1027	15405, 12	15434, 10	73215, 43,3	73255, 27,3
Cr	0.00	94.90	149.8	99.89	91.90	137.9	679.3	549.4	17.00	-	1129	103.0	70.00
Zr	-	-	-	-	-	-	890	1020	660	-	885	-	-
Hf	-	41	120	43	41	51	33	22	13.9	-	19.4	25.6	16
La	-	110	200	130	91	87	95	58	44.3	-	65	42.9	20.3
Ce	-	250	460	270	218	237	-	149	117	-	174	125	50
Nd	-	-	-	-	111	113	-	93	58	-	101	-	34
Sm	-	36	66	40	33	33	36	22	15.9	-	64.5	19	6.74
Eu	-	2.80	3.30	3.00	2.53	2.82	2.69	3.30	1.17	-	1.44	3.11	2.71
Tb	-	8.1	15.0	9.3	8.1	8.4	8.0	4.9	4.3	-	7.6	5.6	1.52
Yb	-	37.0	64.0	43.0	38.0	33.0	55.3	18.0	32.2	-	32.7	27.2	10.3
Lu	-	5.0	7.7	5.9	4.9	4.3	7.9	2.6	5.1	-	4.9	5.3	1.5
Sc	-	15.0	20.0	20.0	15.8	13.6	15.6	10.7	3	-	49	4.8	2.3
Co	-	2.7	3.8	3.9	2.4	2.7	15.1	14.1	0.94	-	52.35	2.1	1.5
Ni	-	-	-	-	-	-	110.0	<60	4.9	-	-	n.d.	-
Rb	-	110	87	89	87	92	107	114	210	-	52.5	-	-
Sr	-	170	170	190	150	110	190	210	55±16	-	118	-	215
Cs	-	2.3	2.0	2.2	2.0	2.9	5.0	2.2	5.7	-	0.47	-	-
Ta	-	-	-	-	-	-	-	-	8.3	-	4.4	5.4	2.4
W	-	-	-	-	-	-	-	-	-	-	-	-	-
Ir	-	<1.6	<5.7	<5.1	<1.4	<1.7	<6	<2.8	47	-	-	-	-
Au	-	-	-	-	10.00	<4	<4	-	35	-	<5	-	-
Th	-	35	42	28	29	30	66	-	65	-	19.7	39.9	9.5
U	-	9.1	13	8.2	8.2	9.9	20	-	23.4	-	5.7	-	-